COMPACT ANTENNAS FOR MIMO COMMUNICATIONS

A Dissertation by

Chandana K.K. Jayasooriya

Master of Science, Wichita State University, 2006

Diplom-Ingenieur, Technical University of Berlin, 2004

Submitted to the Department of Electrical Engineering and Computer Science
and the faculty of the Graduate School of
Wichita State University
in partial fulfillment of
the requirements for the degree of
Doctor of Philosophy

July 2013

COMPACT ANTENNAS FOR MIMO COMMUNICATIONS

The following faculty have examined the final copy of this thesis for form and content, and recommended that it be accepted in partial fulfillment of the requirement for the degree of Doctor of Philosophy with a major in Electrical Engineering.

Hyuck M. Kwon, Committee Chair

Yanwu Ding, Committee Member

Victor Isakov, Committee Member

Vinod Namboodiri, Committee Member

John Watkins, Committee Member

Accepted for the College of Engineering

Vish Prasad, Interim Dean

Accepted for the Graduate School

Abu Masud, Interim Dean

DEDICATION

To my parents and my two children

ACKNOWLEDGEMENTS

I would like to express my gratitude to my advisor, Dr. Hyuck M. Kwon, for his guidance and patience throughout the past few years. This dissertation would not have been possible without the financial support that he provided me.

I am grateful to my committee members, Dr. John Watkins, Dr. Yanwu Ding, Dr. Vinod Namboodiri, and Dr. Victor Isakov for their support. I would also like to thank the Department of Electrical Engineering and Computer Science for providing me with a teaching assistantship during my graduate studies.

Special thanks goes to Dr. Sudharman Jayaweera for giving me the opportunity to pursue graduate studies in the U.S.A.

I also acknowledge colleagues in the Wireless Communications Group and all my friends at WSU who entered my life during last few years. It was a great pleasure to experience their company.

My sincere gratitude goes to my loving parents who showed me the importance of education and my brothers and sisters who guided me and helped me in various ways to achieve my accomplishments. Special thanks to my son and wife who reluctantly let me go to the lab on weekends.

This work was partly sponsored by the Army Research Office under DEPSCoR ARO Grant W911-NF-08-1-0256, and by NASA under EPSCoR CAN Grant NNX08AV84A.

ABSTRACT

The newest cellular communication standard, 4G-LTE (Long Term Evolution) provides an all internet protocol(IP)-based solutions to the high data rate required of mobile communication applications. It offers 100 Mbit/s and 1 Gbit/s for low mobility and high mobility applications, respectively. These high data rates are possible mainly due to the use of multiple antennas at both ends of the communication system. Therefore, antenna design for this new cellular standard is of high interest. Due to the size limitations of a hand-held device (typically, 120 mm×65 mm×5 mm (L×W×H)) designing antennas has become more challenging. Minimal antenna size, mutual coupling between different antennas, and compliance with radiation restrictions are some of the challenges that influence the design of antennas for this new standard.

This work focuses on designing compact antennas to be used in mobile handsets as well as wireless routers such as in the IEEE 802.11n standard. The first attempt was to design a two-port co-located circular patch antenna (CPA) and an annular ring antenna (ARA) that utilizes pattern diversity. The idea behind pattern diversity is to generate two orthogonal radiation patterns associated with each port. To reduce the size of the antenna, ferrite material is used as the substrate material. Even though the use of ferrite material leads to a significant size reduction, the dimensions of those antennas are too large to fit in a cellular mobile handset. Therefore, a spatially separated half-cycle meander structure was investigated. This antenna was designed to fit into a mobile handset using FEKO simulations, and then fabricated and tested. By using the simulated S-parameters and radiation patterns, all of these antennas were investigated for communication theoretic performance parameters such as bit error rate (BER) and capacity.

TABLE OF CONTENTS

Chapter Page

1 INTRODUCTION **1**

2 LITERATURE SURVEY **7**

3 COMMUNICATION THEORETIC PERFORMANCE METRICS **13**

3.1 System Model 13

3.2 Spatial Correlation of Radiation Patterns 14

3.3 Performance Evaluation 15

3.3.1 Bit Error Rate 16

3.3.2 System Capacity 18

4 MICROWAVE THEORETIC PERFORMANCE METRICS **22**

4.1 Scattering Parameters 22

4.2 Antenna Efficiency 25

4.3 Antenna Bandwidth 25

4.4 Mutual Impedance 26

5 FERRITE CIRCULAR PATCH ANTENNA (1-CPA) **28**

5.1 Modes of Circular Patch Antenna 28

5.2 Radiation Characteristics 30

5.3 Simulation Setup and Results 32

5.4 Parameter Comparison of Fe 1-CPA and Dielectric 2-CPA 38

5.5 Performance Evaluation in Clustered MIMO Channels - Fe 1-CPA 38

6 FERRITE ANNULAR RING ANTENNA (1-ARA) **45**

TABLE OF CONTENTS (continued)

Chapter Page

6.1 Radiation Characteristics 45
6.2 Simulation Setup 45
6.3 Performance Evaluation in Clustered MIMO Channels - Fe 1-ARA 48

7 FABRICATED FE 1-CPA AND FE 1-ARA 54
7.1 Antenna Measurement Methodology 56
7.2 Fe 1-CPA 59
7.3 Fe 1-ARA 60

8 PARAMETER OPTIMIZATION OF FE 1-CPA 63
8.1 Optimization of all Parameters Simultaneously using PSO Algorithm 64
8.2 Optimization of a Single Parameter using PSO Algorithm 66

9 HIGH-EFFICIENCY MEANDER ANTENNA (HEMA) 76
9.1 HEMA Antenna Design 76
9.1.1 Ground Plane and Y-Shaped Slit 78
9.1.2 Substrate Material 83
9.1.3 Fabricated Antenna 83
9.2 Measurement Results of Fabricated HEMA 84
9.3 Performance Analysis 88

10 CONCLUSIONS 94

REFERENCES 100

LIST OF TABLES

Table Page

2.1 COMPARISON OF COMPACT MIMO ANTENNAS FOR LTE/LTE-ADVANCED STANDARDS. 12

4.1 COMPARISON OF SWR, REFLECTION COEFFICIENT, AND RETURN LOSS. 25

5.1 PARAMETERS OF DIELECTRIC 2-CPA and FERRITE 1-CPA. 33

7.1 PARAMETERS OF DIELECTRIC 2-CPA, FERRITE 1-CPA, and FERRITE 1-ARA. 62

8.1 RANGE OF PARAMETER VALUES USED IN OPTIMIZATION. 64

8.2 PARAMETERS USED IN SINGLE PARAMETER OPTIMIZATION USING PSO. 75

LIST OF FIGURES

Figure Page

1.1 Single-input single-output (SISO) and multiple-input multiple-output (MIMO) radio channels. 4

3.1 Block diagram of two-branch transmit diversity scheme. 17
3.2 Block diagram of communication system. 19

4.1 Arbitrary N-port microwave network. 23

5.1 Superimposed ideal radiation patterns of circular patch antenna excited with mode $n = 3$. Far-field patterns calculated according to equations (5.2.2) and (5.2.3) for $\theta = \pi/2$. Ports 1 and 2 correspond to $\phi_0 = 0$ and $\phi_0 = \pi/6$, respectively. 31
5.2 Geometry of Fe 1-CPA design (top view.) 32
5.3 Three-dimensional radiation patterns of circular patch antenna excited with mode $n = 3$: Fe 1-CPA using FEKO. Only port at $\phi = 0$ was excited. 34
5.4 Three-dimensional radiation patterns of circular patch antenna excited with mode $n = 3$: Fe 1-CPA using FEKO. Only port at $\phi = \pi/2$ was excited. . . . 34
5.5 Superimposed radiation patterns of Fe 1-CPA excited with mode $n = 3$ when ports are excited consecutively, and radiation patterns are overlaid: Using FEKO. 35
5.6 Simulated S-parameters of Fe 1-CPA: Using FEKO. 37
5.7 Input impedance loci of Fe 1-CPA: Using FEKO. 37
5.8 Correlation coefficients of Fe 1-CPA calculated according to equation (3.2.1) using realistic radiation patterns shown in Figure 5.5. 39
5.9 Correlation coefficients of Fe 1-CPA calculated according to equation (14) and equation (20) in [15] with ideal electric fields. 39

LIST OF FIGURES (continued)

Figure Page

5.10 Ergodic capacity of Fe 1-CPA vs. angle of arrival and signal-to-noise. 41
5.11 Ergodic capacity of Fe 1-CPA vs. angle of arrival with signal-to-noise ratio as parameter. 41
5.12 Bit error rate of Fe 1-CPA vs. angle of arrival. 42
5.13 Bit error rate of Fe 1-CPA vs. angle of arrival with signal-to-noise ratio as a parameter. 43
5.14 Bit error rate comparison of 2×2 MIMO vs. Fe 1-CPA using Alamouti scheme under Rayleigh fading channel. 44

6.1 Geometry of Fe 1-ARA design (top view.) 46
6.2 Three-dimensional gain patterns of Fe 1-ARA in decibels. Only port at $\phi = 0$ was excited. 47
6.3 Three-dimensional gain patterns of Fe 1-ARA in decibels. Only port at $\phi = \pi/2$ was excited. 47
6.4 Two-dimensional overlaid gain patterns of Fe 1-ARA. 47
6.5 Simulated S-parameters of Fe 1-ARA. 48
6.6 Correlation coefficients of Fe 1-ARA calculated according to equation (3.2.1) using radiation patterns shown in Figure 6.4. 49
6.7 Ergodic capacity of Fe 1-ARA vs. angle of arrival and signal-to-noise ratio. . 50
6.8 Ergodic capacity of Fe 1-ARA vs. angle of arrival with signal-to-noise ratio as a parameter. 50
6.9 Bit error rate of Fe 1-ARA vs. angle of arrival and signal-to-noise ratio. . . . 51

Figure Page

6.10 Bit error rate of Fe 1-ARA vs. angle of arrival with signal-to-noise ratio as a parameter. 52
6.11 Bit error rate comparison of 2×2 MIMO vs. Fe 1-ARA using Alamouti scheme under Rayleigh fading channel. 53

7.1 Fabricated Fe 1-CPA: top, bottom, and side views. 54
7.2 Fabricated Fe 1-ARA: top, bottom, and side views. 54
7.3 Measured permittivity and permeability spectra of $Ba_3Co_2Fe_{24}O_{41}$ hexaferrite (10 h shake-milling) + 2 wt% glass sintered at 950° C for 1 h. 55
7.4 Measuring reflection coefficients of antenna 1 and antenna 2. 56
7.5 Measuring transmission coefficients from antenna 1 to antenna 2 and vice versa. 57
7.6 Block diagram of measurement setup of antenna radiation patterns. 58
7.7 Simulated and measured S-parameters of Fe 1-CPA. 59
7.8 Simulated and measured S-parameters of Fe 1-ARA. 60
7.9 Measured and simulated gains of fabricated Fe 1-ARA over azimuth plane (a) at $f = 1.9$ GHz and at (b) $f = 2.7$ GHz. 61

8.1 Particle swarm optimization of parameters f, ρ_f, g, and h of Fe 1-CPA. All the parameters were varied simultaneously. 65
8.2 Gain and antenna efficiency variations in particle swarm optimization. 66
8.3 Particle swarm optimization of parameter h. 67
8.4 Gain and antenna efficiency variations in particle swarm optimization of parameter h. 68
8.5 Particle swarm optimization of parameter ρ_f. 68
8.6 Dependency of ρ_f on maximum gain in PSO. 69
8.7 Dependency of ρ_f on efficiency in PSO. 69
8.8 Dependency of maximum gain on efficiency in PSO of ρ_f. 70

Figure Page

8.9 Particle swarm optimization of parameter f. 71
8.10 Dependency of f on maximum gain in PSO. 71
8.11 Dependency of f on efficiency in PSO. 72
8.12 Dependency of maximum gain on efficiency in PSO of f. 72
8.13 Particle swarm optimization of parameter g. 73
8.14 Dependency of g on maximum gain in PSO. 73
8.15 Dependency of g on efficiency in PSO. 74
8.16 Dependency of maximum gain on efficiency in PSO of g. 74
8.17 S-parameters of Fe 1-CPA using iteratively optimized parameters. 75

9.1 Geometry and dimensions of antenna model. 77
9.2 Simulated S-parameters of HEMA for variable ground plane lengths, L_1. . . 78
9.3 Simulated S-parameters of HEMA for variable slit widths W_1. Ground plane length $L_1 = 70$ mm. 80
9.4 Simulated S-parameters of HEMA for variable W_2 values. Ground plane length $L_1 = 70$ mm and width $W_1 = 4$ mm. 82
9.5 Top and bottom views of fabricated HEMA. 84
9.6 Simulated and measured S-parameters of HEMA. 85
9.7 Simulated radiation patterns of HEMA. 86
9.8 Simulated and measured radiation patterns of HEMA. Both patterns are shown for $\phi = 90^\circ$ and $\theta = -180^\circ \cdots +180^\circ$ (a) total gain and (b) normalized total measured power. 87
9.9 Simulated gain of HEMA vs. azimuth angle with elevation angle, θ, as a parameter. 88
9.10 Simulated correlation coefficients of HEMA vs. mean angle of arrival ϕ_c. . . 89
9.11 Average BER comparison of HEMA, and theoretical 2×2 MIMO vs. SNR using Alamouti scheme under Rayleigh fading channel. 90

Figure Page

9.12 Average ergodic capacity comparison of HEMA, and theoretical 2×2 MIMO vs. SNR. 91
9.13 Envelope correlation of HEMA calculated according to Eq. 11 in [44]. 92

CHAPTER 1

INTRODUCTION

With the introduction of the first commercial cellular mobile telephone system in the late 1970's, a whole new era in wireless telecommunication began. Even though mobile phones were available as early as 1946, they were extremely heavy or limited to equipment that was installed in automobiles. A milestone in mobile communication history occurred on June 17, 1946, when the first mobile telephone call was made from a car in St. Louis, Missouri [1]. In two years, AT&T offered wireless telephone system in almost 100 cities and highway corridors serving 5,000 customers, such as utilities, truck fleet operators, and reporters. This system was incapable of handling large call volumes, expensive (US $15 per month service cost plus 30 to 40 cents per local call), and far from "mobile."

The current cellular concept for mobile communications was first proposed in 1947 by Bell Laboratories engineers Douglas H. Ring and W. Rae Young [2]. Shortly before that, their colleagues experimented with the first transistor in 1948. Use of multiple low-power base stations to serve "small" areas that form a hexagonal grid ("cells"), frequency reuse, and automatic call handoff from one cell to another comprised this proposal. It was not until the 1960s that those concepts became reality, due to the advancement of computers and electronics. The first public call on a mobile phone was made on April 3, 1973, by a Motorola engineer named Martin Cooper [3]. These early phones cost US $3,000 and weighed about a kilogram.

The first generation (1G) (1980s–1990s) of cellular systems were analog networks that

were introduced in the early 1980s. In 1978, in Chicago and Newark, New Jersey American Telephone and Telegraph (AT&T) conducted Federal Communication Commission (FCC)-authorized field trials of the first analog cellular system in North America, known as the Advanced Mobile Phone System (AMPS). Four years later, the AMPS system was commercially available. In Japan, the cellular system was introduced in 1979 by the Nippon Telegraph and Telephone (NTT). In Nordic countries–Sweden, Norway, Denmark, and Finland–the commercial Nordic Mobile Telephone (NMT) services was launched between 1981 and 1982. This was also an analog cellular system [4].

The Global System of Mobile Communications (GSM), a standard developed by the European Telecommunications Standards Institute (ETSI), and code division multiple access (CDMA), a system developed in U.S., were the key standards that emerged during the second generation (2G) of cellular systems. The first GSM network was launched in Finland in 1991. Unlike in first-generation systems, these were digital systems. With this new technology, data services such as Short Message Service (SMS), commercial payments, and full Internet service evolved.

In 2001, NTT DoCoMo launched the third-generation (3G) communication system in Japan based on wideband code division multiple access (WCDMA) technology.

Current wireless connectivity standards like 802.11n as well as cellular communication standards, LTE (long-term evolution) and LTE-Advanced standards, employ multiple-input multiple-output (MIMO) technology to achieve higher data rates. Maximum downlink (DL) data rates of 172.8 Mbps and 1 Gbps are supported for a 4×4 single-user MIMO system in LTE and LTE-Advanced standards, respectively. To achieve these high data rates, a signal bandwidth as wide as 200 MHz is required for both uplink (UL) and downlink transmission

streams. Therefore, MIMO-capable antennas with wider bandwidth are in high demand.

MIMO is a technology for wireless communication systems in which multiple antennas are used at both the transmitter and the receiver to transfer more data at the same time. MIMO technology takes advantage of the electromagnetic (EM) wave phenomenon called scattering. When an EM wave is met with obstructions, such as hills, buildings, walls, ceilings, and other objects, the wavefronts are scattered. These scattered waves take multiple paths to reach the destination via different angles and at slightly different delays. The effect caused by different arrival angles and delays at the destination is referred to as multipath effect, a condition that must be accommodated by ground-to-ground wireless communication systems. In a wireless communication system in which only a single antenna is used at both the source and the destination, i.e., single-input single-output (SISO), this multipath propagation of electromagnetic waves can cause problems such as fading and intersymbol interference, resulting in the reduction of data rate and increase in bit errors. In contrast, a MIMO system can mitigate multipath effects, and they can be exploited to increase data rates and simultaneously improve the robustness of the radio link. Figure 1.1 depicts SISO and MIMO radio channel and antenna configurations.

As it suggests, the capacity of a MIMO system can be significantly increased by adding more antenna elements. Decreasing the distance between antennas in order to place more antennas in a designated area results in two negative effects. One is the increasing correlation among transmitted signals, and the second is the increasing mutual coupling among antennas [5]. Mutual coupling is a function of antenna spacing, number of antennas, and direction of each ray relative to the array plane. Hence, it becomes difficult to match the antenna impedance, which is important for efficient energy transfer [5].

(a) SISO.

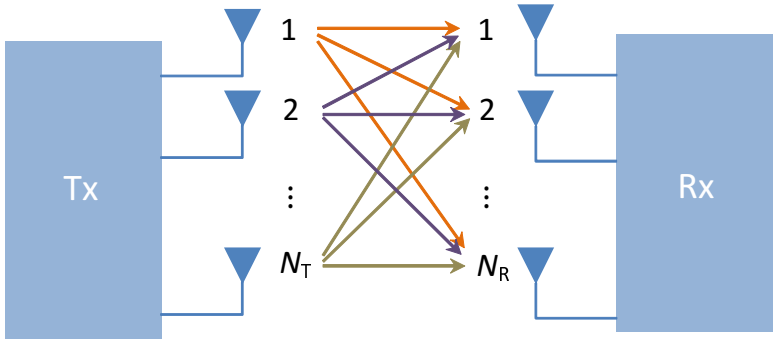

(b) MIMO.

Figure 1.1: Single-input single-output (SISO) and multiple-input multiple-output (MIMO) radio channels.

Making the antenna spacing lower than $\lambda/2$ would cause performance degradation due to the aforementioned effects, where $\lambda = c/f_c$ denotes the wavelength in meters for carrier frequency f_c (Hz) and the speed of light c (m/sec). Jakes showed that the correlation becomes strong even for antenna spacing larger than λ for narrow angular spreads of the significant rays [6]. For example, when $f_c = 2.45$ GHz, the minimum required adjacent antenna spacing of $\lambda/2$ would be 6 cm, which can be restrictive in many space-limited applications, such as handsets, as the number of antenna increases.

The objective of this work is to miniaturize an antenna without sacrificing much performance, especially miniaturization of the more recent two-colocated stacked circular patch antenna (2-CPA) from the work of Forenza and Heath [7]. This work presents three prototypes of fabricated miniaturized antennas: (a) a miniaturized ferrite single circular patch antenna (Fe 1-CPA) [8, 9], (b) a miniaturized ferrite single annular ring patch antenna (Fe 1-ARA) [10, 11], and (c) a highly efficient miniaturized half-cycle meander antenna

(HEMA) [12, 13]. The performances of Fe 1-CPA and Fe 1-ARA are compared to that of the 2-CPA, which generates higher-order orthogonal mode patterns for MIMO communication system applications. The three miniaturized antennas, Fe 1-CPA, Fe 1-ARA, and HEMA use ferrite substrate materials for miniaturization purposes, whereas the 2-CPA uses dielectric substrate materials. Both Fe 1-CPA and Fe 1-ARA were initially designed with the FEKO simulator. Then, both antennas were fabricated using the available ferrite materials in the lab. The parameters of the fabricated antennas were slightly different from those of the initial FEKO designs and therefore adjusted to have bandwidths similar to the simulated antennas in the work of Forenza and Heath [7]. This is because the available ferrite materials in the lab showed higher tangent-loss parameters than the parameters obtained through the FEKO simulations in this work.

It is necessary that an antenna be designed to operate at a desired center frequency. A circular patch antenna (CPA) is a resonant structure that supports different modes that are excited at different frequencies [14]. The resonance frequency of a particular mode of a CPA is proportional to the ratio of the derivative of the Bessel function and the radius of the CPA. It is also inversely proportional to the square root of the product of the permeability (μ) and permittivity (ϵ) of the substrate material. The value of the derivative of the Bessel function increases with the mode number. Therefore, for a given resonance frequency, when the resonance mode of the antenna is increased, which is desired for pattern diversity according to the work of Forenza and Heath [15], the radius of the antenna must be increased. Even though the use of substrate material with high permeability and permittivity can reduce the radius of a CPA, the resulting dimensions of a CPA is prohibitive for use in applications where available space is very limited.

Therefore, a third antenna, HEMA, was designed and investigated. It consists of two spatially separated half-cycle meander structures, which are placed on a system board the size of a current cellular phone. Using a FEKO simulator, the antenna was initially designed and then later fabricated and tested. Each antenna element emits a different radiation pattern, resulting in pattern diversity. Use of low-loss ferrite material in the HEMA fabrication resulted in a highly efficient antenna. S-parameters and radiation patterns of the simulated and the fabricated antenna were compared, and then the performance of the 2×2 MIMO antenna was evaluated in terms of bit error rate and capacity.

This dissertation is organized as follows. Chapter 2 presents a survey of literature related to this dissertation. Chapters 3 and 4 present communication theoretic and microwave theoretic performance metrics that were used to characterize and evaluate the presented antennas, respectively. Design, simulation, and performance evaluation of the Fe 1-CPA and Fe 1-ARA are presented in chapters 5 and 6, respectively. Chapter 7 presents the fabricated Fe 1-CPA and Fe 1-ARA. Parameter optimization of Fe 1-CPA is presented in chapter 8. Design, simulation results, and performance analysis of a high-efficiency half-cycle meander antenna is presented in chapter 9. The fabricated HEMA antenna is also discussed. Chapter 10 concludes the dissertation.

CHAPTER 2

LITERATURE SURVEY

A collection of recent miniaturized antennas utilizing different technologies were presented by the NASA Glenn Research Center (GRC) [16]: a folded Hilbert curve fractal antenna (fHCFA) [17], a compact microstrip monopole antenna (CMMA) [18], a self-powered antenna, a reconfigurable spiral microstrip patch antenna [19], a miniaturized antenna for random sensor arrays [20], and an antenna using metamaterials. These antennas are specifically designed for future lunar and Martian mission applications. The size of a monopole antenna can be reduced by folding it upon itself in the form of a meander line. Further size reduction can be achieved by using fractal antennas [21,22]. A fractal antenna was designed by folding a third-order Hilbert curve upon itself in four layers [17]. These layers are separated by air gaps. The overall dimensions of thr fHCFA presented are 5 mm $\times$ 5 mm $\times$ 4.5 mm (L$\times$W$\times$H), and it achieves a size reduction of factor approximately 15, compared to a monopole at 2.3 GHz resonance frequency. Even though this antenna has a 500 MHz (3%) 10 dB-bandwidth at 16.8 GHz, it is merely 10 MHz (0.5%) at 2.3 GHz. Even though fractal antennas can be designed to operate wideband or multiband simultaneously, thus reducing antenna size significantly, their broadside or endfire radiation characteristics restrict their use in cellular communication systems.

The compact microstrip monopole antenna (CMMA) consists of a tri-lobed patch (TLP) of size 12 mm $\times$ 12 mm with a vertical enclosure wall (VEW) of height 11 mm, and a grounding wall (GW). This antenna was designed to perate at 2.3 GHz and achieves a size

reduction factor of 11.6 compared to a monopole. The size reduction of this antenna is achieved by increasing the perimeter of the ungrounded patch by introducing three lobes. The bandwidth of the antenna is 130 MHz. High directivity of this antenna is undesirable for cellular communication systems.

The antenna presented in [19] consists of a single-turn square microstrip spiral of size 19.25 mm $\times$ 17 mm and two single radio frequency microelectromechanical systems (RF MEMS) switches. RF MEMS switches are used to reconfigure the radiation pattern behavior (broadside or endfire radiation, depending on the states of the switches.) The antenna is designed to operate at 6.85 GHz and fabricated on 3.175 mm-thick Duroid 5880 substrate. The achieved bandwidth at 2:1 voltage standing wave ratio (VSWR) is 80 MHz (1.1%), which is significantly low. If this antenna is to be designed for 2.45 GHz band the dimensions will be significantly large for space-limited applications.

The miniaturized antenna presented by Soldner et al. [20] consists of two stacked trapezoidal antennae of size 28 mm $\times$ 24 mm. It achieves a 2:1 VSWR bandwidth of 100 MHz (3.8%) around 2.66 GHz while occupying only 4 cm^3. Use of inductive loads placed across the antenna aperture results in shifting the operating bandwidth of the antenna to a lower frequency without increasing the physical size. Its stacked sectors create closely separated multiple resonances resulting in an increase of antenna bandwidth. This antenna shows an omnidirectional radiation pattern, which is favorable for cellular systems. But its efficiency is merely 65%, which is significantly low, and the height of the antenna (6 mm) could be too high for space-limited applications, such as cellular phone handsets.

Use of metamaterials in antenna design offers significant size reduction. Because their fabrication is unknown, these materials are not considered in this work.

Although some of above-discussed antennae employ multiple-antenna array elements, they are not designed for exploiting multiple-input (transmit) and multiple-output (receive) space-diversity gain but rather are designed for exploiting beam-forming gain. They do not fit into the MIMO/orthogonal frequency division multiple access (OFDMA) applications. A MIMO system can significantly increase the capacity of a broadband channel by using multiple antennas at the transmitter (TX) and/or receiver (RX) without increasing total power and bandwidth [23]. MIMO system capacity can be much higher than that of the SISO system [23] and increases linearly with the number of antennas in the presence of a rich scattering environment, which ensures that the signal from each transmit antenna of the multiple antennas becomes uncorrelated. According to Shannon's classical formula in the high signal-to-noise ratio (SNR) realm, the capacity of a SISO system increases one more bit/(s·Hz) for every 3 dB increase in SNR. Hence, in a MIMO system with n antennas at both transmitter and receiver, for the case of independent Rayleigh faded paths among TX and RX antenna elements, capacity increases with n more bits/(s·Hz) for every 3 dB SNR improvement [5].

Different diversity techniques, e.g., spatial, polarization, and pattern, have been proposed to reduce the correlation among subchannels in a MIMO communication system. Up to six degrees of freedom are available in polarization diversity in a rich scattering environment, which can increase the channel capacity significantly [24]. However, the effective degrees of freedom are reduced to three in a real environment, because the channels are not completely uncorrelated in a polarization diversity scheme [24]. In the work of Andrews et al. [24], to demonstrate polarization diversity, three electric dipoles and three magnetic dipoles were placed orthogonally along the x, y, and z axes.

Microstrip antennas have been studied in numerous research studies, almost all of which deal with the fundamental mode and a single-feed probe (or port). A two-port higher-order circular microstrip antenna has been previously studied [25–27], whereby a generation of orthogonal radiation patterns is introduced by using two angularly separated feed probes. Here the mathematical condition for orthogonality of radiation patterns and the correlation between different radiation patterns were introduced. In the work of Dammerle and Wiesbeck [28], higher-order modes were excited in a biconical antenna using several feed probes. Dong et al. [29] showed analytically that a transceiver array with appropriate dissimilarity in radiation patterns in conjunction with spatial diversity can reduce correlation among subchannels, thus resulting in higher system capacity. More recently, a circular patch antenna-based pattern diversity was introduced and analyzed [15]. Two colocated stacked CPAs were used to generate two orthogonal far-field radiation patterns, which in turn were used to show that a diversity gain can be achieved by exploiting pattern diversity instead of space diversity [15]. Feasibility was demonstrated through simulations showing that a MIMO communication system can be realized using the pattern diversity technique, even where strict size limitations apply. Forenza and Heath [7] extended their own work [15] through simulations, where each of two stacked CPAs (2-CPA) had a single-probe feed. These two feed probes were separated over the azimuth plane so that the generated far-field radiation patterns were approximately orthogonal. In addition to the preceding analytical work, the feasibility of generating orthogonal radiation patterns using a single circular patch antenna with two spatially separated feed probes was presented [30]. This demonstrates the feasibility of generating TM_{13} (mode 3) or TM_{14} (mode 4) by varying the radius of the patch by turning on or off the PIN diodes located between an outer ring and an inner disc. Two

orthogonal radiation patterns were generated for each excited mode. This reconfigurable antenna was fabricated on a FR4 substrate and operates at 2.48 GHz. Simulation results agreed with the measured radiation patterns and S-parameters. This work was extended (analytically) [31] to generate TM_{12} (mode 2), TM_{13} (mode 3), or TM_{14} (mode 4), similar to the work of Piazza et al. [30], but using two outer rings and an inner disc. This antenna was designed to operate at 5.2 GHz, and the simulations were performed assuming RT/duroid 5880 substrate of relative permittivity 2.2. The dimensions of the antennas presented in the work of Piazza et al. [30,31] were not provided in the publications but should be on the same order of the lower CPA presented in the work of Forenza and Heath [7], which has a radius approximately 10.5 cm (0.43λ). A compact dual mode (TM_{01} and TM_{11}) microstrip patch antenna was also introduced [32, 33]. This antenna operates at 2 GHz and has a radius of 3.4 cm (0.37λ). Bandwidth of the antennas presented in the work of Piazza et al. [30, 31], Rajo-Iglesias et al. [32], and Sanchez-Fernandez and Rajo-Iglesias [33] was not provided. The 10 dB-bandwidth of the antenna presented in the work of Forenza and Heath [7] is approximately 75 MHz. It is evident that the antennas discussed above are not suitable for applications where space is limited, due to their physical dimensions.

Many authors [34–43] have proposed MIMO-capable antennas for LTE/LTE-Advanced cellular communication system handsets. Table 2.1 lists a summary of key parameters of 2×2 MIMO antennas designed to operate in the "Band 41" which spans from 2,496 to 2,690 MHz. Some antennas presented in the literature [39–42] are designed to operate in the "Band 17" frequency, which occupies 704 to 716 MHz (UL) and 734 to 746 MHz (DL), and hence are not listed in Table 2.1. Even though the dimensions of the printed circuit board (PCB) of the antenna presented in this paper are similar to those listed in Table 2.1 (except

the antenna in the work of Ssorin et al. [35]), the dimensions of a single antenna element are much smaller. The envelope correlation coefficient, as shown in the work of Blanch et al. [44], was calculated and presented in most of the cases. As indicated in Table 2.1, none of the listed references has considered the evaluation of bit error rate (BER) or capacity of the communication system. Furthermore, the bandwidth is evaluated at a voltage standing wave ratio (VSWR) $< 3:1$, which is -6 dB.

Table 2.1: COMPARISON OF COMPACT MIMO ANTENNAS FOR LTE/LTE-ADVANCED STANDARDS.

Antenna	Frequency Band	Bandwidth (MHz)	Eff. (%)	PCB Size (mm^2)	Elem. Size (mm^2)	Corr. Coeff.
[34]	multiband incl. LTE 2500	410 (VSWR<3:1)	-	125×100	33×11	<0.001
[35]	LTE 2500	280 (VSWR<2.5:1)	-	10×20		<0.25
[36]	LTE 700 & LTE 2500	200 (VSWR<3:1)	97.2	120×50	36×15	
[37]	LTE 2500	790 (VSWR<3:1)	75	90×50	19×10	<0.008
[38]	multiband incl. LTE 2500	250 (VSWR<3:1)	-	100×50	7×50	0.01
Proposed antenna	LTE 2500	262 (VSWR<2:1)	81	90×60	6×8	<0.001

CHAPTER 3

COMMUNICATION THEORETIC PERFORMANCE METRICS

3.1 System Model

The received signal of a MIMO system with N_T transmit antennas and N_R receive antennas can be written as [23]

$$\mathbf{y} = \sqrt{\frac{P}{N_T}}\mathbf{H}\mathbf{x} + \mathbf{n} \tag{3.1.1}$$

where P/N_T denotes the transmit power at each receiver antenna element, $\mathbf{y}$ is the $(N_R \times 1)$ complex received signal vector, $\mathbf{x}$ is the $(N_T \times 1)$ complex normalized transmit signal vector, $\mathbf{H}$ is the complex $(N_R \times N_T)$ MIMO channel matrix, and $\mathbf{n}$ is the $(N_R \times 1)$ complex zero-mean additive white Gaussian noise vector with covariance matrix $\mathbb{E}\{\mathbf{n}\mathbf{n}^*\} = \mathbf{I}_{N_R}$.

The MIMO channel matrix $\mathbf{H}$ for a correlated channel can be separated into a constant matrix $\mathbf{H}_{los}$, which represents the line of sight (LOS), and a variable matrix $\mathbf{H}_{nlos}$, as follows [45]:

$$\mathbf{H} = \sqrt{\frac{K}{K+1}}\mathbf{H}_{los} + \sqrt{\frac{1}{K+1}}\mathbf{H}_{nlos} \tag{3.1.2}$$

where K is the Ricean K-factor, the elements of $\mathbf{H}_{nlos}$ are correlated zero-mean unit variance complex Gaussian variables, the elements of the fixed line-of-sight matrix $\mathbf{H}_{los}$ are written as $exp(j\phi_{i,j})$, and i and j are the TX and RX antenna index, respectively. The notation $exp(j\phi_{i,j})$ is the phase difference between the i^{th} transmit and j^{th} receive antenna [46]. The non-line-of-sight channel matrix is defined as [45]

$$\mathbf{H}_{nlos} = \mathbf{R}_R^{1/2}\mathbf{H}_{iid}\mathbf{R}_T^{1/2} \tag{3.1.3}$$

where, $\mathbf{R}_R$ and $\mathbf{R}_T$ denote the RX and TX spatial correlation matrices, respectively, and

$\mathbf{H}_{iid} \in C^{N_R \times N_T}$ is a matrix of independent and identically distributed (i.i.d.) complex Gaussian fading coefficients. In this work, the line-of-sight component is not considered in the simulations, because most channels are under a multipath rich environment.

3.2 Spatial Correlation of Radiation Patterns

When a MIMO system is being considered, where each antenna elements radiates with a different radiation pattern, the correlation between the radiation pattern of a transmit antenna and that of a receive antenna is discussed here.

A closed-form formula for the spacial correlation coefficient of a 3-D multiple antenna array with arbitrary array configuration was presented in the work of Lee and Cheng [47]. Since the structure of the antenna presented in this paper is planar and non-uniform angular energy distribution is assumed, the formula presented in this work is not used.

The correlation coefficient of the l-th TX antenna and the m-th RX antenna can be expressed using the angular distribution of the received power, i.e., the power angular spectrum (PAS) $S(\Omega)$ and far-field electric field $\underline{E}$ in the work of Forenza and Heath [7] as

$$r_{l,m} = \frac{\int_{\Omega} S(\Omega)\underline{E}_l(\Omega)\underline{E}_m^*(\Omega)d\Omega}{\int_{\Omega} S(\Omega)|\underline{E}_{iso}(\Omega)|^2 d\Omega} \tag{3.2.1}$$

where $\underline{E}_{iso}(\Omega)$ is the far field of ideal isotropic radiators, and $l, m \in \{1, 2\}$ denotes TX and RX antenna indices. In equation (3.2.1), normalization is done with respect to the antenna gain of the ideal isotropic radiator. Normalization in the conventional definition of correlation coefficients does not take into account non-uniformly distributed $S(\Omega)$ or non-uniform antenna gain. Since the spatial correlation is normalized with respect to the gain of the ideal isotropic radiator, the envelope of equation (3.2.1) is not necessarily lower than one [7]. Assuming that the power angular spectrum over the azimuth angle and the elevation

angle are independent, $S(\Omega)$ can be expressed as a product of power angular spectrums over the azimuth angle $S_\phi(\phi)$ and elevation angle $S_\theta(\theta)$, respectively [48]. Furthermore, assuming that the elevation angle spread is smaller than the azimuth angle spread and that received signals are concentrated over the azimuth plane, $S_\theta(\theta)$ can be expressed in the form of the delta function, $\delta(\theta - \pi/2)$ [15]. It has been shown that a Laplacian distribution offers the best fit for the power angular spectrum, for both urban and rural areas [45], which can be expressed as

$$S_\phi(\phi) = c \cdot e^{-\frac{\sqrt{2}}{\sigma_\phi}|\phi - \phi_c|}, \quad \phi, \phi_c \in [-\pi, \pi) \tag{3.2.2}$$

where ϕ is the azimuth angle, ϕ_c is the mean angle of arrival (AoA) of the cluster, and σ_ϕ denotes the standard deviation of the power azimuth spectrum that controls the angular spread. The constant c is determined as $(\sqrt{2}\sigma_\phi(1 - e^{-\sqrt{2}\pi/\sigma_\phi}))^{-1}$ by using the integration property of a probability density function, i.e., $\int_{-\infty}^{\infty} S_\phi(\phi)d\phi = 1$. Correlation coefficients are computed according to equation (3.2.1) by using the far-field electric field components obtained by FEKO simulations for performance evaluation of the system.

3.3 Performance Evaluation

Generally, performance of a communication system is evaluated by capacity or BER. Capacity provides information on how many bits can be transmitted per unit time and per unit bandwidth with zero bit errors, and BER provides information on how many bits will be erroneous on average at a SNR. The channel matrix in equation (3.1.2) is required to calculate both performances. In this paper, the line-of-sight component is not considered. This assumption is valid for a typical multipath rich environment. Hence, only the ideal NLOS channel matrix in equation (3.1.3) or its extended channel matrix in equation (4.4.1)

are used for performance evaluation.

3.3.1 Bit Error Rate

For BER evaluation, Alamouti's transmit diversity scheme presented in [49] was used in [7] and also in this paper for comparison. This simple diversity scheme improves the signal quality at the receiver and achieves a diversity order of $2M$, where M is the number of receive antennas, and two antennas are used at the transmitter end. This scheme assumes perfect channel information at the receiver end for signal detection and no channel information at the transmitter end. Sensitivity to fading is decreased, which allows for usage of higher-order modulation techniques to increase the data rate. For simplicity, in this work, the binary phase shift keying (BPSK) modulation is used, and the BER is calculated and compared with that of a two TX- and two RX-antenna system. A block diagram of this transmit diversity scheme used in this work for BER performance evaluation is shown in Figure 3.1.

In the following discussion, two transmit antennas and two receive antennas are considered. The encoding of the signals and the transmission sequence is as follows: During the first symbol period, signals s_0 and s_1 are transmitted from antenna zero and one, respectively. Signals $-s_1^*$ and s_0^* are transmitted during the next symbol period from antenna zero and one, respectively. The notation $*$ denotes complex conjugate operation.

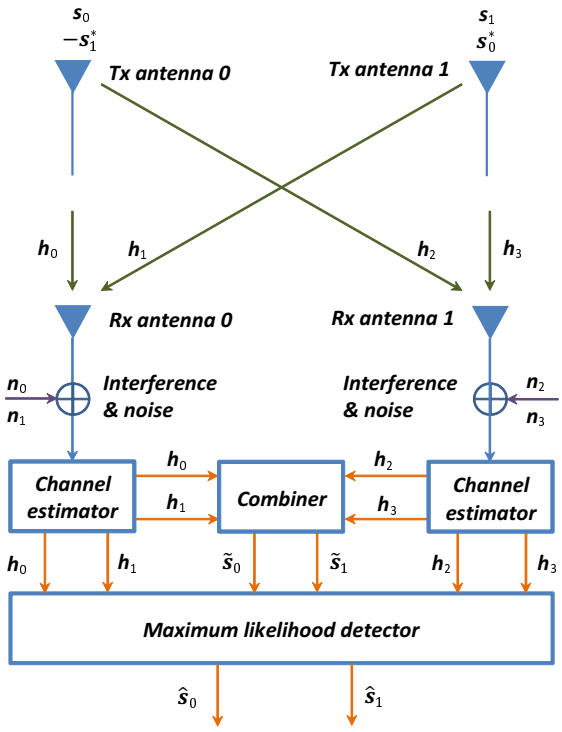

Figure 3.1: Block diagram of two-branch transmit diversity scheme.

The received signals at receive antenna zero and one during two symbol periods can be expressed as

$$\begin{aligned} \boldsymbol{r}_0 &= \boldsymbol{h}_0 \boldsymbol{s}_0 + \boldsymbol{h}_1 \boldsymbol{s}_1 + \boldsymbol{n}_0 \\ \boldsymbol{r}_1 &= -\boldsymbol{h}_0 \boldsymbol{s}_1^* + \boldsymbol{h}_1 \boldsymbol{s}_0^* + \boldsymbol{n}_1 \\ \boldsymbol{r}_2 &= \boldsymbol{h}_2 \boldsymbol{s}_0 + \boldsymbol{h}_3 \boldsymbol{s}_1 + \boldsymbol{n}_2 \\ \boldsymbol{r}_3 &= -\boldsymbol{h}_2 \boldsymbol{s}_1^* + \boldsymbol{h}_3 \boldsymbol{s}_0^* + \boldsymbol{n}_3 \end{aligned} \tag{3.3.1}$$

where r_0, r_1 are the received signals at antenna zero, and r_2, r_3 are the received signals at antenna one. Complex random variables, n_0, n_1, n_2, and n_3 represent thermal noise and interference at the receiver. Using estimated channel coefficients h_0, h_1, h_2, and h_3, the

received signals are combined as follows:

$$\begin{aligned} \tilde{\boldsymbol{s}}_0 &= \boldsymbol{h}_0^* \boldsymbol{r}_0 + \boldsymbol{h}_1 \boldsymbol{r}_1^* + \boldsymbol{h}_2^* \boldsymbol{r}_2 + \boldsymbol{h}_3 \boldsymbol{r}_3^* \\ \tilde{\boldsymbol{s}}_1 &= \boldsymbol{h}_1^* \boldsymbol{r}_0 - \boldsymbol{h}_0 \boldsymbol{r}_1^* + \boldsymbol{h}_3^* \boldsymbol{r}_2 - \boldsymbol{h}_2 \boldsymbol{r}_3^*. \end{aligned} \tag{3.3.2}$$

The maximum likelihood detector uses these combined signals given in equation (3.3.2) and decides on $\tilde{s}_0$ or $\tilde{s}_1$ according to the following criteria:

For signal $\mathbf{s}_0$,

- choose $\mathbf{s}_i$ *iff* $d^2(\tilde{\mathbf{s}}_0, \mathbf{s}_i) \leq d^2(\tilde{\mathbf{s}}_0, \mathbf{s}_k) \quad i \neq \forall k$

For signal $\mathbf{s}_1$,

- choose $\mathbf{s}_i$ *iff* $d^2(\tilde{\mathbf{s}}_1, \mathbf{s}_i) \leq d^2(\tilde{\mathbf{s}}_1, \mathbf{s}_k) \quad i \neq \forall k$

3.3.2 System Capacity

The ergodic channel capacity of a MIMO system with N_T transmit antennas and N_R receive antennas without channel information available at the transmitter end is [5]

$$C = \mathbb{E}\left[\log_2 \det\left[\mathbf{I}_{N_R} + \frac{P}{N_T}\mathbf{H}\mathbf{H}^*\right]\right] \quad \left[\frac{bits}{s \cdot Hz}\right] \tag{3.3.3}$$

where $\mathbb{E}[X]$ is the expectation of a random variable X.

In the derivation of equation (3.3.3), the N_T components of the transmitted signal are assumed to be statistically independent, of equal power, and normally distributed. This capacity is computed using random channel matrix realizations, $\mathbf{H}$, for comparison with those of the proposed antenna. This choice is made because of the simple transmission scheme also used in this paper for evaluating BER performance, which does not require channel matrix information at the transmitter end.

A block diagram of a communication system in the context of "*information*" *channel capacity* is shown in Figure 3.2.

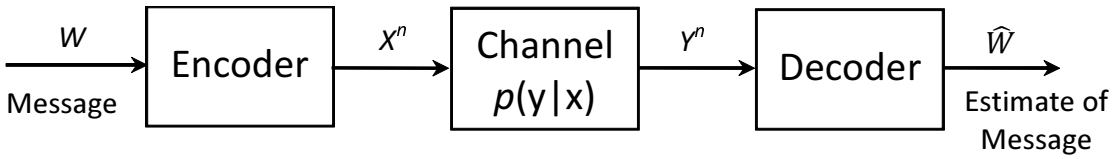

Figure 3.2: Block diagram of communication system.

Input message W is encoded into one of the symbols in the input alphabet $\mathcal{X}$ and transmitted over the channel. The probability of observing the output symbol y given that the symbol x was sent is given by the probability transition matrix $p(y|x)$. The output symbol y is decoded, and an estimate of message W is obtained.

The "*information*" *channel capacity* of a discrete memoryless channel is [50]

$$C = \max_{p(x)} I(X;Y) \tag{3.3.4}$$

where the maximum is taken over all possible input distributions $p(x)$, $\mathbf{x}$, $I(X;Y)$ denotes the mutual information between the the input $\mathbf{x}$ and the output $\mathbf{y}$ of the system, and X and Y are vectors of random variables that represent input and output signals of the system. The mutual information is a measure of the dependence between two random variables. It gives the reduction of the entropy ("uncertainty") of a random variable due to some additional information available about it. The channel is said to be *memoryless* if the probability distribution of the output depends only on the input at that time and is conditionally independent of previous channel inputs or outputs. For continuous random variables X and

Y, the mutual information $I(X;Y)$ can be written as

$$I(X;Y) = h(Y) - h(Y|X) \tag{3.3.5}$$

where $h(Y)$ is the differential entropy of a set of n random variables, which is defined as $-\int f(x^n)\log f(x^n)dx^n$. The notation $f(x^n)$ denotes the joint density function. Substituting equation (3.1.1) in equation (3.3.5) yields

$$\begin{aligned} I(X;Y) &= h(Y) - h\left(\sqrt{\frac{P}{N_T}}\mathbf{H}X + N|X\right) \\ &= h(Y) - h(N|X) \\ &= h(Y) - h(N) \end{aligned} \tag{3.3.6}$$

Differential entropy of a multivariate normal distribution with zero mean and covariance matrix $\mathbf{K_N}$ can be written as [50]

$$h(N_1, N_2, ..., N_{N_R}) = h(\mathcal{N}(0, \mathbf{K}_N)) = \frac{1}{2}\log(2\pi e)^{N_R}|\mathbf{K_N}| \tag{3.3.7}$$

where $|\mathbf{K}_N| = |\mathbf{I}_{N_R}| = 1$ is the determinant of the covariance matrix of the noise random vector N. It can be shown that the multivariate normal distribution maximizes the entropy over all distributions with the same covariance [50]. Therefore, the entropy of the output signal of the system, $h(Y) \leq \frac{1}{2}\log_2(2\pi e)^{N_R}|\mathbf{K}_Y|$, with equality *iff* $Y \sim \mathcal{N}(0, \mathbf{K})$. Therefore,

$$\begin{aligned} I(X;Y) &\leq \log_2(2\pi e)^{N_R}|\mathbf{K}_Y| - \log_2(2\pi e)^{N_R}|\mathbf{K_N}| \\ &= \log_2(2\pi e)^{N_R} + \log_2(|\mathbf{K}_Y|) - \log_2(2\pi e)^{N_R} - \log_2(1) \\ &= \log_2(|\mathbf{K}_Y|) \end{aligned} \tag{3.3.8}$$

The covariance matrix $\mathbf{K}_Y$ can be calculated as follows:

$$\begin{aligned}
\mathbf{K}_Y &= \mathbb{E}\left[YY^*\right] \\
&= \mathbb{E}\left[\left(\sqrt{\frac{P}{N_T}}\mathbf{H}X + N\right)\left(\sqrt{\frac{P}{N_T}}\mathbf{H}X + N\right)^*\right] \\
&= \mathbb{E}\left[\frac{P}{N_T}\mathbf{H}XX^*\mathbf{H}^*\right] + \mathbb{E}\left[NN^*\right] \\
&= \frac{P}{N_T}\mathbf{H}\mathbb{E}\left[XX^*\right]\mathbf{H}^* + \mathbf{I}_{N_R} \\
&= \frac{P}{N_T}\mathbf{H}\mathbf{I}_{N_T}\mathbf{H}^* + \mathbf{I}_{N_R} \\
&= \frac{P}{N_T}\mathbf{H}\mathbf{H}^* + \mathbf{I}_{N_R} \qquad (3.3.9)
\end{aligned}$$

Thus, the ergodic capacity of a MIMO communication system with N_T transmit antennas and N_R receive antennas when channel information is unavailable at the transmitter or receiver end can be calculated as

$$C = \mathbb{E}_{\mathbf{H}}\left[\log_2 \det\left[\mathbf{I}_{N_R} + \frac{P}{N_T}\mathbf{H}\mathbf{H}^*\right]\right] \quad \left[\frac{bits}{s \cdot Hz}\right] \qquad (3.3.10)$$

where $\mathbb{E}_{\mathbf{H}}$ means averaging over multiple realisations of the channel matrix $\mathbf{H}$.

CHAPTER 4

MICROWAVE THEORETIC PERFORMANCE METRICS

This chapter briefly discusses the microwave theoretic parameters that are being used in the performance evaluation of antennas discussed in this work.

4.1 Scattering Parameters

Linear multi-port networks are characterized by a number of equivalent circuit parameters, such as their transfer matrix, impedance matrix, admittance matrix, and scattering matrix. The scattering matrix gives a representation more in accord with direct measurements, and with the ideas of incident, reflected, and transmitted waves [51]. The impedance and admittance matrices relate total voltages and currents at the ports, whereas the scattering matrix relates voltage waves incident on the ports to those reflected from the ports. Conversions between these different forms are presented in the work of Frickey [52] and Marks et al. [53]. The scattering parameters can be calculated using network analysis techniques or can be measured directly with a vector network analyzer.

Figure 4.1 shows an arbitrary N-port microwave network. Variables a_n and b_n are the amplitudes of the incident voltage wave and reflected voltage wave at port n, respectively.

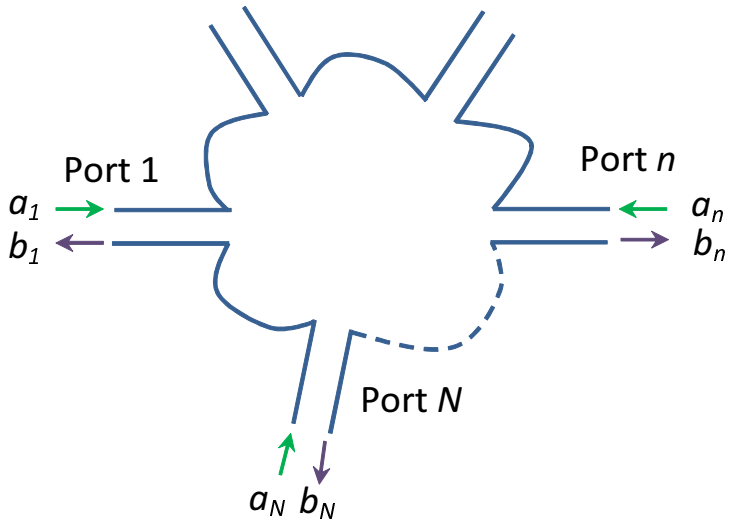

Figure 4.1: Arbitrary N-port microwave network.

These incident and reflected voltage waves are related as follows with the scattering matrix S:

$$\begin{bmatrix} b_1 \\ b_2 \\ \vdots \\ b_N \end{bmatrix} = \begin{bmatrix} S_{11} & S_{12} & \cdots & S_{1N} \\ S_{21} & S_{22} & \cdots & S_{2N} \\ \vdots & \vdots & \ddots & \vdots \\ S_{N1} & S_{N2} & \cdots & S_{NN} \end{bmatrix} \begin{bmatrix} a_1 \\ a_2 \\ \vdots \\ a_N \end{bmatrix} \tag{4.1.1}$$

A specific element of the scattering matrix can be calculated as

$$S_{ij} = \frac{b_i}{a_j}|_{a_k=0 for k\neq j} \tag{4.1.2}$$

This means that port j is driven with an incident wave of voltage a_j, and the reflected wave amplitude b_i is measured at port i to determine S_{ij}. All other ports, except the driving port j, must be terminated in matched loads to avoid reflections. This means that there are no incident waves at any port except at port j. S_{ii} is the reflection coefficient at port i, and S_{ij} is the transmission coefficient from port j to port i.

Reflection coefficient S_{ii}, which is also often denoted by Γ, gives a measure of how much

power is reflected at a port due to load mismatches. Only a portion of the available power from the generator is delivered to the, load due to load mismatches. This "loss" is called *return loss* (RL), and is defined as

$$RL = -20 \log |\Gamma| dB \tag{4.1.3}$$

Therefore, if the load is matched, the voltage reflection coefficient $\Gamma = 0$, or equivalently, the return loss $RL = \infty$, whereas $RL = 0$ dB (all incident power is reflected) if $|\Gamma| = 1$.

When the load is mismatched, the reflected wave exists in addition to the incident wave, thus resulting in standing waves on a line. This causes the magnitude of the voltage to vary. Therefore, the ratio of the maximum voltage to the minimum voltage, called *standing wave ratio* (SWR), gives a measure of the mismatch of a line defined [51] as

$$SWR = \frac{1 + |\Gamma|}{1 - |\Gamma|}. \tag{4.1.4}$$

The above quantity is also known as the *voltage standing wave ratio* and takes values one to infinity for $|\Gamma| = 0$ and $|\Gamma| = 1$, respectively. For a perfectly matched load $|\Gamma| = 0$ and $SWR = 1$. Often, the bandwidth of an antenna (range of frequencies that it operates) is given in terms of SWR or RL. Equations (4.1.3) and (4.1.4) can be used to convert one quantity to another. Table 4.1 shows a list of these quantities for comparison.

Table 4.1: COMPARISON OF SWR, REFLECTION COEFFICIENT, AND RETURN LOSS.

SWR	$\|\Gamma\|$	RL (dB)
1.0	0	∞
1.01	0.005	46.0
1.06	0.032	30.0
1.12	0.056	25.0
1.22	0.099	20.0
1.50	0.200	13.9
1.92	0.316	10.0
2.00	0.333	9.5
2.50	0.428	7.3
3.00	0.500	6.0

4.2 Antenna Efficiency

Radiation efficiency η of an antenna is defined as the ratio of the total radiated power to the total input power to the antenna. This can be calculated as the ratio of the antenna gain $G(\theta, \phi)$ to the directivity $D(\theta, \phi)$, which are written as [14]

$$G(\theta, \phi) = 4\pi \frac{U(\theta, \phi)}{P_{in}} \tag{4.2.1}$$

$$D(\theta, \phi) = 4\pi \frac{U(\theta, \phi)}{P_{rad}} \tag{4.2.2}$$

where $U(\theta, \phi)$ is the radiation intensity, and P_{in} and P_{rad} are the power accepted by the antenna and the total radiated power, respectively. Radiation intensity in a given direction is defined as the power radiated from an antenna per unit solid angle [14].

4.3 Antenna Bandwidth

The frequency range over which an antenna can effectively radiate is given by antenna bandwidth and it is usually centered on the resonant frequency. The impedance of an antenna changes with the frequency. This causes the amount of reflected power to vary with frequency. Generally the frequency range in which the standing wave ratio (SWR) is less

than 1.9:1 is considered as the bandwidth of an antenna. This figure can also be expressed as the power ratio between reflected wave and incident wave at an antenna input and is equivalent to -10 dB. The bandwidth of the antenna is determined by using S parameter simulations.

4.4 Mutual Impedance

The spatial channel matrix in equation (3.1.3), taking mutual coupling and correlation into consideration at both transmitter and receiver ends, is expanded [54] as

$$\mathbf{H} = \mathbf{M}_R(\eta_R \mathbf{R}_R)^{\frac{1}{2}} \mathbf{H}_{iid} (\eta_T \mathbf{R}_T)^{\frac{1}{2}} \mathbf{M}_T \tag{4.4.1}$$

where η_R and η_T are the receiver and transmitter efficiencies, respectively, and $\mathbf{M}_R$, $\mathbf{R}_R$, $\mathbf{M}_T$, and $\mathbf{R}_T$ denote the mutual coupling and correlation matrices at the receiver and transmitter, respectively. The transmitter and receiver coupling matrices are given by

$$\mathbf{M} = 2Z_0 \mathbf{Y} \tag{4.4.2}$$

where

$$\mathbf{Y} = [\dot{\mathbf{Z}}_M + \mathbf{Z}]^{-1} \tag{4.4.3}$$

is the array admittance matrix [54] (here, subscripts R and T are omitted for simplicity), Z_0 is the characteristic impedance of the transmission line connected to each antenna, $\dot{\mathbf{Z}}_M$ denotes the matching impedance of each antenna, and $\mathbf{Z}$ is the mutual impedance matrix.

The mutual impedance matrix $\mathbf{Z}$ can be computed in terms of the scattering matrix $\mathbf{S}$ [51] as

$$\mathbf{Z} = [\mathbf{I} + \mathbf{S}][\mathbf{I} - \mathbf{S}]^{-1} \tag{4.4.4}$$

where $\mathbf{I}$ is the identity matrix.

For performance evaluation, as will be described in the next subsection, a more realistic channel matrix is computed according to equation (4.4.1), whereas $\mathbf{H}$ in equation (3.1.3) has been used in most of the literature, e.g., the work of Forenza and Heath [15] and [7], for simplicity. In this work, the impedance of matching networks, $\dot{\mathbf{Z}}_M$, is not considered in the calculation of admittance matrices, $\mathbf{Y}$, and mutual impedance matrices, $\mathbf{Z}$, are calculated by using the scattering matrices, $\mathbf{S}$, obtained by FEKO simulations.

CHAPTER 5

FERRITE CIRCULAR PATCH ANTENNA (1-CPA)

This chapter describes the design of a miniaturized ferrite single circular patch antenna (Fe 1-CPA). Simulations are performed using the FEKO simulator. Then, its performance is compared to that of the two colocated stacked circular patch antenna (2-CPA) [7]. The 2-CPA generates higher-order orthogonal mode patterns for MIMO communication system applications, and so is the designed Fe 1-CPA. The Fe 1-CPA uses ferrite substrate materials for miniaturization purposes, whereas the 2-CPA uses dielectric substrate materials. The designed Fe 1-CPA is then fabricated using the available ferrite materials in the lab.

5.1 Modes of Circular Patch Antenna

The order of the supportable modes for a rectangular patch antenna can be changed by varying the width-to-length ratio. The supportable modes of this configuration can be found using the cavity model. Thus, the rectangular patch antenna has two degrees of freedom to select a supportable mode. The resonant frequency of the modes does not change with the dimensions of the rectangular patch. On the other hand, the supportable mode of a circular patch antenna can be changed by adjusting the radius. Thus, the circular patch antenna has one degree of freedom. And the resonant frequency of each supportable mode can be changed [14]. Hence, the circular patch has received considerable attention [14].

Resonant frequencies of a microstrip circular antenna, i.e., circular patch antenna, can be written as [14]

$$(f_r)_{mn} = \frac{1}{2\pi\sqrt{\mu\epsilon}}\left(\frac{\chi'_{mn}}{a}\right) \tag{5.1.1}$$

for TM_{mn} modes, where $\chi\prime_{mn}$ represents the zeros of the derivative of the Bessel function $J_m(x)$ of the first kind of order m, a is the radius of the antenna, and μ and ϵ represent the permeability and the permittivity of the substrate material, respectively. Also, $\mu = \mu_r\mu_0$ and $\epsilon = \epsilon_r\epsilon_0$, where μ_r and ϵ_r are the relative permeability and relative permittivity of the substrate material, respectively, $\mu_0 = 4\pi \cdot 10^{-7}$ H/m, and $\epsilon_0 = 8.854 \cdot 10^{-12}$ F/m. Fields fringe at the edge of the patch. This effect is not taken into consideration in equation (5.1.1). A radius correction is introduced by using an effective radius as [14]

$$a_e = a\left\{1 + \frac{2h}{\pi a\epsilon_r}\left[\ln\left(\frac{\pi a}{2h}\right) + 1.7726\right]\right\}^{\frac{1}{2}} \tag{5.1.2}$$

where h is the height of the circular patch antenna. Since $\chi\prime_{mn}$ increases as the mode index m increases for $m = 1, 2, 3$, the highest mode that can be excited is limited by the antenna radius a. In other words, the radius of the circular patch must be increased if a higher mode wants to be generated for a given resonance frequency. Thus, from the antenna miniaturization point of view, the highest mode that can be supported in the CPA is constrained by the given antenna radius. If the conventional substrates are used in patch antennas, then the dielectric materials have a relative permeability of one, which implies that there is no more room for minimization of a in equation (5.1.1). In fact, it is desirable to have a higher mode for higher pattern diversity effects. Hence, the main focus of this paper is to replace the dielectric substrate with a material of higher permeability μ to reduce the size of the circular patch antenna. Specifically, further size reduction can be achieved according to equation (5.1.1), if a ferrite substrate material of a relative permeability μ_r greater than one is used for a given resonance frequency.

5.2 Radiation Characteristics

This section describes the far field of a circular patch antenna when multiple feed probes are present in a single antenna. The radiated electric field of a CPA in the far field can be written as [14]

$$\overrightarrow{E}_m = \frac{e^{-jk_0r}}{r}\left[\underline{E}_{m,\theta}\overrightarrow{\theta} + \underline{E}_{m,\phi}\overrightarrow{\phi}\right] = \frac{e^{-jk_0r}}{r}\underline{E}_m \tag{5.2.1}$$

where r is the radius (distance) from the origin to the point from which the radiated field is observed, k_0 is the wave number (free-space propagation constant), and $\overrightarrow{\theta}$ and $\overrightarrow{\phi}$ are the unit vectors in the elevation angle θ and azimuth angle ϕ, respectively. Here the subscript m represents the feed probe (or port) index at the transmitter or receiver antenna, and $\underline{E}_m$ represents the generated electric field pattern only as a function of the azimuth and elevation angles corresponding to the m-th feed probe active in the circular patch antenna. Radial dependency is not included. Electric field components $\underline{E}_{m,\theta}$ and $\underline{E}_{m,\phi}$, which are over the elevation angle and the azimuth angle, respectively, can be expressed as [26]

$$\begin{aligned} E^{(n)}_{m,\theta} = {} & e^{j\frac{n\pi}{2}}\frac{V_0^{(n)}k_0a}{2}\cos(n(\phi-\phi_0)) \\ & \times (J_{n+1}(z) - J_{n-1}(z)) \end{aligned} \tag{5.2.2}$$

$$\begin{aligned} E^{(n)}_{m,\phi} = {} & -e^{j\frac{n\pi}{2}}\frac{V_0^{(n)}k_0a}{2}\cos(\theta)\sin(n(\phi-\phi_0)) \\ & \times (J_{n+1}(z) + J_{n-1}(z)) \end{aligned} \tag{5.2.3}$$

where n is the mode number, ϕ_0 is the reference angle that corresponds to the peak magnetic current $V_0^{(n)}$, a is the radius of the antenna, and $J_n(z)$ is the Bessel function of the first kind of order n, where $z = k_0 \cdot a \cdot sin(\theta)$. According to equations (5.2.2) and (5.2.3), it can be observed that any azimuthal mode n other than zero can be rotated by $\phi_2 - \phi_1$ and will be orthogonal to its unrotated form. This means that the same mode can be used to provide

two radiation patterns that are orthogonal. Therefore, two-branch diversity can be achieved by the same azimuthal mode [25]. Generating two orthogonal patterns of the same mode can be achieved when feed positions are displaced azimuthally as [25]

$$\phi_2 - \phi_1 = \frac{(2q-1)\pi}{2n}, \quad q = 1, 2, \cdots, 2n. \tag{5.2.4}$$

Figure 5.1 shows numerically calculated ideal electric field components $E_{m,\theta}^{(n)}$ for mode $n = 3$ over the azimuth angle according to equation (5.2.2), where the elevation angle is set to $\theta = \pi/2$.

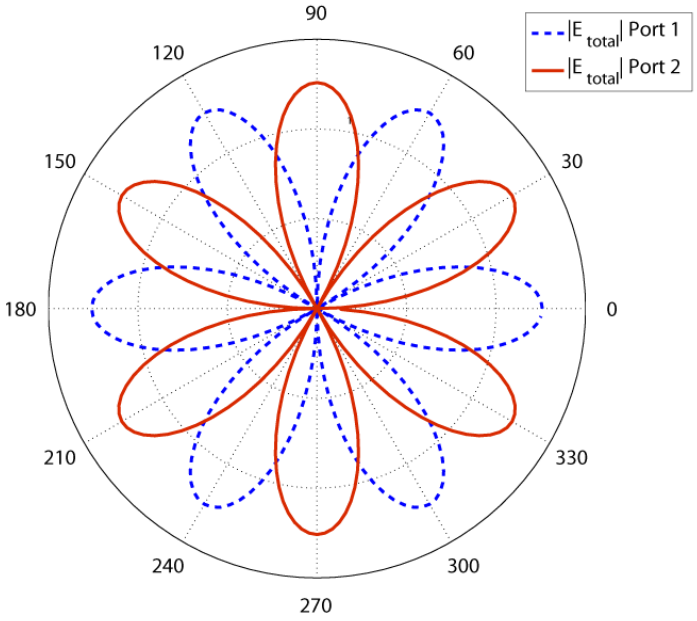

Figure 5.1: Superimposed ideal radiation patterns of circular patch antenna excited with mode $n = 3$. Far-field patterns calculated according to equations (5.2.2) and (5.2.3) for $\theta = \pi/2$. Ports 1 and 2 correspond to $\phi_0 = 0$ and $\phi_0 = \pi/6$, respectively.

The two orthogonal radiation patterns correspond to two reference angles $\phi_0 = 0$ and $\phi_0 = \pi/6$. The far-field electric field component for each reference angle was calculated individually, and then the radiation patterns were overlaid and shown. Each reference angle

corresponds to the angular position of the feed pin of the circular patch antenna.

5.3 Simulation Setup and Results

The geometry in Figure 5.2 was used in the FEKO electromagnetic simulation tool to obtain far-field radiation patterns and S-parameters of the Fe 1-CPA antenna.

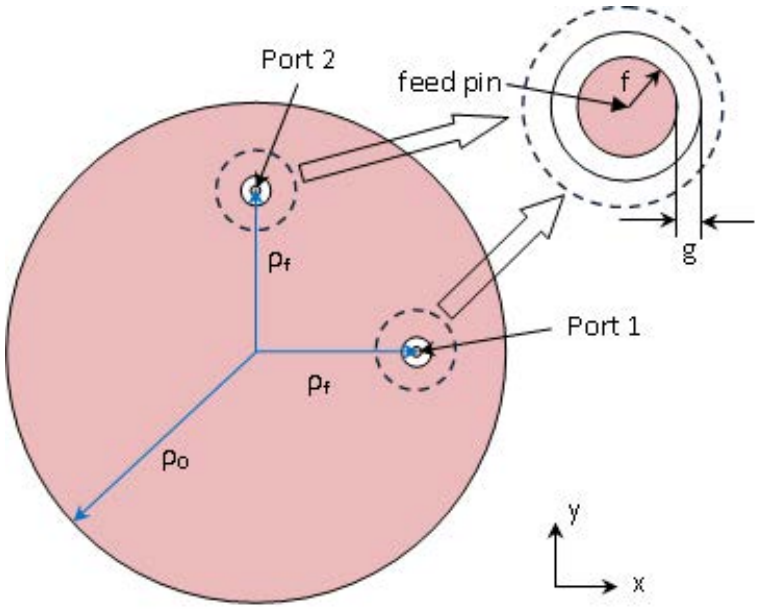

Figure 5.2: Geometry of Fe 1-CPA design (top view.)

Electric field components over the azimuth plane were used to calculate the spatial correlation coefficients r_{11}, r_{22}, r_{12}, and r_{21}, according to equation (3.2.1). S-parameters were used to determine the frequency bandwidth of the antenna, and the mutual impedance matrix $\mathbf{Z}$ according to equation (4.4.4). Radius ρ_0 of the CPA, radial position ρ_f of the feed pins, height h of the substrate, annular gap g, and radius f were found empirically. Table 5.1 compares the physical dimensions and material parameters of the proposed Fe 1-CPA with those of the dielectric 2-CPA in [7].

Table 5.1: PARAMETERS OF DIELECTRIC 2-CPA and FERRITE 1-CPA.

	Dielectric 2-CPA	Ferrite 1-CPA
$h^{(1)}(mm)$	9.0	7.0
$\rho_0^{(1)}(mm)$	52.8	25.5
$\rho_{gp}^{(1)}(mm)$	105.6	25.5
$\rho_f^{(1)}(mm)$	47.5	12.7
$\epsilon_r^{(1)}$	2.2	7.0
$\mu_r^{(1)}$	1.0	2.0
$h^{(2)}(mm)$	7.0	N/A
$\rho_0^{(2)}(mm)$	27.0	N/A
$\rho_{gp}^{(2)}(mm)$	48.6	N/A
$\rho_f^{(2)}(mm)$	21.6	N/A
$\epsilon_r^{(2)}$	8.0	N/A
$\mu_r^{(2)}$	1.0	N/A
volume (cm^3)	367.4 (100%)	14.3 (3.89%)
weight (g)	808.3 (100%)	76.5 (9.46%)

Z-type hexagonal ferrite: 5.35 [g/cm^3], Duroid : 2.2 [g/cm^3] are used for the weight calculations.

The proposed ferrite circular patch contains two feed probes that are azimuthally displaced by $\pi/2$ in a single circular patch antenna. An annular ring around each feed point was introduced to compensate probe inductance [55], [56]. To obtain the far field radiation pattern of Fe 1-CPA, each port was excited separately as well as simultaneously. Figures 5.3 and 5.4 show the electric field component of the far-field over $\theta \in [0, \pi/2]$ and $\phi \in [0, 2\pi]$ when the ports were excited at $\phi = 0$ and $\phi = \pi/2$, respectively.

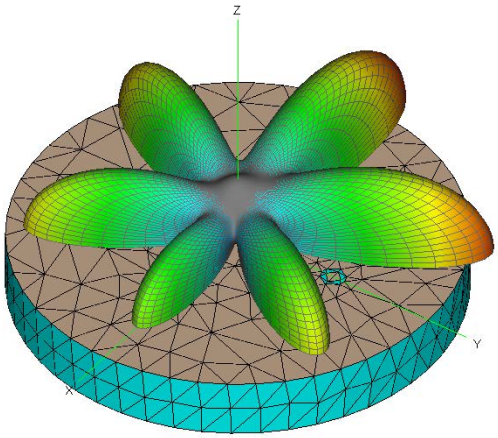

Figure 5.3: Three-dimensional radiation patterns of circular patch antenna excited with mode $n = 3$: Fe 1-CPA using FEKO. Only port at $\phi = 0$ was excited.

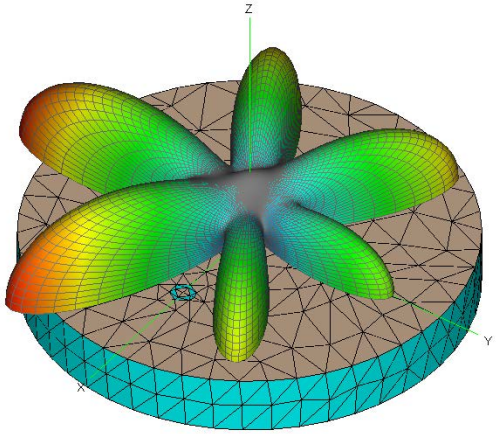

Figure 5.4: Three-dimensional radiation patterns of circular patch antenna excited with mode $n = 3$: Fe 1-CPA using FEKO. Only port at $\phi = \pi/2$ was excited.

Far-field gain patterns when each port was excited alone are overlaid and shown in Figure 5.5 for $\theta = \pi/2$ and $\phi \in [0, 2\pi]$. The following antenna parameters were used in the above simulations: $\rho_0 = 2.55$ cm, $\rho_f = 0.5\rho_0$, $h = 0.7$ cm, $f = 0.1$ cm, $g = 0.05$ cm, $\epsilon_r = 7.0$, and $\mu_r = 2.0$.

Note that the far-field radiation patterns were rotated by $\pi/2$ in a counterclockwise direction, which corresponds to the angular separation of the two feed probes (see Figures

5.3, 5.4, and 5.5).

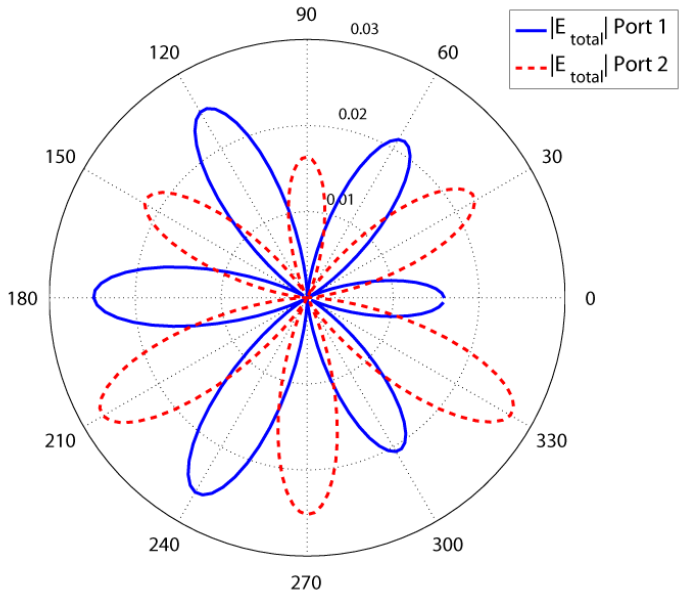

Figure 5.5: Superimposed radiation patterns of Fe 1-CPA excited with mode $n = 3$ when ports are excited consecutively, and radiation patterns are overlaid: Using FEKO.

It is evident from Figure 5.5 that the far-field radiation patterns generated when each feed pin was individually excited are orthogonal. In the work of Forenza and Heath [7], these individual patterns were also generated separately and overlaid to show the orthogonality using the 2-CPA. If the two ports are simultaneously excited, then the superimposed pattern shows only six lobes instead of twelve, and the lobe peaks appear between the lobe peaks, as depicted in Figures 5.3 and 5.4. This paper does not employ the superimposed pattern but rather the individual patterns for the capacity and BER performance evaluation as was done by Forenza and Heath [7]. This is because spatial multiplexing is assumed between the in-phase and quadrature-phase components at the transmitter and the receiver to achieve pattern diversity [57].

Note also that whenever a maximum occurs in the electric field corresponding to feed pin

1, a minimum occurs in the electric field corresponding to feed pin 2, and vice-versa. When compared with the ideal radiation patterns in Figure 5.1, the results obtained by FEKO simulations, as shown in Figure 5.5, which are based on the Method of Moments, are not symmetrical over the azimuth angle. This is because in the cavity model, the feed probes are not taken into account when deriving equations (5.2.2) and (5.2.3), whereas the Method of Moments considers the probe feeds in its calculations [14], [58].

Figure 5.6 shows the simulated S-parameters of the Fe 1-CPA. The magnitudes of the reflection coefficients $|S_{11}|$ and $|S_{22}|$ of each port are well below the -10 dB at 2.45 GHz center frequency and have a frequency bandwidth of 25 MHz. The magnitudes of the transmission coefficients $|S_{12}|$ and $|S_{21}|$ are below -20 dB over the entire frequency range from 2.3 GHz to 2.6 GHz, which implies a very low-signal coupling between the two feed probes. Figure 5.7 shows the corresponding normalized input impedance loci of port 1 and port 2.

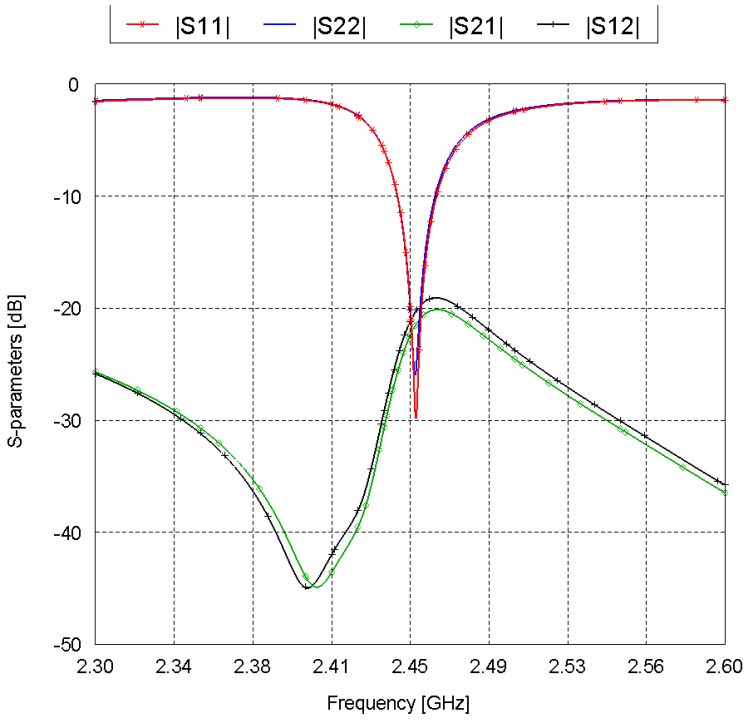

Figure 5.6: Simulated S-parameters of Fe 1-CPA: Using FEKO.

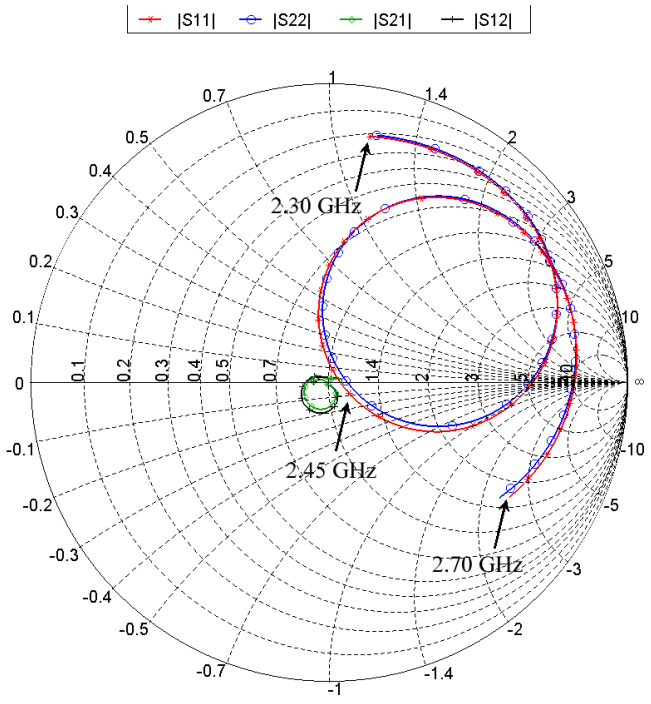

Figure 5.7: Input impedance loci of Fe 1-CPA: Using FEKO.

5.4 Parameter Comparison of Fe 1-CPA and Dielectric 2-CPA

Table 5.1 previously listed the physical parameters of the Fe 1-CPA and the dielectric 2-CPA presented in the work of Forenza and Heath [7]. According to equation (5.1.1), the calculated radius of the Fe 1-CPA is 2.19 cm at the resonant frequency $f_r = 2.45$ GHz, $\epsilon_r = 7.0$, $\mu_r = 2.0$, and $n = 3$. The above calculation does not take into account fringing. The effective radius a_e is 2.24 cm, which is calculated with the fringe effect from equation (5.1.2). This value is very close to the value of 2.55 cm found empirically by FEKO simulations. The height of the Fe 1-CPA is 0.7 cm, which equals 0.0572λ at $f_r = 2.45$ GHz. This satisfies the assumption of the substrate height $h < 0.05\lambda_0$ approximately, that the fields along the z-axis are constant, and that only the TM modes are present in the patch antenna [14]. Note that the volume of Fe 1-CPA can be 25.7 times smaller than that of the 2-CPA, and the weights of the Fe 1-CPA can be 10 times smaller than that of the 2-CPA, respectively, due to miniaturization.

5.5 Performance Evaluation in Clustered MIMO Channels - Fe 1-CPA

Electric field components over the azimuth plane were obtained from the FEKO far field simulation results, and then correlation coefficients were calculated. Figure 5.8 shows the calculated correlation coefficients using equation (3.2.1).For comparisons, Figure 5.9 also shows the correlated coefficients that were calculated using equations (14) and (20) of the work of Forenza and Heath [15] with ideal electric fields.

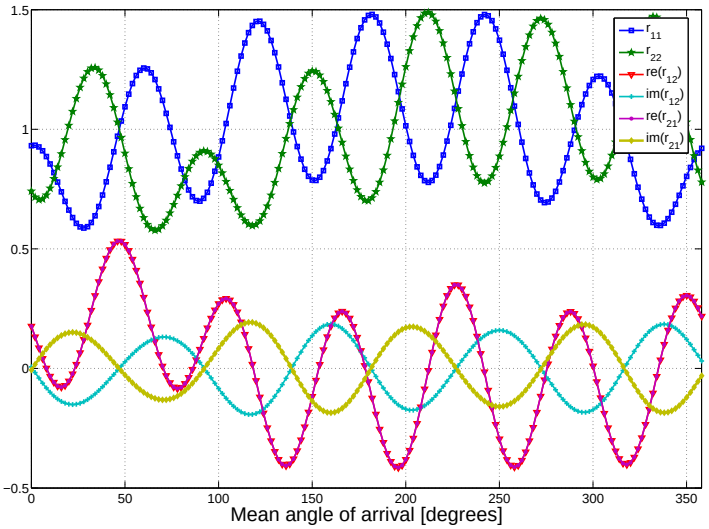

Figure 5.8: Correlation coefficients of Fe 1-CPA calculated according to equation (3.2.1) using realistic radiation patterns shown in Figure 5.5.

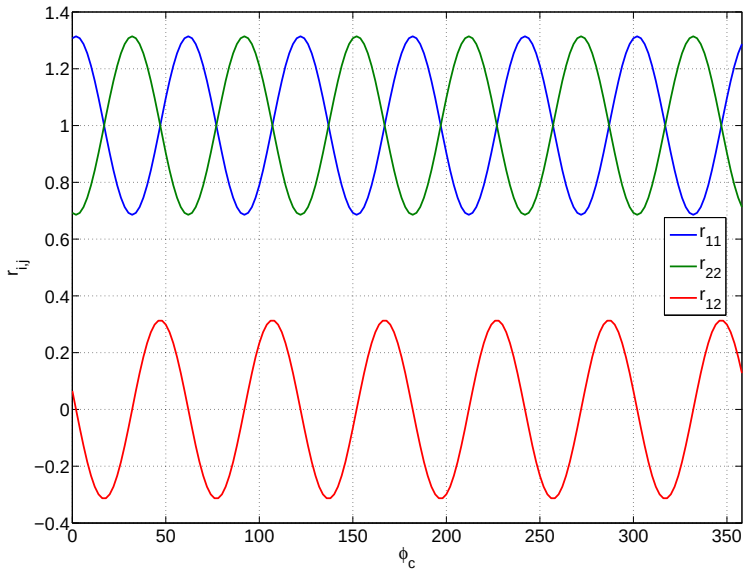

Figure 5.9: Correlation coefficients of Fe 1-CPA calculated according to equation (14) and equation (20) in [15] with ideal electric fields.

The deviations of the correlation coefficients from the sinusoidal form can be explained due to the irregular lobes in the far-field radiation patterns shown previously in Figure 5.5. As shown in Figure 5.5, the radiation power of the pattern generated by exciting port 1 is strong at azimuth angles 0°, 60°, and 300°, whereas that of the pattern generated by exciting port 2 is weak at those angles and strong at azimuth angles 30°, 90°, and 150°. Hence, the correlation coefficients of r_{11} and r_{22} show the peaks at (0°, 60°, 300°) and (30°, 90°, 150°), respectively, in Figure 5.8.

The calculated correlation coefficients in Figure 5.8 are used to find the correlation matrices $\mathbf{R}_T$ and $\mathbf{R}_R$ in equation (4.4.1), which are necessary to calculate the ergodic capacity of the channel in equation (3.3.3) by means of spatially correlated signals. The following scattering parameters obtained through FEKO simulations were used to calculate the coupling matrices $\mathbf{M_T}$ and $\mathbf{M_R}$: $S_{11} = 0.185\angle 47°$, $S_{12} = 0.044\angle -104°$, $S_{21} = 0.073\angle -115°$, and $S_{22} = 0.173\angle 34°$. The radiation efficiency η of the Fe 1-CPA was calculated with the FEKO simulation results and found to be 8.4%. These parameters, $\mathbf{M_T}$, $\mathbf{M_R}$, and η, are also required to calculate the channel matrix $\mathbf{H}$ according to equation (4.4.1), and are used in the capacity equation (3.3.3) and bit error rate evaluations.

Figure 5.10 shows a three-dimensional plot of an ergodic capacity averaged over 10,000 channel realizations, the azimuth angle, and SNR. A two dimensional plot of the ergodic capacity shown in Figure 5.10 is shown in Figure 5.11, in which SNR is used as a parameter. It is observed that the capacity increases with increasing SNR, which is expected from equation (4) in the work of Forenza and Heath [5]. A capacity increase of 1.6 bits/s/Hz can be observed for a 3 dB signal-to-noise ratio improvement from 27 dB to 30 dB.

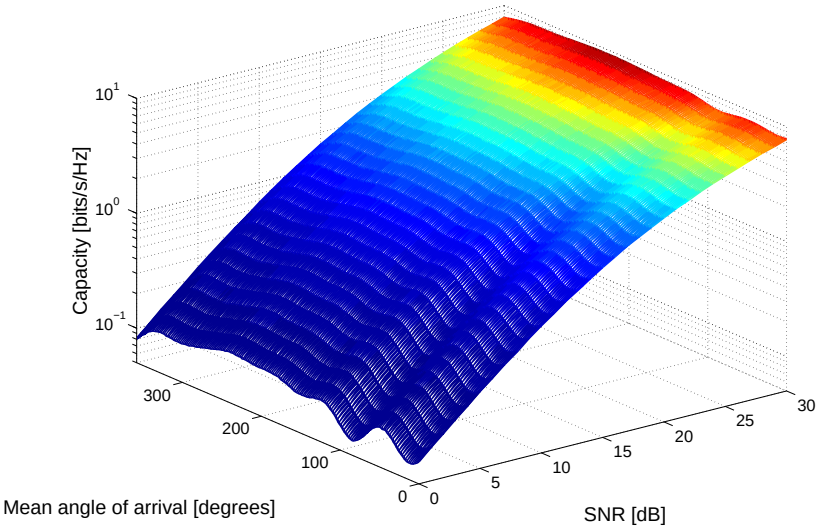

Figure 5.10: Ergodic capacity of Fe 1-CPA vs. angle of arrival and signal-to-noise.

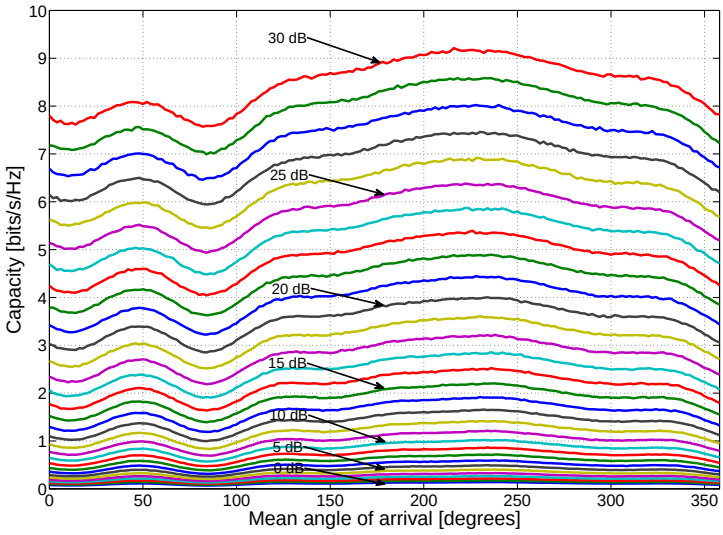

Figure 5.11: Ergodic capacity of Fe 1-CPA vs. angle of arrival with signal-to-noise ratio as parameter.

Expected 2 bits/s/Hz capacity increment for a 2×2 MIMO system was not yet achieved for the 1-CPA system at these simulated SNR values. The average capacity over the mean angle of arrival at 0 dB, 10 dB, 20 dB, and 30 dB are 0.11 bits/s/Hz, 0.83 bits/s/Hz, 3.5 bits/s/Hz, and 8.5 bits/s/Hz, respectively. The standard deviations of the capacity over the mean angle arrival at above SNR values are $2.03 \cdot 10^{-2}$ bits/s/Hz, $1.28 \cdot 10^{-1}$ bits/s/Hz, $3.42 \cdot 10^{-1}$ bits/s/Hz, and $5.10 \cdot 10^{-1}$ bits/s/Hz, respectively.

Figure 5.12 shows a three-dimensional plot of the BER, SNR, and mean angle of arrival.

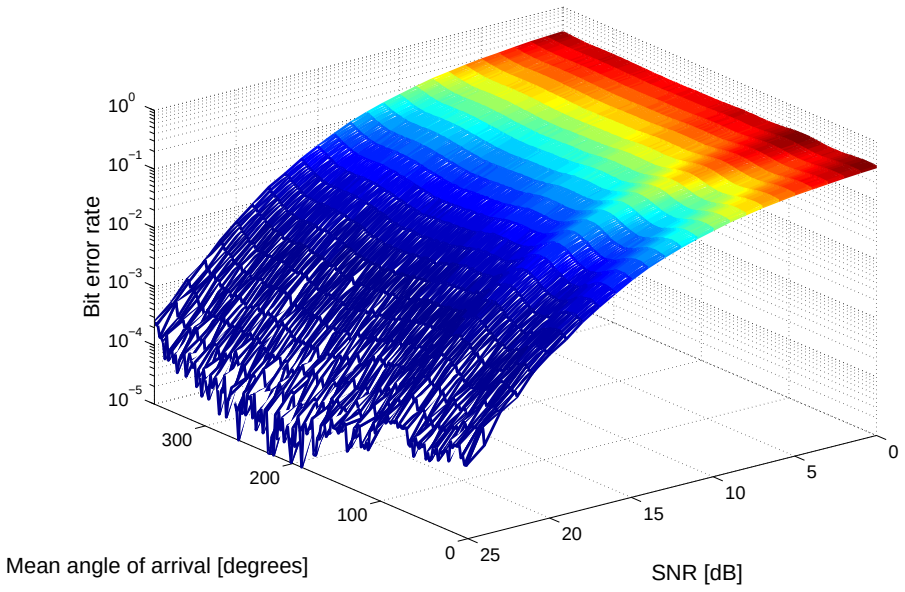

Figure 5.12: Bit error rate of Fe 1-CPA vs. angle of arrival.

As expected, BER decreases as SNR increases. For the BER plot in Figure 5.12, Alamouti's (2×2) space-time block code (STBC) encoding and decoding were used with the Fe 1-CPA at the TX and RX [49], and the bit error rate of the Fe 1-CPA was compared with a conventional (2×2) STBC MIMO system in which two spatially separated antennas were employed. Figure 5.13 shows BER versus the angle of arrival, with SNR as a parameter. The BER was not averaged over sufficient channel realizations. This is why the BER curves show

a coarse nature (see Figure 5.13). Standard deviations of the bit error rate over the angle of arrival are $1.42 \cdot 10^{-2}$, $2.25 \cdot 10^{-2}$, and $8.56 \cdot 10^{-5}$ at 0 dB, 10 dB, and 25 dB, respectively. It is observed that the non-symmetric radiation patterns show minor effects on BER of the system when SNR is high, as opposite to what is observed for the capacity case.

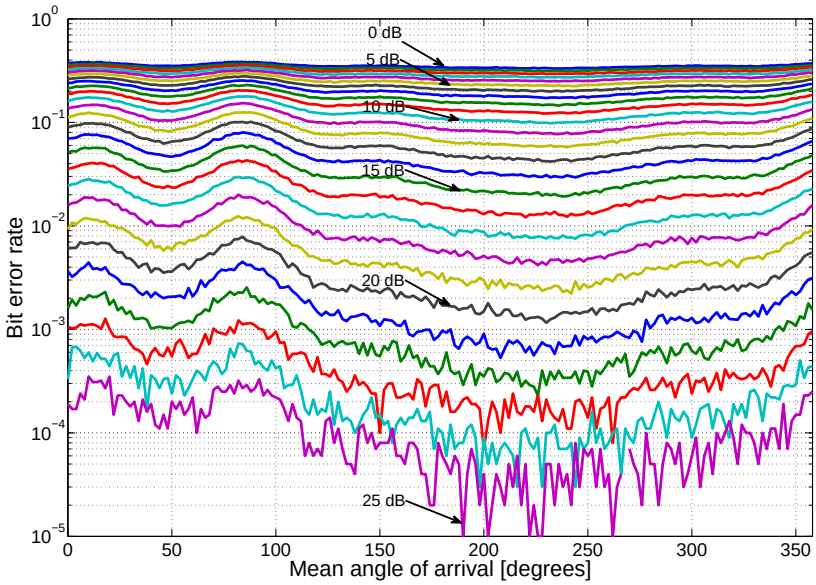

Figure 5.13: Bit error rate of Fe 1-CPA vs. angle of arrival with signal-to-noise ratio as a parameter.

Figure 5.14 compares the BER of the Fe 1-CPA with that of the conventional (2×2) STBC MIMO system. The BER of the Fe 1-CPA was calculated by taking only the spatial correlation into consideration equation (3.1.3) or by taking the spatial correlation as well as radiation efficiency and mutual coupling of the antenna into consideration equation (4.4.1).

Note that equation (4.4.1) becomes equation (3.1.3) when $\mathbf{M_T} = I$ and $\eta = 100\%$. Averaged BER over the angle of arrival is shown. The 1-CPA without taking the radiation efficiency and mutual coupling into consideration performs slightly inferior to the conventional (2×2) STBC MIMO system for simulated signal-to-noise ratios.

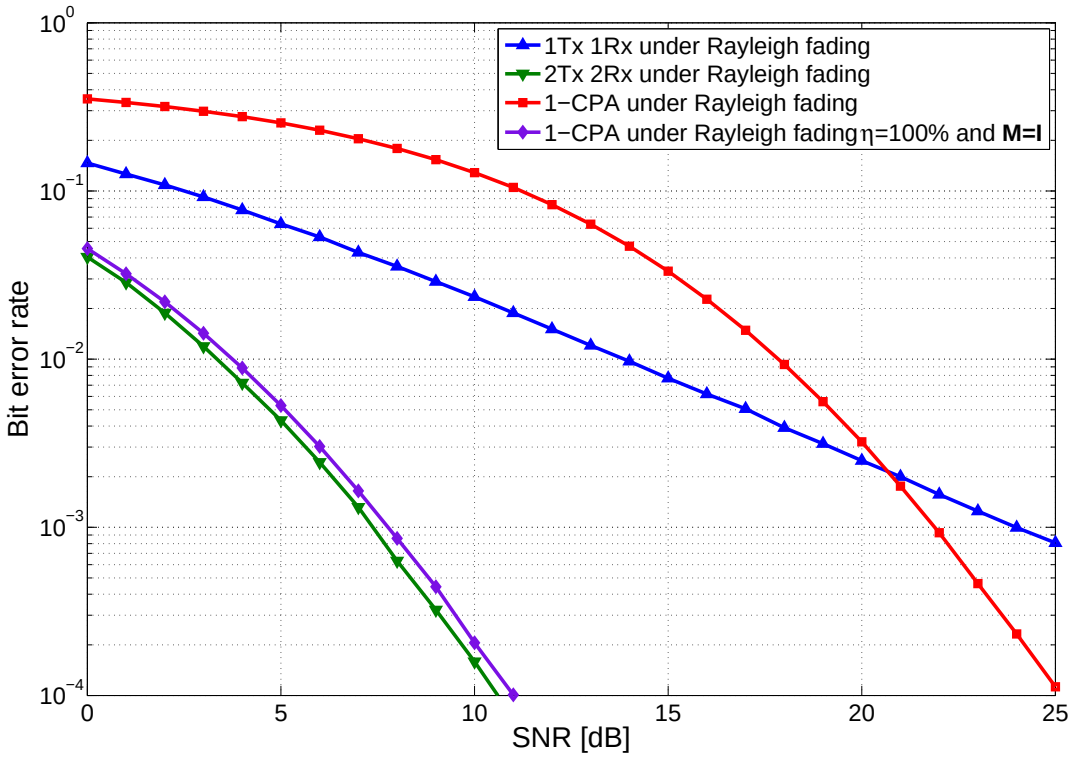

Figure 5.14: Bit error rate comparison of 2×2 MIMO vs. Fe 1-CPA using Alamouti scheme under Rayleigh fading channel.

For example, the Fe 1-CPA requires 0.5 dB higher SNR than the conventional (2×2) STBC MIMO system to achieve 10^{-3} BER. When both the radiation efficiency and the mutual coupling are taken into account, the Fe 1-CPA requires 14.7 dB higher SNR than the conventional (2×2) STBC MIMO system to achieve the same BER. This inferior performance of the Fe 1-CPA is caused by low-radiation efficiency of the antenna, which is merely 8%. High-loss magnetic material used for the substrate causes the low-radiation efficiency of the antenna.

CHAPTER 6

FERRITE ANNULAR RING ANTENNA (1-ARA)

The design of a miniaturized ferrite single circular patch antenna (Fe 1-ARA) is described in this chapter. Simulations were performed using the FEKO simulator. Then, its performance was compared to that of the two colocated stacked circular patch antenna (2-CPA) in the work of Forenza and Heath [7]. Fe 1-ARA was also designed to excite mode 3 as of 2-CPA. A ferrite substrate materials was used for miniaturization purposes. The designed Fe 1-ARA was then fabricated using the available ferrite materials in the lab.

6.1 Radiation Characteristics

The radiation characteristics of a closed-ring microstrip antenna were examined by Sultan [59]. Electric fields over the elevation angle and azimuth angles, respectively, are given by

$$E_\theta = -C\cos(n\phi)\left[K_1 B_1(a_{ae}) - K_2 B_1(a_{ie})\right] \tag{6.1.1}$$

$$E_\phi = Cn\cos(\theta)\sin(n\phi)\left[K_1 B_2(a_{ae}) - K_2 B_2(a_{ie})\right] \tag{6.1.2}$$

where $C = j^n h k_0 E_0 e^{-jk_0 r/r}$, $K_1 = r_{ae}A_n(r_{ae})$, $K_2 = r_{ie}A_n(r_{ie})$, $a_{ae} = k_0 r_{ae}\sin(\theta)$, $a_{ie} = k_0 r_{ie}\sin(\theta)$, $A_n(x) = J_n(k_{nm}x) - C_1 Y_n(k_{nm}x)$, $C_1 = \frac{J_n'(k_{nm}r_{ie})}{Y_n'(k_{nm}r_{ie})}$, $B_1(x) = J_{n-1}(x) - \frac{nJ_n(x)}{x}$, and $B_2(x) = \frac{J_n(x)}{x}$, and the dummy variable x refers to r_{ae}, r_{ie}, a_{ae} or a_{ie}; k_{nm} is the mode number given by $k_{nm} = 2n/(r_{ae} + r_{ie})$; r_{ae} and r_{ie} are the inner and outer radii of the equivalent cavity model of the closed-ring microstrip antenna, h is the height of the antenna; and $J_n(x)$ and $Y_n(x)$ are the ordinary Bessel functions of the first and second kind, respectively.

6.2 Simulation Setup

Figure 6.1 shows the top view of the Fe 1-ARA.

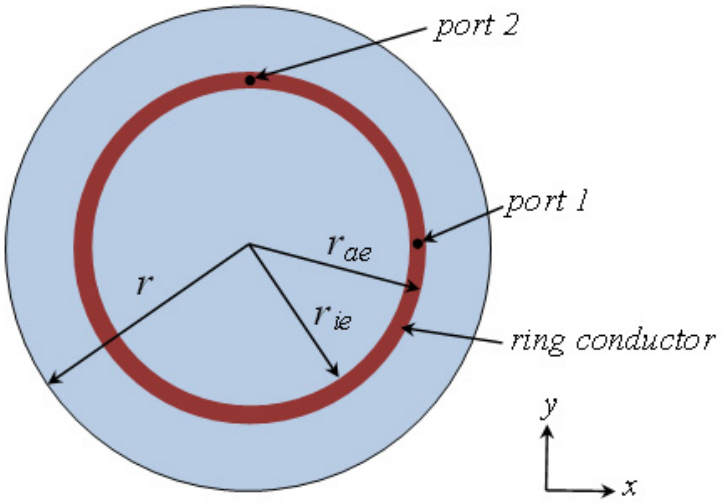

Figure 6.1: Geometry of Fe 1-ARA design (top view.)

This geometry was used in the FEKO simulations to generate the S-parameters and far-field radiation patterns. Simulation results shown in this subsection were generated using the following parameter values: $r = 30$ mm, $r_{ae} = 27$ mm, $r_{ie} = 25$ mm, and height of the antenna $h = 6.5$ mm. For the ferrite substrate, relative permittivity, ϵ_r, of 5 and relative permeability, μ_r, of 2.2 were used. The corresponding loss tangents associated with the permittivity and permeability were $tan\delta_\epsilon = 0.001$ and $tan\delta_\mu = 0.01$, respectively.

Figures 6.2 and 6.2 show the far-field radiation patterns over the azimuth and elevation angles, associated with each port. Port 1 alone was activated in Figure 6.2, and port 2 alone was activated in Figure 6.3. Total gain of the antenna for each case is shown in decibels. The radiation pattern corresponding to each port over the azimuth angle ($\theta = \pi/2$) was extracted. Figure 6.4 shows the overlaid radiation patterns. It is evident from these figures that the radiation patterns are approximately orthogonal. These radiation patterns were generated at 2.44 GHz.

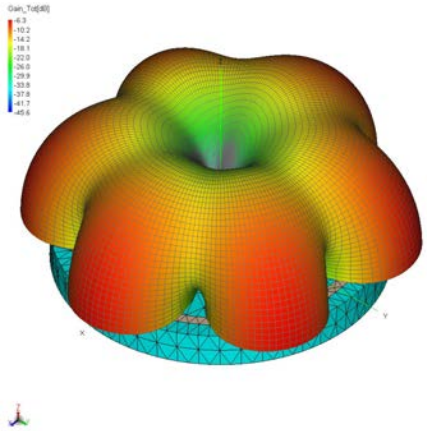

Figure 6.2: Three-dimensional gain patterns of Fe 1-ARA in decibels. Only port at $\phi = 0$ was excited.

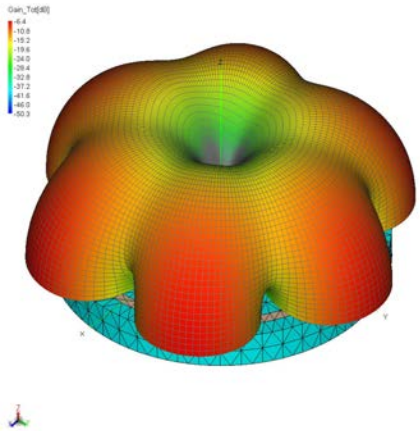

Figure 6.3: Three-dimensional gain patterns of Fe 1-ARA in decibels. Only port at $\phi = \pi/2$ was excited.

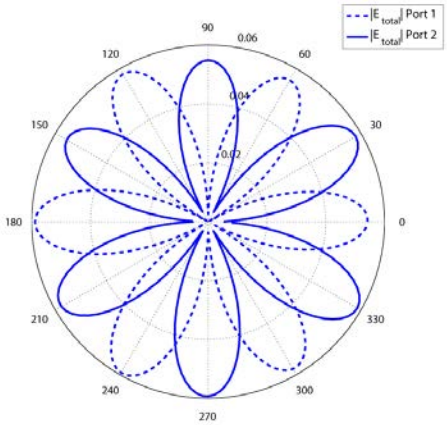

Figure 6.4: Two-dimensional overlaid gain patterns of Fe 1-ARA.

6.3 Performance Evaluation in Clustered MIMO Channels - Fe 1-ARA

Figure 6.5 shows the simulated S-parameters $|S_{11}|$, $|S_{22}|$, $|S_{12}|$, and $|S_{21}|$ for the geometry shown in Figure 6.1.

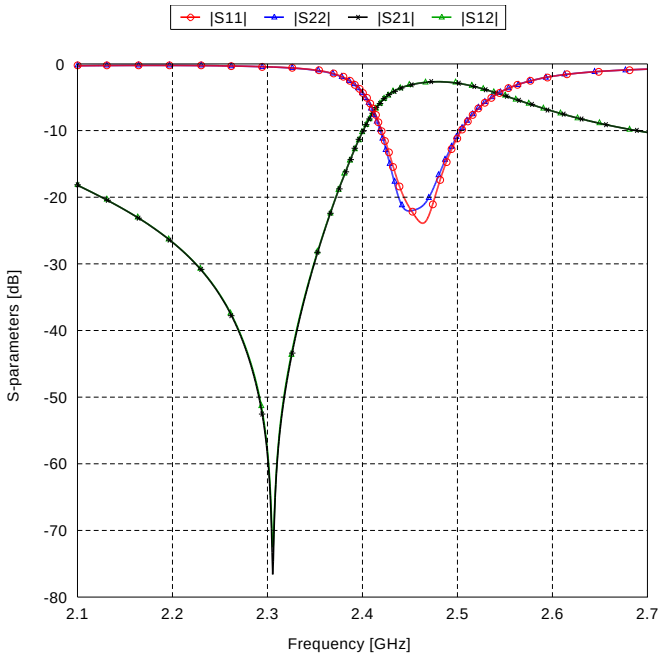

Figure 6.5: Simulated S-parameters of Fe 1-ARA.

A 10-dB bandwidth of 70 MHz can be achieved according to $|S_{11}|$ and $|S_{22}|$ values centered at 2.44 GHz. This frequency is approximately equal to that of the 2-CPA in [7]. High signal coupling between two ports is observed from $|S_{12}|$ and $|S_{21}|$ values. This is a disadvantage of the Fe 1-ARA.

Figure 6.6 shows the calculated correlation coefficients using equation (3.2.1) and the linear scaled radiation patterns corresponding to that shown in Figure 6.4.

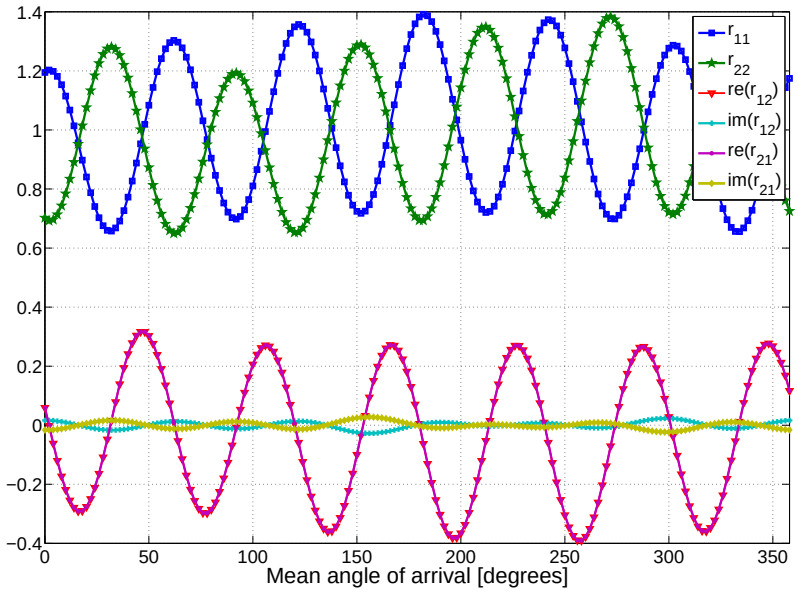

Figure 6.6: Correlation coefficients of Fe 1-ARA calculated according to equation (3.2.1) using radiation patterns shown in Figure 6.4.

The r_{11} and r_{22} values oscillate around one, and r_{12} and r_{21} oscillate around zero. These oscillations are expected due to oscillating lobes of the radiation patterns in Figure 6.4. As can be seen, the oscillations are not regular. Correlation coefficients in Figure 6.6 were used to calculate ergodic capacity. The following scattering parameters obtained by FEKO simulations were used to calculate the coupling matrices $\mathbf{M}$. $S_{11} = 0.0636\angle -4°$, $S_{12} = 0.678\angle 88°$, $S_{21} = 0.689\angle 88°$, and $S_{22} = 0.0672\angle -4°$. The radiation efficiency η of the Fe 1-ARA obtained through FEKO simulations was 7.6%.

Figure 6.7 shows a three-dimensional plot of the capacity averaged over 10,000 channel realizations, SNR, and the angle of arrival. Figure 6.8 shows the capacity versus the angle of arrival with SNR as a parameter. It is evident that capacity increases as SNR increases, as expected.

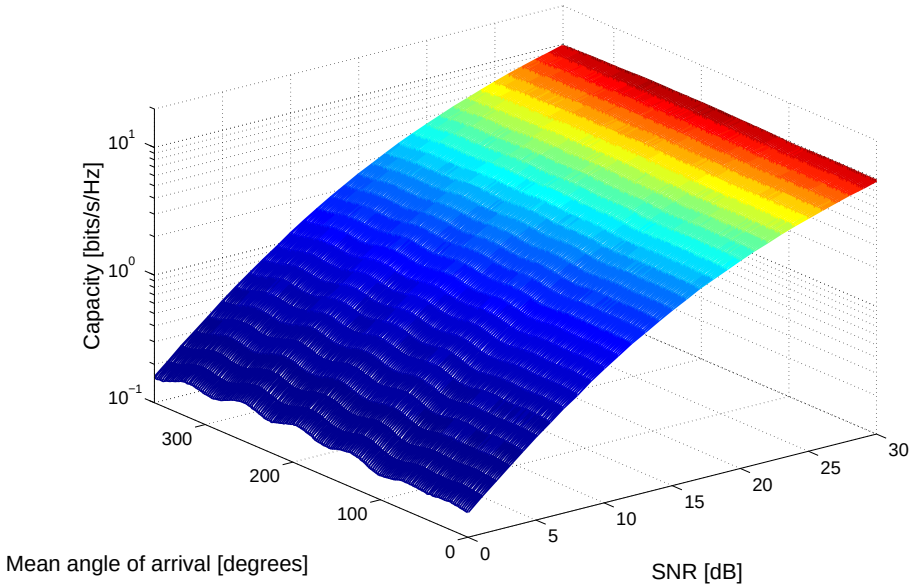

Figure 6.7: Ergodic capacity of Fe 1-ARA vs. angle of arrival and signal-to-noise ratio.

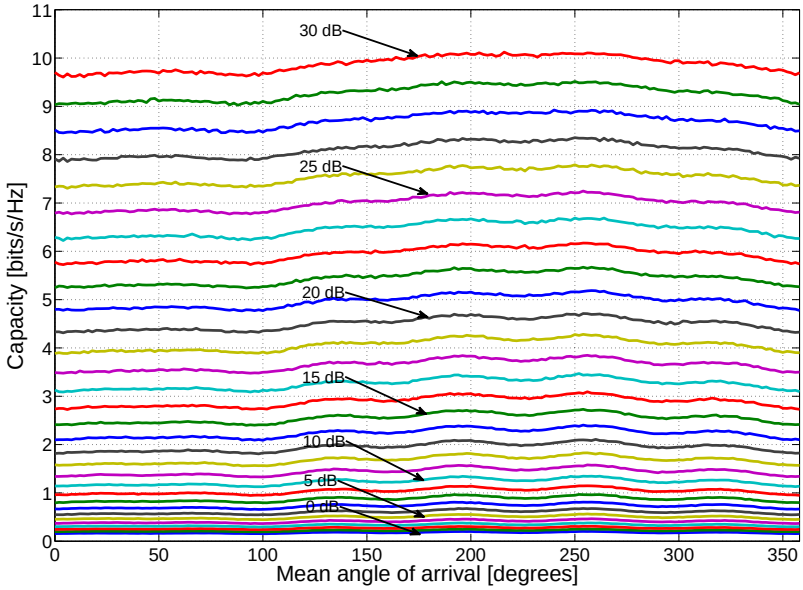

Figure 6.8: Ergodic capacity of Fe 1-ARA vs. angle of arrival with signal-to-noise ratio as a parameter.

A capacity increase of 1.8 bits/s/Hz can be observed for 3 dB signal-to-noise ratio improvement from 27 dB to 30 dB. Expected 2 bits/s/Hz capacity increment for a 2×2 MIMO system is almost achieved for the 1-ARA system for higher than 27 dB signal-to-noise ratios. The average capacity over the mean angle of arrival at 0 dB, 10 dB, 20 dB, and 30 dB are 0.18 bits/s/Hz, 1.23 bits/s/Hz, 4.5 bits/s/Hz, and 9.8 bits/s/Hz, respectively. Standard deviations of the capacity over the mean angle arrival above SNR values are $1.28 \cdot 10^{-2}$ bits/s/Hz, $6.28 \cdot 10^{-2}$ bits/s/Hz, $1.22 \cdot 10^{-1}$ bits/s/Hz, and $1.60 \cdot 10^{-1}$ bits/s/Hz, respectively.

Figure 6.9 shows a three-dimensional plot of BER, SNR, and the angle of arrival.

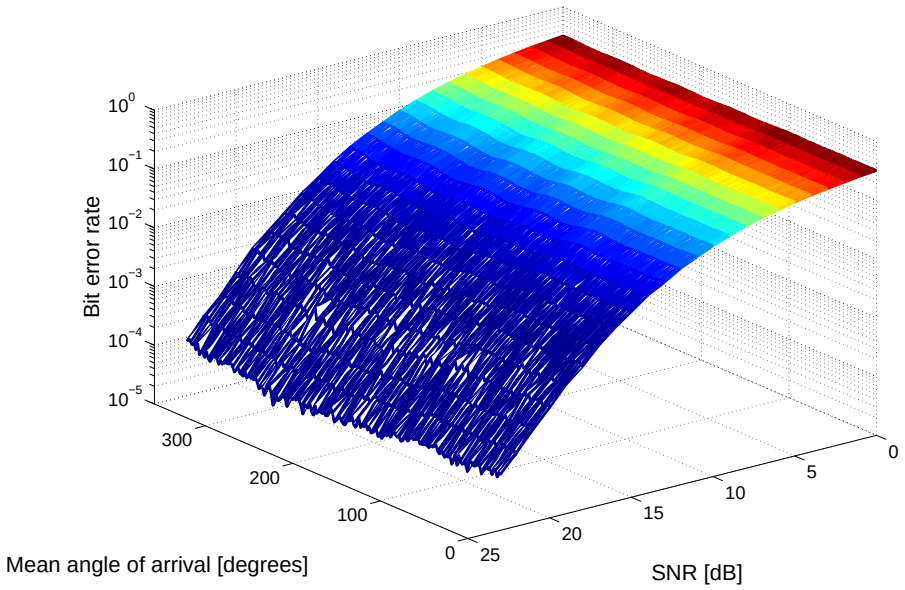

Figure 6.9: Bit error rate of Fe 1-ARA vs. angle of arrival and signal-to-noise ratio.

Here, Alamouti's (2×2) space-time block code encoding and decoding were used with the Fe 1-ARA at the TX and RX [49], and the bit error rate of the Fe 1-ARA was compared with a conventional (2×2) STBC MIMO system, in which two spatially separated antennas were employed. It is evident that as SNR increases, the BER decreases.

Figure 6.10 shows the BER versus the angle of arrival with the SNR as a parameter.

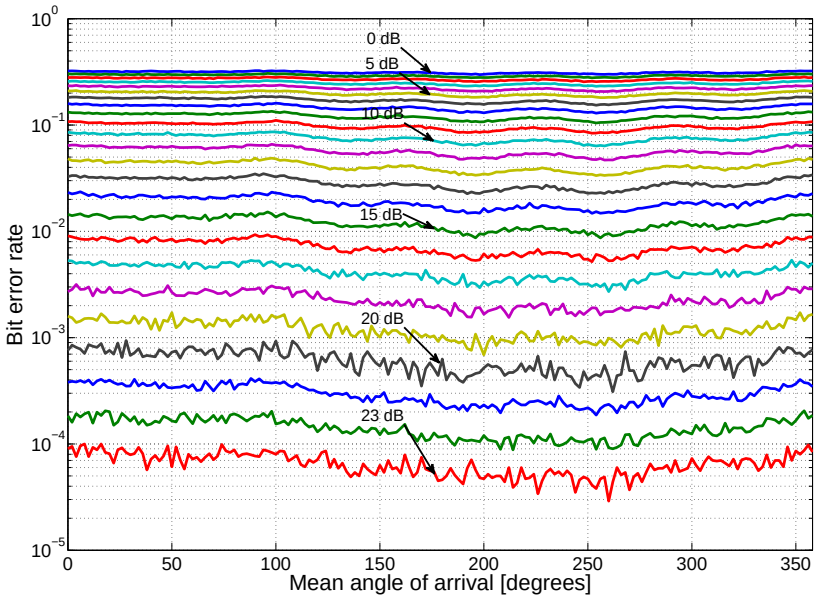

Figure 6.10: Bit error rate of Fe 1-ARA vs. angle of arrival with signal-to-noise ratio as a parameter.

Bit error rate was not calculated by averaging over many channel realizations. Thus, the curves show a coarse nature in Figure 6.10. The radiation efficiency and mutual coupling was taken into consideration in this BER calculations. Standard deviations of the bit error rate over the angle of arrival are $6.63 \cdot 10^{-3}$, $6.30 \cdot 10^{-3}$, and $1.56 \cdot 10^{-5}$ at 0 dB, 10 dB, and 23 dB, respectively. It is observed that the non-symmetric radiation patterns show minor effects on BER of the system when SNR is high, which is opposite to that observed for the capacity case. This was also true for Fe 1-CPA.

Figure 6.11 compares the BER of the Fe 1-ARA averaged over the azimuth angle with that of the conventional (2×2) STBC MIMO system. When only the spatial correlation was taken into account (i.e., $\eta = 100\%$ and $\mathbf{M} = \mathbf{I}$), the Fe 1-ARA shows the same performance

as the the conventional (2×2) STBC MIMO system. When the radiation efficiency and the mutual coupling were considered, the Fe 1-ARA performs inferiorly. For example, to achieve a bit error rate of 10^{-3}, the Fe 1-ARA requires 11.8 dB higher SNR.

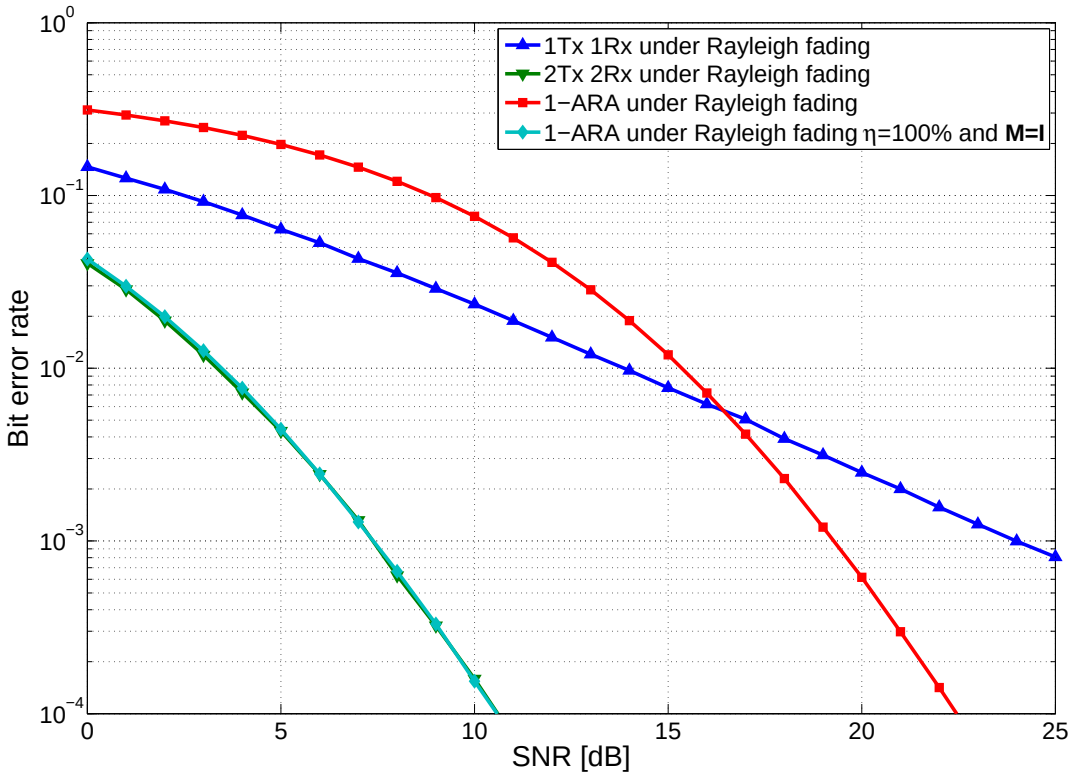

Figure 6.11: Bit error rate comparison of 2×2 MIMO vs. Fe 1-ARA using Alamouti scheme under Rayleigh fading channel.

CHAPTER 7

FABRICATED FE 1-CPA AND FE 1-ARA

An Fe 1-CPA and an Fe 1-ARA were fabricated in the lab using the available $Ba_3Co_2Fe_{24}O_{41}$ hexaferrite material for the substrate. Figures 7.1 and 7.2 show the fabricated Fe 1-CPA and the Fe 1-ARA, respectively.

(a) Top view. (b) Bottom view. (c) Bottom view.

Figure 7.1: Fabricated Fe 1-CPA: top, bottom, and side views.

(a) Top view. (b) Bottom view. (c) Bottom view.

Figure 7.2: Fabricated Fe 1-ARA: top, bottom, and side views.

The radiator and ground plane were created by sputter deposition of gold, copper, and titanium of 30 nm, 1.5 μm, and 60 nm thickness, respectively. Figure 7.3 shows the measured

permeability and permittivity spectra of the fabricated substrate material.

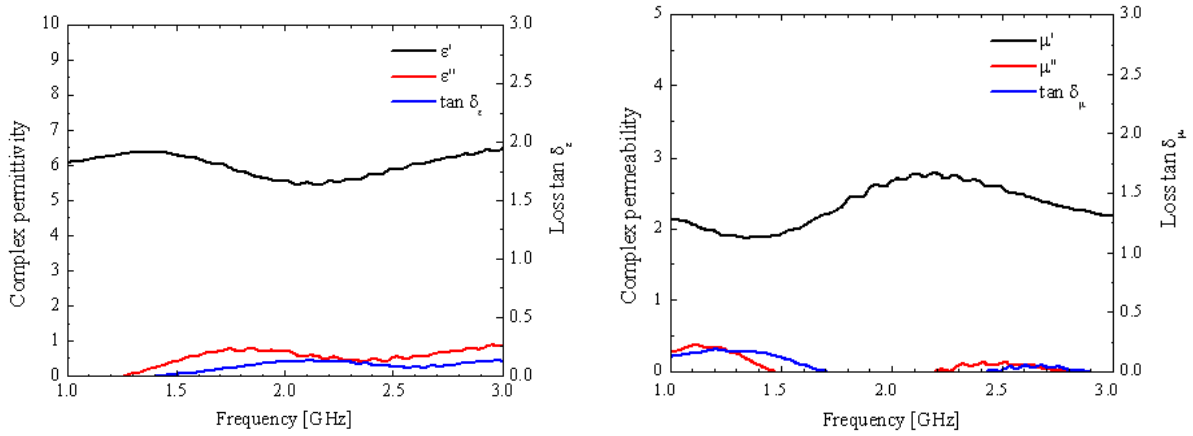

(a) Permittivity (b) Permaebility

Figure 7.3: Measured permittivity and permeability spectra of $Ba_3Co_2Fe_{24}O_{41}$ hexaferrite (10 h shake-milling) + 2 wt% glass sintered at 950° C for 1 h.

Relative permeability $\mu_r = 2.59$ and relative permittivity $\epsilon_r = 5.76$ were measured at 2.45 GHz. The measured magnetic and dielectric loss tangents were $tan\delta_\mu = 0.032$ and $tan\delta_\epsilon = 0.075$, respectively. Note that the simulation results shown in section 5.3 were generated using relative permeability $\mu_r = 2.0$ and permittivity $\epsilon_r = 7.0$. The corresponding loss tangents used for those simulations were $tan\delta_\mu = 0.003$ and $tan\delta_\epsilon = 0.001$. The available ferrite materials in the lab were used for fabrication. This is why the measured relative permittivity, permeability, and tangent losses are different from those of the simulations. Hence, FEKO simulations of the Fe 1-ARA were performed again using the permittivity of 5.0 and permeability of 2.2, which are closer to those of the measured ones. Dimensions of the Fe 1-ARA with two ports have not been optimized yet. A Fe 1-ARA with only one input port was fabricated instead of two.

7.1 Antenna Measurement Methodology

This section briefly describes the measurement methodology of S-parameters and radiation patterns of fabricated antennas. Anritsu MS2026A vector network analyzer (VNA) along with test cables and a 50 Ω load is used to measure S-parameters. Figure 7.4 shows the setup for measuring reflection coefficients of antenna 1 (port 1) and antenna 2 (port 2) S_{11} and S_{22}, respectively. Device under test (DUT) refers to antenna whose S-parameters are to be measured.

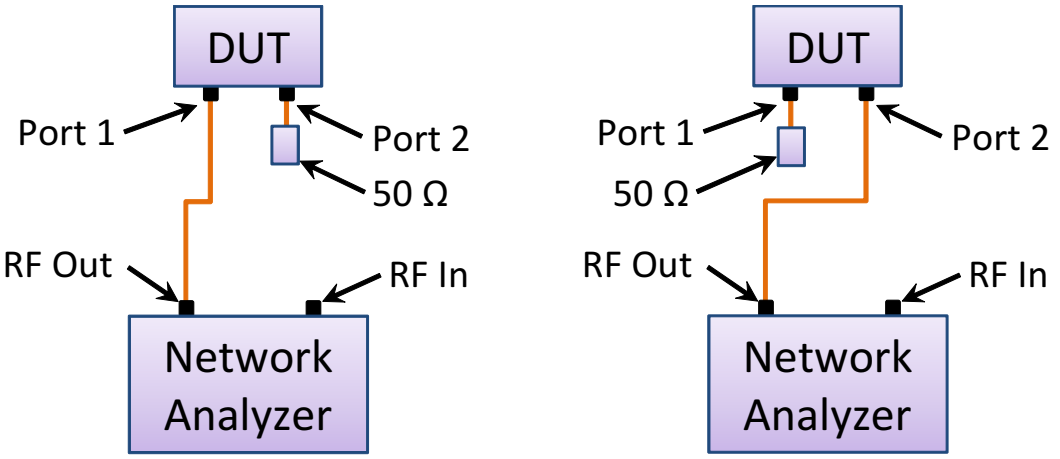

(a) Reflection coefficient of Port 1 (S_{11}). (b) Reflection coefficient of Port 2 (S_{22}).

Figure 7.4: Measuring reflection coefficients of antenna 1 and antenna 2.

To measure the reflection coefficient of antenna 1 (S_{11}), port 1 is connected to the "RF Out" of the VNA via a test cable, and a 50 Ω load resistor is connected to port 2 (antenna 2). Connecting a 50 Ω load resistor to port 2 is required to suppress any signal coupled into port 1 from port 2 (see Figure 7.4a). To measure the reflection coefficient of antenna 2 (S_{22}), port 2 is connected to the "RF Out" of the VNA via a test cable, and a 50 Ω load resistor is connected to port 1 (antenna 1) (see Figure 7.4b).

Transmission coefficients are measured according to the setup shown in Figure 7.5.

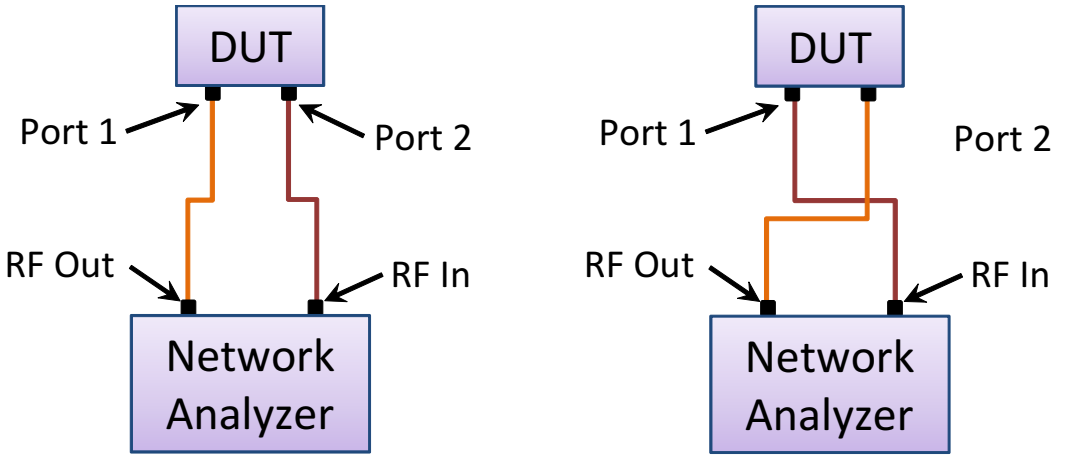

(a) Transmission coefficient from Port 1 to Port 2 (S_{21}).

(b) Transmission coefficient from Port 2 to Port 1 (S_{12}).

Figure 7.5: Measuring transmission coefficients from antenna 1 to antenna 2 and vice versa.

To measure the signal coupled from port 1 (antenna 1) to port 2 (antenna 2) (S_{21}) port 1 is connected to "RF Out," and port 2 is connected to "RF In" of VNA (see Figure 7.5a). To measure S_{12}, the signal coupled from port 2 to port 1, port 2 is connected to "RF Out," and port 2 is connected to "RF In" of VNA (see Figure 7.5b).

Radiation patterns of fabricated antennas were measured in an anechoic chamber. The measurement set up consists of following equipments:

- Aeroflex 3020A PXI RF signal generator
- MICOS DT-80 rotation stage
- Agilent E4416A EPM-P power meter
- Agilent E9323A power sensor
- Horn antenna

- Anechoic chamber

Figure 7.6 shows the block diagram of the setup used to measure radiation patterns of fabricated antennae.

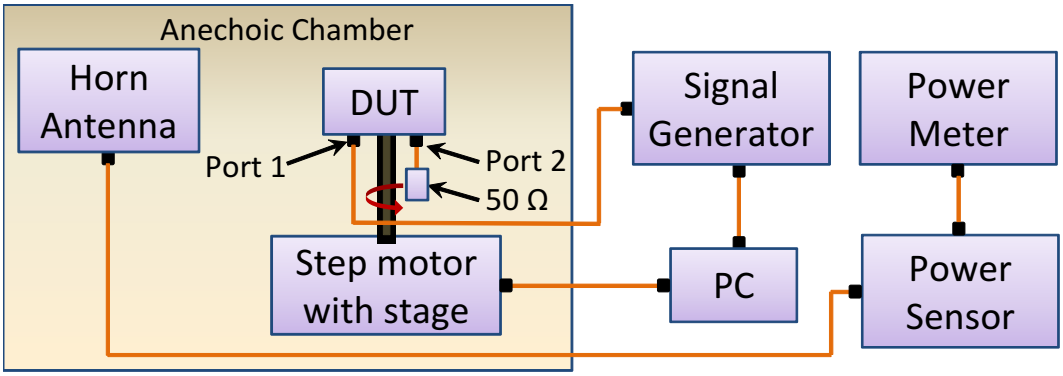

Figure 7.6: Block diagram of measurement setup of antenna radiation patterns.

The antenna, whose radiation patterns are to be measured (DUT), is mounted on the MICOS rotation stage. The antenna is then connected to the signal generator via test cable. The rotation stage with the antenna mounted on it is placed at one end of the anechoic chamber. The horn antenna, which is placed at the other end of the anechoic chamber, is used to receive signals. To measure the received signal power, the horn antenna is connected to the power sensor, which is then attached to the power meter. To obtain the radiation pattern of the fabricated antenna, a continuous wave (CW) signal of desired frequency is generated using the signal generator. This signal is then transmitted by the fabricated antenna. The received signal strength of the horn antenna will be displayed on the power meter. This value is recorded, the antenna is rotated in the azimuth direction by a desired resolution (e.g., 2°) and the received signal power recorded. This process is repeated until the antenna is rotated a full circle (360°), in the azimuth direction. The software provided by Aeroflex

and MICOS are used to generate the CW signal and rotate the stage, respectively. Both software are installed on a PC. Figure 7.6 shows how to obtain radiation pattern associated with antenna 1 (port 1). Port 1 is connected to the output of the signal generator, and a 50 Ω load is connected to port 2 to avoid and reflections. To obtain the radiation pattern of antenna 2, the output of the signal generator and 50 Ω load are to be connected to port 1 and port 2, respectively.

7.2 Fe 1-CPA

Figure 7.7 shows the simulated and measured S-parameters of the fabricated Fe 1-CPA.

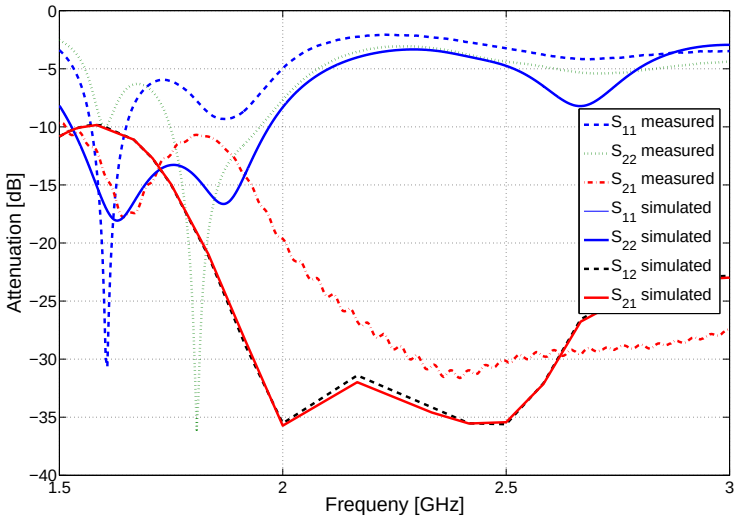

Figure 7.7: Simulated and measured S-parameters of Fe 1-CPA.

The measured permittivity, permeability, and loss tangent values of the substrate materials were used for these FEKO simulations. The deep notches on the measured $|S_{11}|$ and $|S_{22}|$ of the Fe 1-CPA appear at 1.6 GHz and 1.8 GHz, respectively, but these are not so evident in the simulated values. At 2.67 GHz, another unexpected mode is excited according to

the simulated reflection coefficients of Fe 1-CPA. The measured values also show a similar behavior, even though it is not as evident. The measured values of $|S_{12}|$ and $|S_{21}|$ are well below -25 dB above 2.1 GHz and shifted to higher frequencies than the simulated values. Overall, the trends of the simulation results are in agreement with those of the measured values of the fabricated Fe 1-CPA.

7.3 Fe 1-ARA

Figure 7.8 shows the measured and simulated reflection coefficients of the fabricated Fe 1-ARA.

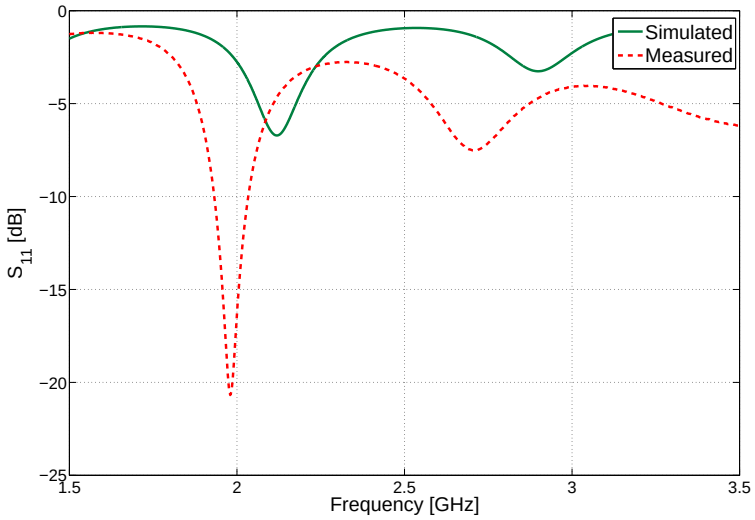

Figure 7.8: Simulated and measured S-parameters of Fe 1-ARA.

Two resonant frequencies at 1.9 GHz and 2.7 GHz can be observed. Figure 7.9 shows the corresponding radiation patterns over the azimuth angle at 1.9 GHz and 2.7 GHz.

The measured power over the azimuth angle is shown in decibels. The amplitude of the received power was scaled, and is shown in Figure 7.9 for better comparison. It is evident that

the measured radiation pattern of the Fe 1-ARA at 1.9 GHz agrees well with the simulation. But the measured values at 2.7 GHz differ slightly from the simulated values. This is due to the sensitivity of the power sensor. At 1.9 GHz, the reflection coefficient $|S_{11}|$ is -20 dB, whereas at 2.7 GHz, it is only -7.5 dB. The higher the reflection coefficient, the more power reflected at the input port, thus resulting in less power radiated. Therefore, at 2.7 GHz, less power is radiated by the antenna. This drives the power sensor connected to the receiving horn antenna close to its sensitivity limit, hence causing less accurate measurements. It is evident from Figure 7.9 that the mode $n = 2$ and $n = 3$ are excited at 1.9 GHz and 2.7 GHz, respectively.

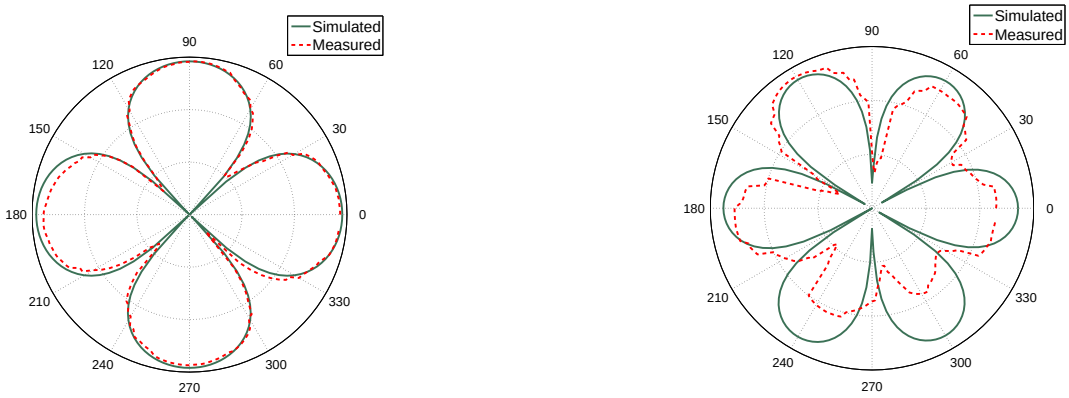

(a) (b)

Figure 7.9: Measured and simulated gains of fabricated Fe 1-ARA over azimuth plane (a) at $f = 1.9$ GHz and at (b) $f = 2.7$ GHz.

Table 7.1 compares the physical dimensions and material parameters of the proposed Fe 1-CPA and Fe 1-ARA with those of the dielectric 2-CPA in the work of Forenza and Heath [7].

Table 7.1: PARAMETERS OF DIELECTRIC 2-CPA, FERRITE 1-CPA, and FERRITE 1-ARA.

	Dielectric 2-CPA	Ferrite 1-CPA	Ferrite 1-ARA
$h^{(1)}(mm)$	9.0	7.0	6.5
$\rho_0^{(1)}(mm)$	52.8	25.5	30.0
$\rho_{gp}^{(1)}(mm)$	105.6	25.5	30.0
$\rho_f^{(1)}(mm)$	47.5	12.7	26.0
$\epsilon_r^{(1)}$	2.2	7.0	5.0
$\mu_r^{(1)}$	1.0	2.0	2.2
$h^{(2)}(mm)$	7.0	N/A	N/A
$\rho_0^{(2)}(mm)$	27.0	N/A	N/A
$\rho_{gp}^{(2)}(mm)$	48.6	N/A	N/A
$\rho_f^{(2)}(mm)$	21.6	N/A	N/A
$\epsilon_r^{(2)}$	8.0	N/A	N/A
$\mu_r^{(2)}$	1.0	N/A	N/A
volume (cm^3)	367.4 (100%)	14.3 (3.89%)	18.3 (4.98%)
weight (g)	808.3 (100%)	76.5 (9.46%)	97.9 (12.11%)
Bandwidth (MHz)	75	25	70

Superscript (1) and(2) correspond to the bottom patch and the top patch of 2-CPA respectively. Z-type hexagonal ferrite: 5.35 [g/cm^3], Duroid : 2.2 [g/cm^3] are used for the weight calculations.

CHAPTER 8

PARAMETER OPTIMIZATION OF FE 1-CPA

FEKO electromagnetic simulator offers three different algorithms to optimize design parameters: simplex (Nelder-Mead method), particle swarm optimization (PSO), and genetic algorithm (GA). In the simplex method, the final optimum depends on the starting point. A geometric figure is formed by a set of $N + 1$ points, in an N-dimensional space. Then, at each of these $N + 1$ points the values of the combined optimization goals are compared and moved toward an optimum point in an iterative process.

The particle swarm optimization method is based on the movement and intelligence of swarms found in nature. This algorithm was first introduced by Kennedy and Eberhart [60] as a concept for the optimization of nonlinear functions. This is a global search algorithm that uses a population-based stochastic evolutionary computation method. This algorithm can be described using the following analogy: Consider a swarm of bees whose goal is to find a location with the maximum density of flowers. Each bee represents a set of parameter values such as information about the location of flower abundance. This information can be based on its own experience as well as the experience of all the other bees. Based on the weights given to individuality or peer pressure, a bee flies in a direction, between the positions of the local and the global bests. Once the flying is done, the bee conveys the new-found information to all the other bees, which then adjust their positions and velocities. With this constant exploring and exchange of information, all the bees are eventually drawn towards the position of highest concentration of flowers.

Utilizing the optimization algorithms available in FEKO, the geometry of Fe 1-CPA (see Figure 5.2) is optimized for bandwidth and gain. The parameters that were used in the optimization process are as follows: distance of the feed pin ρ_f, radius of the small disc f, gap between the small disc and the rest of the conducting surface g, and height of the antenna h. Table 8.1 shows the minimum, maximum, and start values of the parameters to be optimized.

8.1 Optimization of all Parameters Simultaneously using PSO Algorithm

All parameters listed in Table 8.1 are varied in this approach.

Table 8.1: RANGE OF PARAMETER VALUES USED IN OPTIMIZATION.

	Minimum (mm)	Maximum (mm)	Start (mm)
h	2	10	5
ρ_f	8	18	9
f	0.4	5	1
g	0.1	2	0.2

The objective of this optimization is to maximize the antenna gain. Figure 8.1 shows the change of each parameter value for approximately 650 optimization steps of PSO algorithm. As it can be seen, none of the parameters converged in this process.

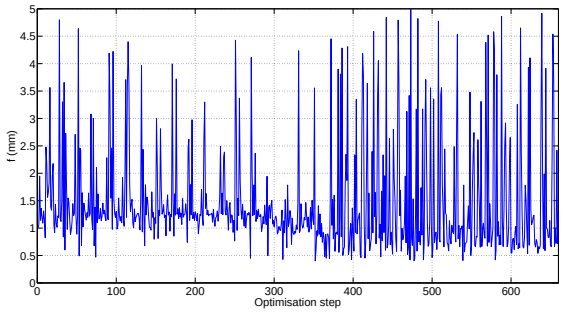

(a)

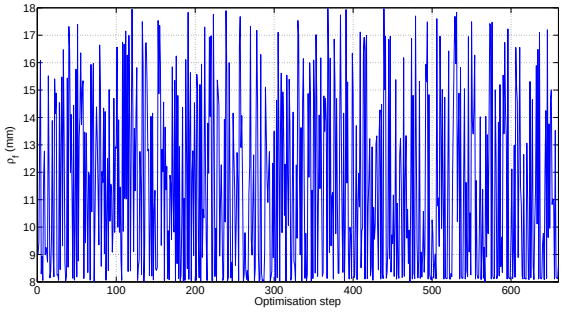

(b)

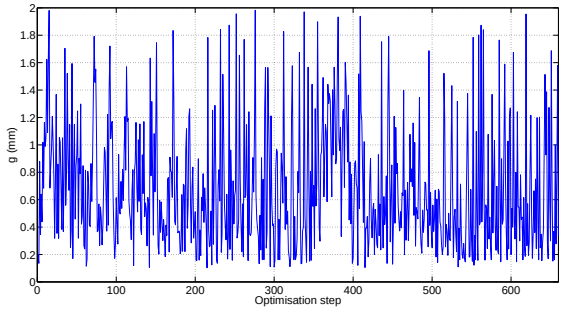

(c)

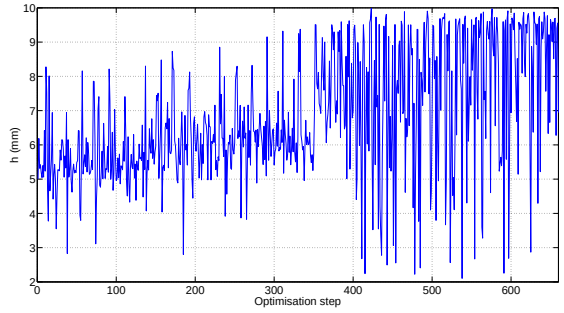

(d)

Figure 8.1: Particle swarm optimization of parameters f, ρ_f, g, and h of Fe 1-CPA. All the parameters were varied simultaneously.

Figure 8.2 shows the variation of antenna efficiency and the maximum antenna gain with the iterations.

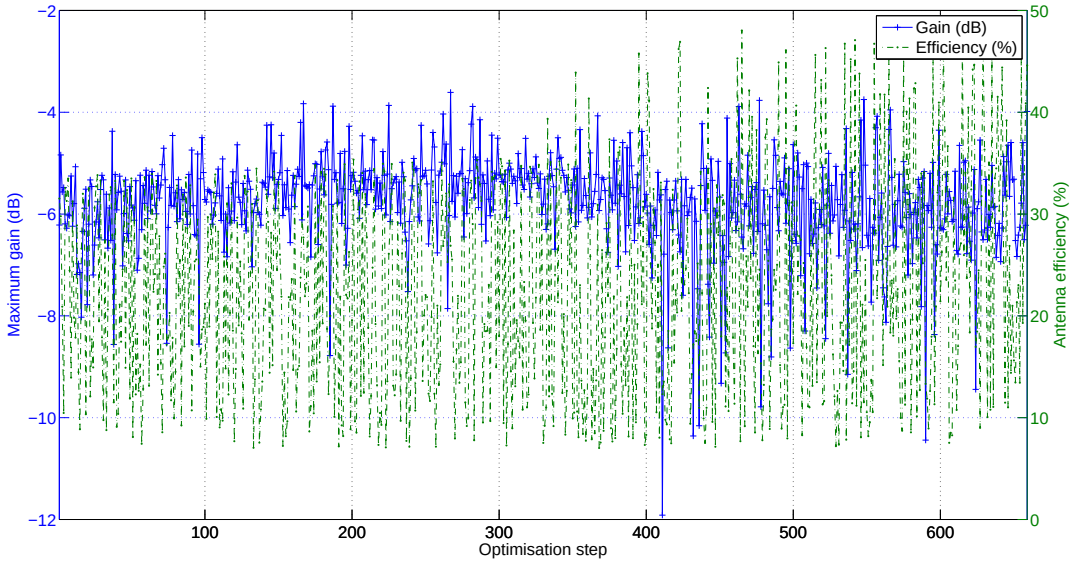

Figure 8.2: Gain and antenna efficiency variations in particle swarm optimization.

Gain varies from as low as -11.9 dB to as high as -3.6 dB, whereas the efficiency varies from as low as 7% to as high as 40%. Since none of the parameters converged as a second approach, only a single parameter is optimized instead of optimizing all four parameters simultaneously.

8.2 Optimization of a Single Parameter using PSO Algorithm

Since none of the parameters converged when the optimization was carried over all the parameters simultaneously, optimization of a single parameter at a time is considered. The sequence of optimization is as follows: the height of substrate h, the position of feed pin ρ_f, the radius of small disc f, and the gap between the small disc and the rest of the conducting surface g. It is evident from Figure 8.3 that the height of the substrate converges

to approximately 8.2 mm.

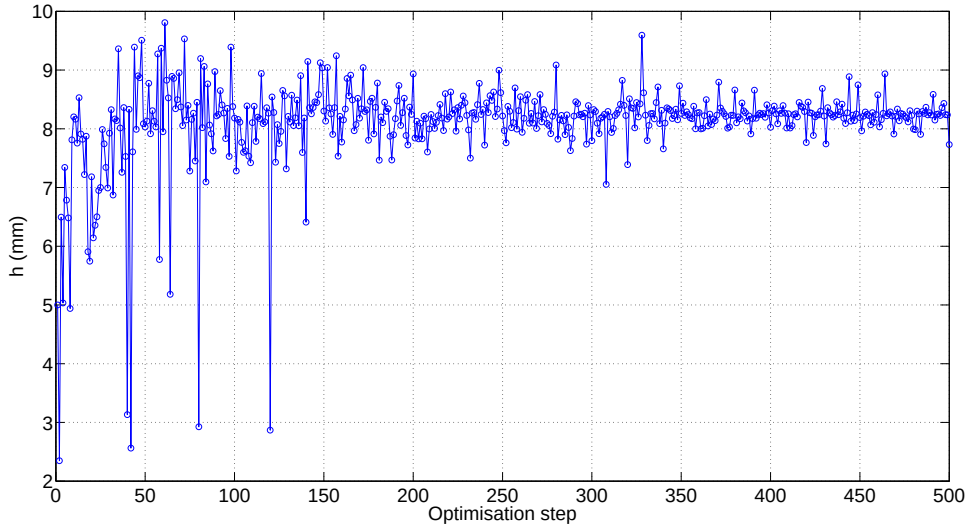

Figure 8.3: Particle swarm optimization of parameter h.

Variations in efficiency and maximum gain are shown in Figure 8.4. The maximum gain varies around -6.1 dB, and the efficiency varies from 9% to 24%. The average efficiency is 11.8%. It is evident that the maximum gain and the efficiency are highly correlated.

As the next step, h is set to 8.2 mm, and the parameter ρ_f is optimized. Figure 8.5 shows how ρ_f varies in the iteration process. It is evident that ρ_f does not converge, but varies between 8mm and 18mm. To see whether there is any correlation between maximum gain (or efficiency) and ρ_f, values of ρ_f are sorted according to a range of gain (or efficiency) values. In Figure 8.6 and Figure 8.7 ρ_f are sorted according to gain values from -6 dB to -4.8 dB in 0.4 dB increments and efficiency values from 10% to 30% in 5% increments, respectively.

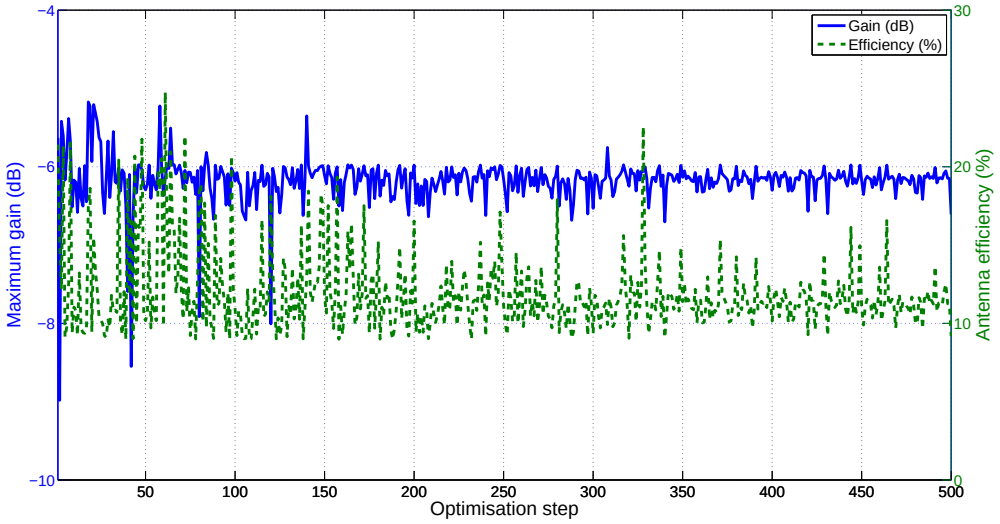

Figure 8.4: Gain and antenna efficiency variations in particle swarm optimization of parameter h.

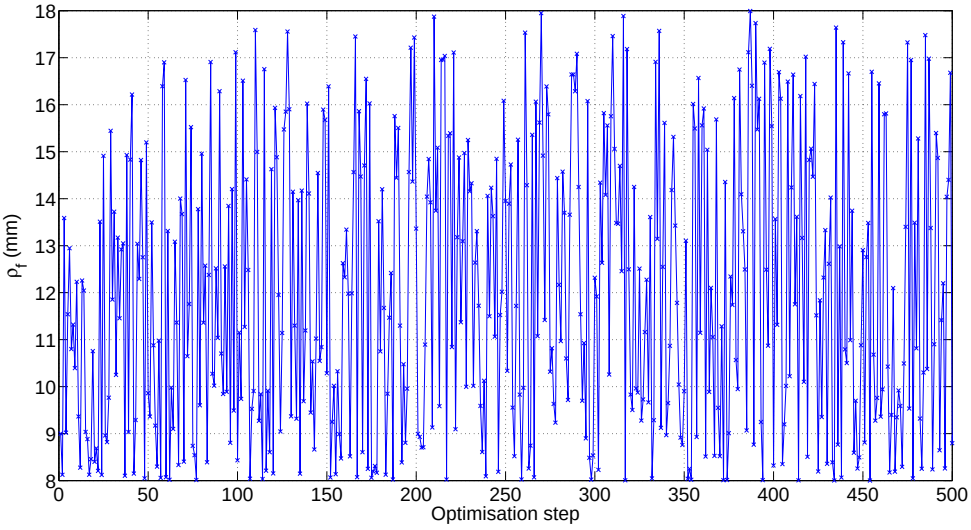

Figure 8.5: Particle swarm optimization of parameter ρ_f.

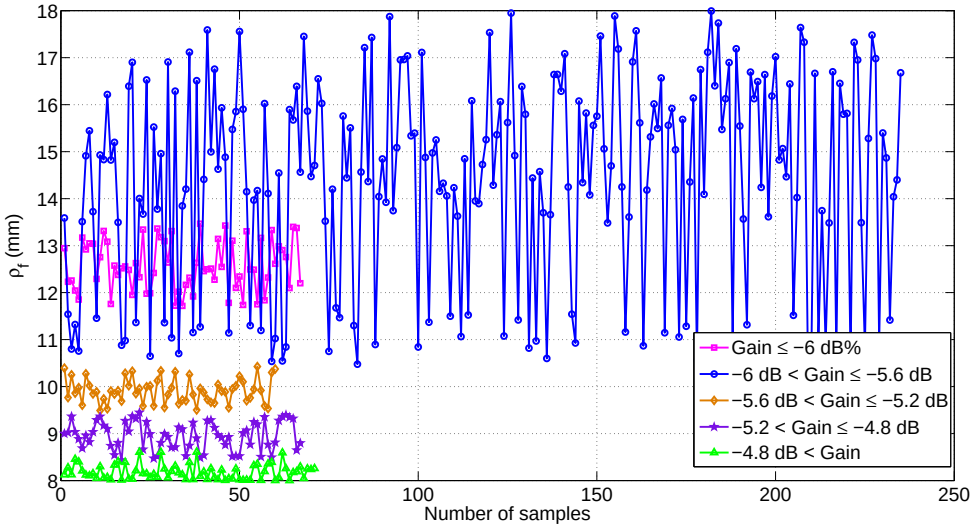

Figure 8.6: Dependency of ρ_f on maximum gain in PSO.

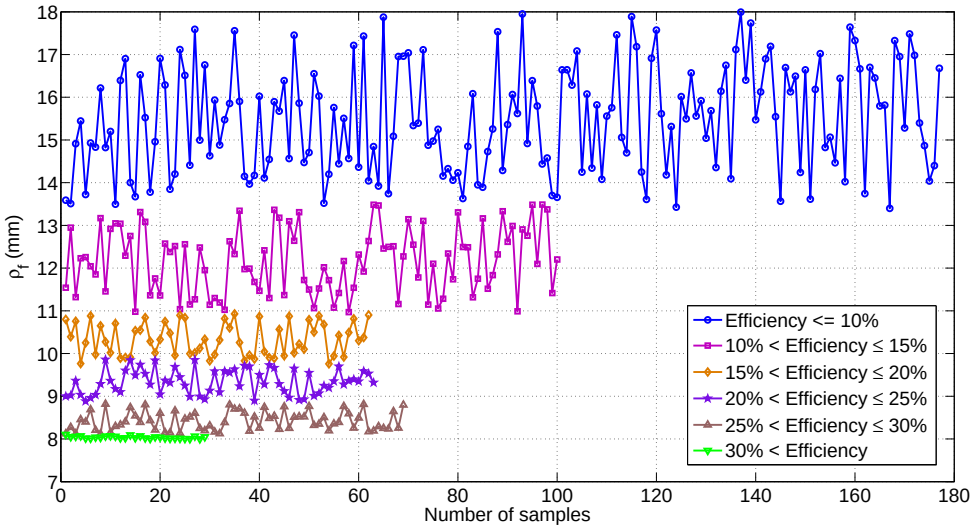

Figure 8.7: Dependency of ρ_f on efficiency in PSO.

It is evident that there are disjoint sets of ρ_f values except for the range of gain values -6 dB to -5.6 dB (see Figure 8.6). These sets are disjoint for all the range of efficiency values as it can be seen in Figure 8.7. Figure 8.8 shows the correlation between maximum gain and antenna efficiency.

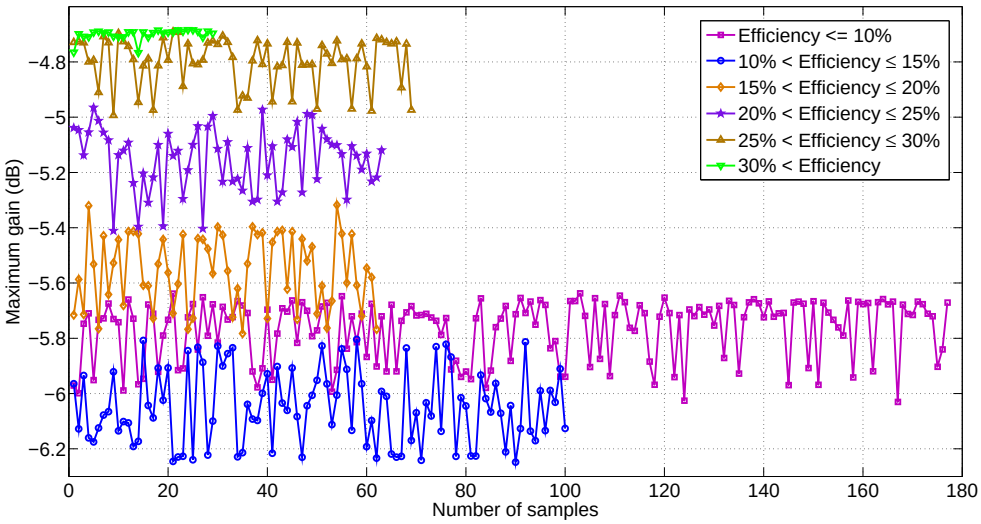

Figure 8.8: Dependency of maximum gain on efficiency in PSO of ρ_f.

It is evident that gain values vary in non-overlapping range of values except for lower efficiency values (10% to 20%). The higher the antenna efficiency the higher the maximum antenna gain. With this knowledge and by observing the azimuth radiation pattern, ρ_f is selected to be 16.9 mm for the next step.

In the third step, h and ρ_f are set to 8.2 mm and 16.9 mm, respectively, and f is optimized. Again, here the parameter does not converge, but varies between 0.41 mm and 5.0 mm (see Figure 8.9). A similar approach as in second step is taken to choose an appropriate vale for f. Figures 8.10 and 8.11 show the grouping of f values according to maximum gain and efficiency of the antenna, respectively.

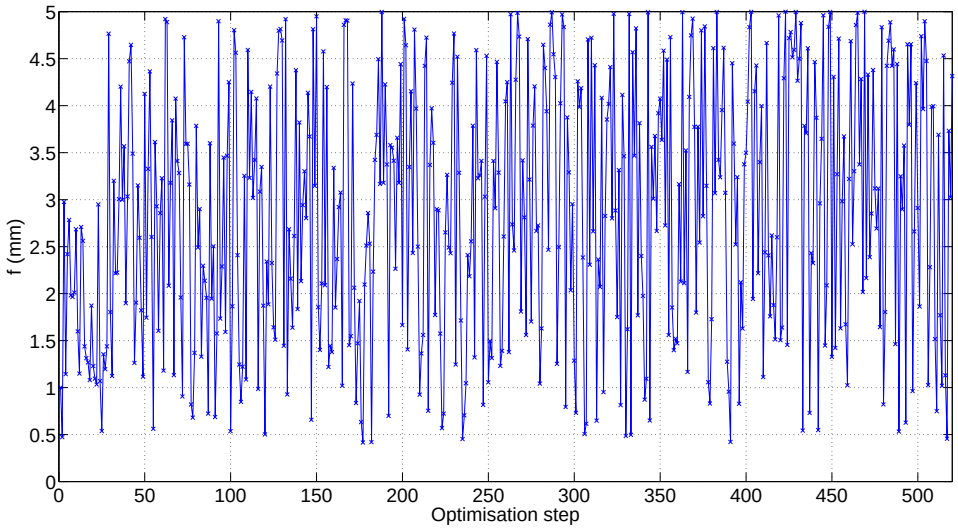

Figure 8.9: Particle swarm optimization of parameter f.

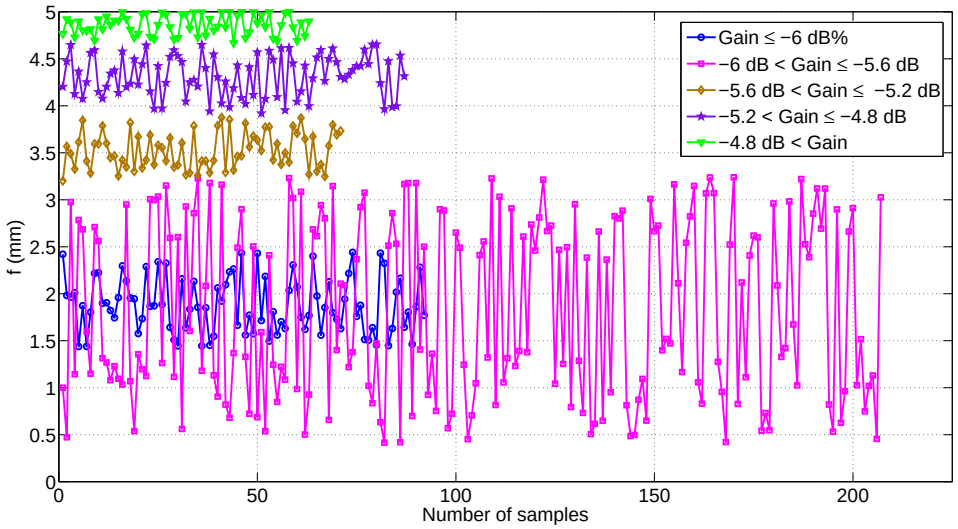

Figure 8.10: Dependency of f on maximum gain in PSO.

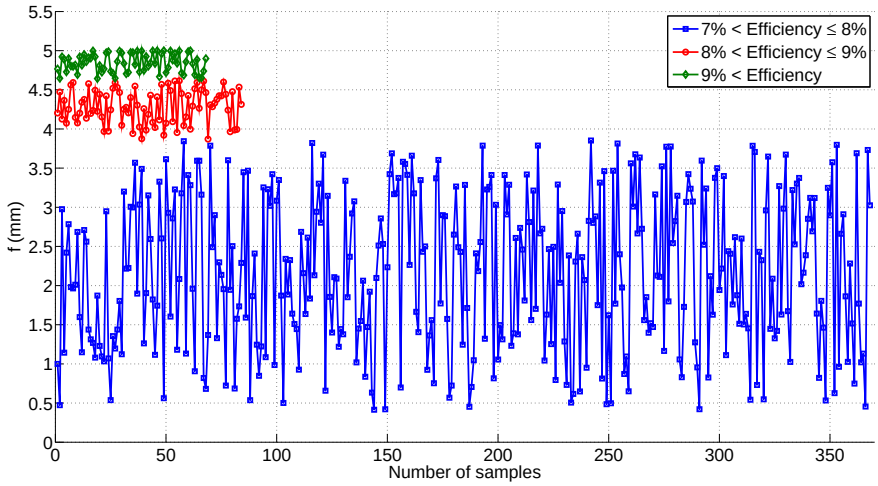

Figure 8.11: Dependency of f on efficiency in PSO.

Also, for this case the correlation between the antenna efficiency and the maximum gain is evident (see Figure 8.12.) The higher the efficiency the higher the maximum gain.

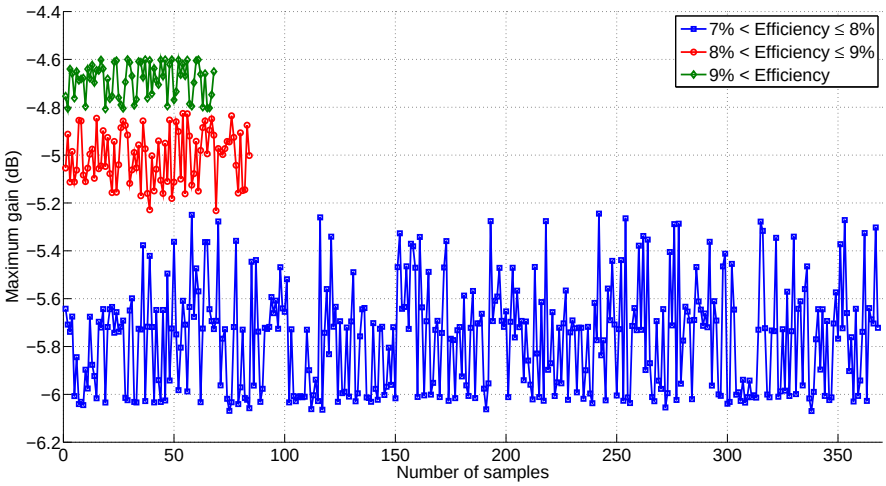

Figure 8.12: Dependency of maximum gain on efficiency in PSO of f.

Using the symmetry of the radiation pattern (equal strength of each lobe) as a criteria, f is selected to be 4.5 mm, and the value of g is varied in the fourth step of the optimization. Figure 8.13 shows the variations of g in the iteration process.

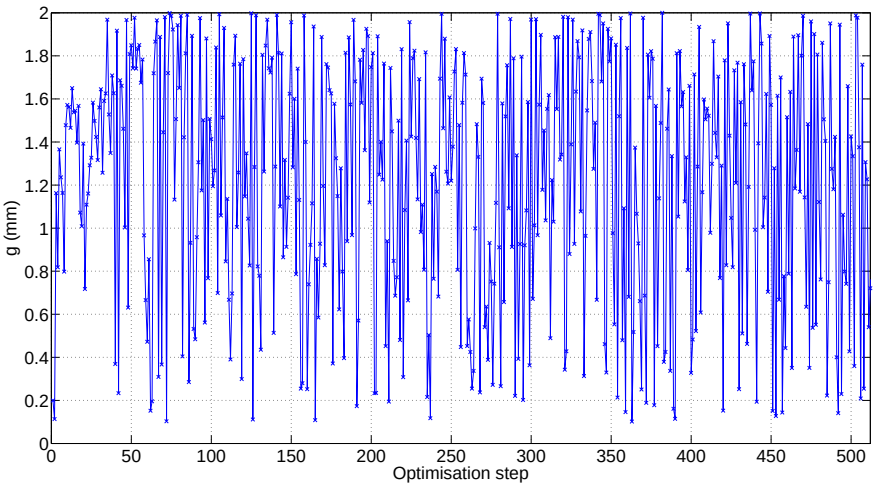

Figure 8.13: Particle swarm optimization of parameter g.

It is also evident that also here the parameter does not converge. Figures 8.14 and 8.15 shows the grouping of g values according to maximum gain and efficiency of the antenna, respectively.

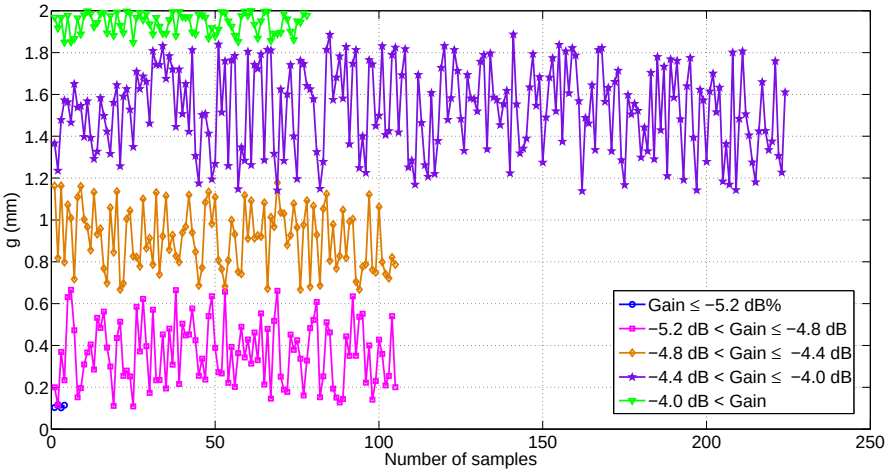

Figure 8.14: Dependency of g on maximum gain in PSO.

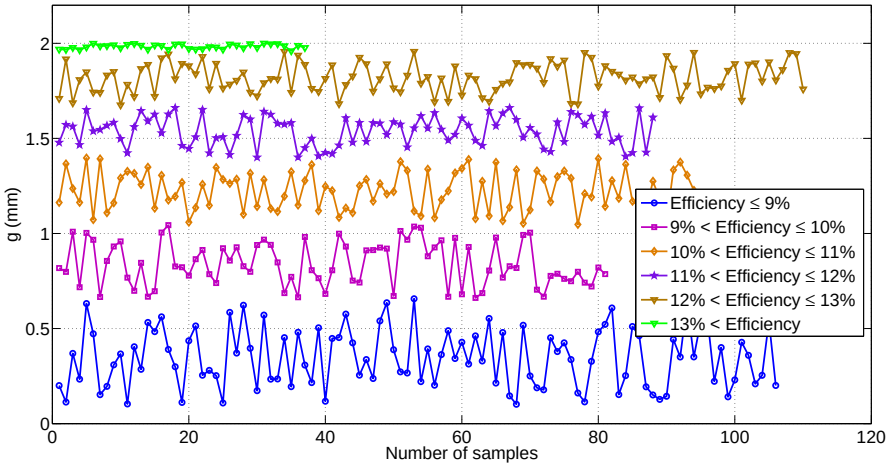

Figure 8.15: Dependency of g on efficiency in PSO.

Also, for this case the correlation between the antenna efficiency and the maximum gain is evident (see Figure 8.16.) The higher the efficiency the higher the maximum gain. From these simulation results g is selected to be 0.9 mm. Using the final values (see Table 8.2) S-parameters and radiation patterns were simulated. Simulated S-parameters are shown in Figure 8.17.

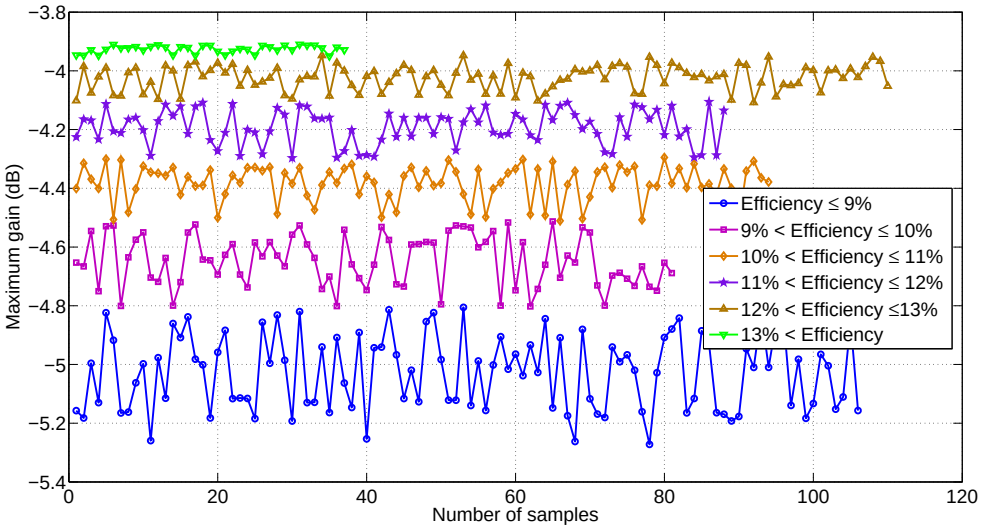

Figure 8.16: Dependency of maximum gain on efficiency in PSO of g.

Table 8.2: PARAMETERS USED IN SINGLE PARAMETER OPTIMIZATION USING PSO.

	Step 1	Step 2	Step 3	Step 4	Final
h	varied	8.2 mm	8.2 mm	8.2 mm	8.2 mm
ρ_f	12.75 mm	varied	16.9 mm	16.9 mm	16.9 mm
f	0.85 mm	0.85 mm	varied	4.5 mm	4.5 mm
g	0.5 mm	0.5 mm	0.5 mm	varied	0.9 mm

The bandwidth has reduced to 11 MHz and the center frequency has shifted to about 2.477 GHz.

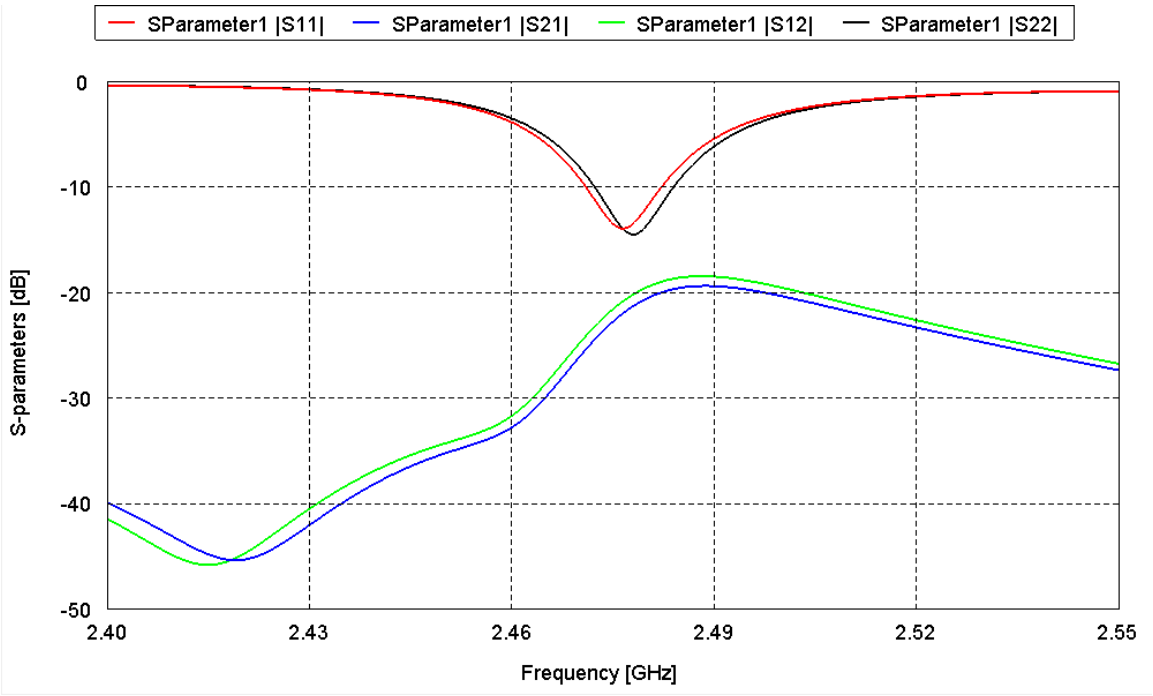

Figure 8.17: S-parameters of Fe 1-CPA using iteratively optimized parameters.

CHAPTER 9

HIGH-EFFICIENCY MEANDER ANTENNA (HEMA)

This chaper proposes a half-cycle microstrip high-efficiency meander antenna, which can be used to realize a 2×2 MIMO system and analyze its microwave theoretic as well as communication theoretic performance metrics, such as S-parameters, antenna efficiency, radiation patterns, BER, and ergodic capacity. The correlation between the antenna radiation patterns are considered, and mutual coupling and radiation efficiency are accounted for in the channel matrix, which was used in BER and capacity calculations. The effect of radiation efficiency on those metrics is presented and compared. The author believes that this paper is the first one to include all of these practical parameters together in the evaluation of an antenna.

9.1 HEMA Antenna Design

The objective is to design an antenna that can be used for 2×2 MIMO applications and with dimensions that fit in a current smart phone. The antenna is modeled in the FEKO electromagnetic simulator to replicate antenna characteristics. The design goals are more than 200 MHz of impedance bandwidth centered at 2.45 GHz, high isolation between antennas ($<$ -20 dB), and high efficiency. Impedance bandwidth is evaluated at a voltage standing wave ratio $< 2:1$, which is -10 dB ($|S_{11}|$ and $|S_{22}|$), a more strict condition than that of other antennas previously listed in Table 2.1.

The signal received at each antenna must be independent to obtain the benefits of MIMO communication systems. To achieve this, the antennas should be designed so that mutual

coupling between antennas becomes minimal. Mutual coupling, which is undesired in MIMO applications, is a function of the spatial separation between antenna elements. Furthermore, high isolation is required between the ports to achieve higher radiation efficiency.

The model of the antenna used in the FEKO electromagnetic simulator is shown in Figure 9.1.

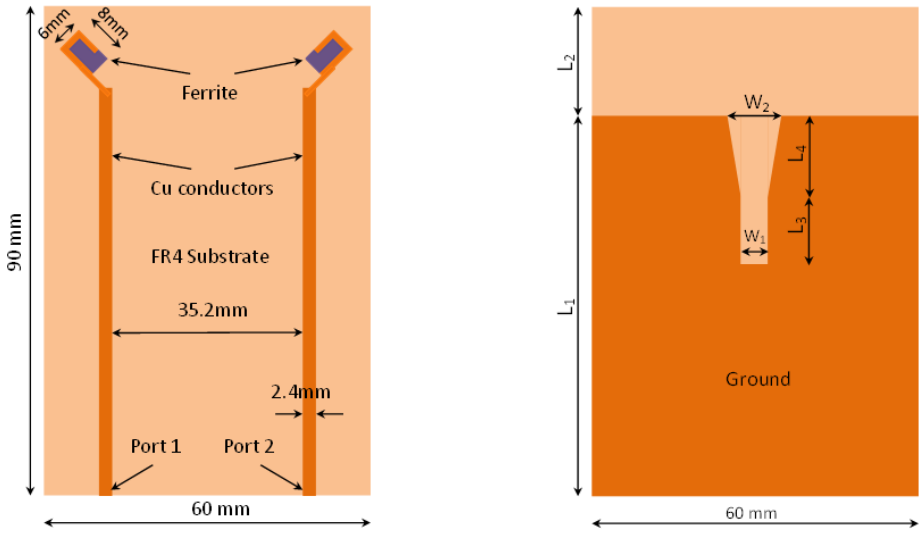

(a) Top view.

(b) Bottom view.

Figure 9.1: Geometry and dimensions of antenna model.

The antenna model consists of two spatially separated half-cycle microstrip meander structures. Each of these meander structures is placed on a $8 \times 6 \times 1.5$ mm^3 piece of ferrite material. Dimensions of the system board and the antenna configuration are shown in Figure 9.1a. Microsrip structures and ferrite material are shown in orange and purple, respectively. Figure 9.1b shows the bottom view of the antenna. In the proceeding section the values of L_1, W_1, and W_2 are varied to obtain targeted results. The values of L_3 and L_4 are 10 mm and 15 mm, respectively, and are kept constant. The dimensions of the system board (90×60

mm^2) are not changed (L_1+L_2 = 90 mm).

9.1.1 Ground Plane and Y-Shaped Slit

Initially, S-parameters are simulated simply by varying the length of the ground plane, L_1 (see Figure 9.1b). In this case, the ground plane does not include the Y-shaped slit. The length of the ground plane, L_1, is varied from 90 mm to 60 mm in 5 mm steps. When L_1 = 90 mm, the backside of the FR4 substrate is entirely covered by the ground plane. Resulting S-parameters are shown in Figure 9.2.

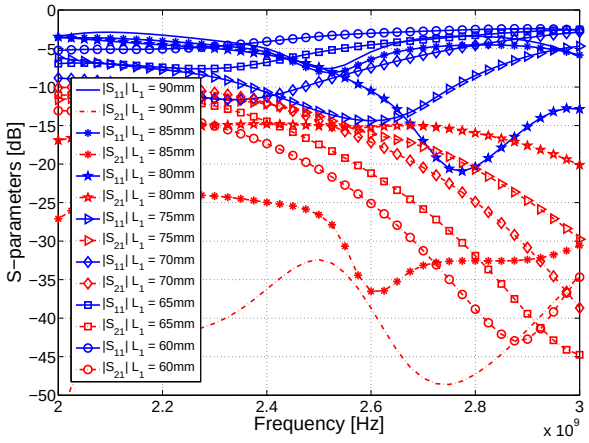

(a) Simulated $|S_{11}|$ and $|S_{21}|$.

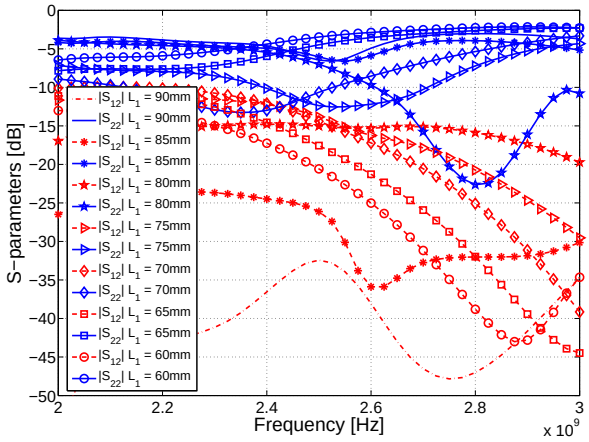

(b) Simulated $|S_{22}|$ and $|S_{12}|$.

Figure 9.2: Simulated S-parameters of HEMA for variable ground plane lengths, L_1.

For the sake of clarity, S-parameters related to Port 1 and Port 2 are separated and shown in Figures 9.2a and 9.2b, respectively.

As can be seen, $|S_{21}|$ and $|S_{12}|$ are almost identical. Even though S_{11} and S_{22} vary slightly (if compared at each frequency), the tendencies that they exhibit for variable ground plane length is identical. Therefore, in the following discussion, only $|S_{11}|$ and $|S_{21}|$ are considered. One of the design goals is to achieve reflection coefficients ($|S_{11}|$ and $|S_{22}|$) lower than -10 dB centered around 2.45 GHz (f_c), the region that is considered the impedance bandwidth of the antenna. Additionally, signal coupling from one port to the other, which is given by $|S_{21}|$ and $|S_{12}|$, is desired to be lower than -20 dB to achieve lower signal correlation between antennas.

When $L_1 = 80$ mm, an impedance bandwidth of 400 MHz centered around 2.8 GHz can be achieved, which is unfortunately not at the desired center frequency. It is evident that this center frequency corresponding to the lowest $|S_{11}|$ value shifts towards lower frequencies when L_1 is decreased. When L_1 is smaller than 70 mm, the reflection coefficients become undesirably high (> -10 dB). Furthermore, when the -10 dB impedance bandwidth is considered, the signal coupled from Port 2 to 1 ($|S_{21}|$) is greater than -15 dB for all values of L_1. The impedance bandwidths that can be achieved for $L_1 = 75$ mm and 70 mm are 375 MHz and 300 MHz, respectively. Since for $L_1 = 70$ mm, $|S_{11}|$ is centered closer to f_c than that for $L_1 = 75$ mm, $L_1 = 70$ is used in the subsequent design process.

By varying the ground plane length, it is possible to adjust reflection coefficients to the desired center frequency and achieve adequate impedance bandwidth, as shown earlier (see Figure 9.2). But further improvements are necessary to lower the undesired higher signal coupling (> -15 dB). The basic idea behind reducing the signal coupling between ports is

to reduce the current flow between them by introducing a slit in the ground plane. First, a rectangular slit ($W_1 = W_2$) is introduced (see Figure 9.1b). S-parameters are simulated by varying the width of the slit W_1 from 1 mm to 6 mm, and these results are shown in Figure 9.3.

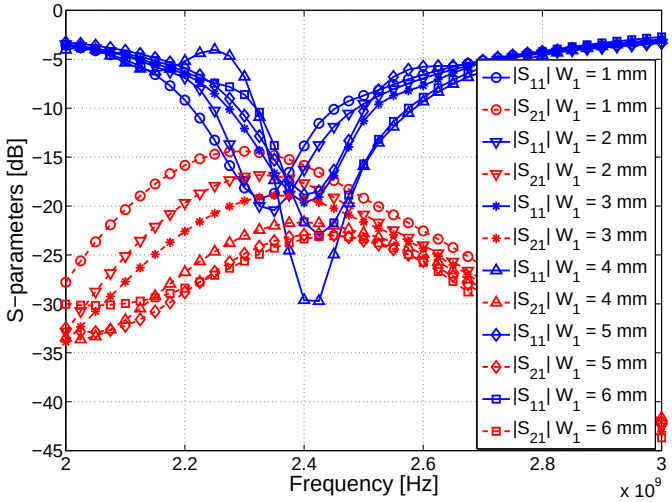

(a) Simulated $|S_{11}|$ and $|S_{21}|$.

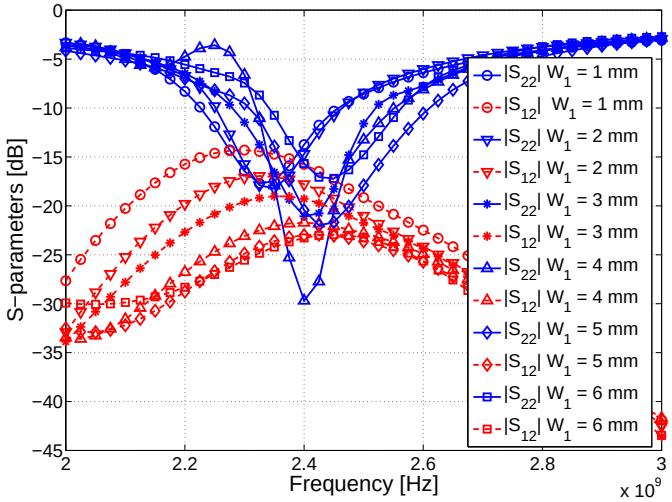

(b) Simulated $|S_{22}|$ and $|S_{12}|$.

Figure 9.3: Simulated S-parameters of HEMA for variable slit widths W_1. Ground plane length $L_1 = 70$ mm.

The length of the slit is 25 mm, which is kept constant. It is evident that the frequency where the minimum $|S_{11}|$ occurs shifts to higher frequencies with the increase of slit width. The impedance bandwidth varies slightly for different slit widths. The minimum and maximum values, 210 MHz and 267 MHz, are achieved when $W_1 = 5$ mm and $W_1 = 4$ mm, respectively. The effect of slit width on $|S_{12}|$ and $|S_{21}|$ is very evident. The maximum value of $|S_{21}|$ decreases from -14 dB to -23 dB with the increase in slit width. As expected, the wider the slit width, the lower the signal coupling between the ports.

By considering the impedance bandwidth and signal coupling, a slit width of 4 mm and a ground plane length of 70 mm seem to be a good choice for the antenna design. Even though the previously mentioned impedance bandwidth is about 267 MHz for this case, when both $|S_{11}|$ and $|S_{22}|$ are considered, this is reduced to 230 MHz since they are not perfectly aligned (compare Figures 9.3a and 9.3b). The antenna achieves lower signal coupling over the entire frequency range, which is less than -21.6 dB. When the lowest values of $|S_{11}|$ and $|S_{22}|$ are considered, they are not yet centered at f_c.

Further improvement in the antenna design is investigated by changing the shape of the slit in the ground plane. As a simple modification to the rectangular slit, a Y-shaped slit is introduced (see Figure 9.1b). Figure 9.4 shows the simulated S-parameters of the antenna for variable W_2 values. W_2 is varied from 5 mm to 10 mm in 1 mm increments W_1 is kept at 4 mm. The lowest values of $|S_{11}|$ and $|S_{22}|$ shift to higher frequencies with increasing W_2 values. Furthermore, $|S_{21}|$ and $|S_{12}|$ values for all W_2 values are lower than -18.8 dB over the entire simulation frequency range. This number is -14.3 dB for the rectangular slit (see Figure 9.3). When only $|S_{11}|$ is considered, the highest -10 dB impedance bandwidth is achieved for $W_2 = 8$ mm, which is 260 MHz. The lowest value of this is achieved when

$W_2 = 6$ mm, which is 200 MHz. For both values of $W_2 = 7$ mm and $W_2 = 8$ mm, $|S_{11}|$ is centered around 2.45 GHz, which is one of the design goals. But the impedance bandwidth is 15 MHz lower for the $W_2 = 7$ mm case than that of the latter case. When both $|S_{11}|$ and $|S_{22}|$ are considered, an impedance bandwidth of 235 MHz is achievable for $W_2 = 8$ mm. $|S_{21}|$ and $|S_{12}|$ values are lower than -21 dB over the entire simulated frequency range.

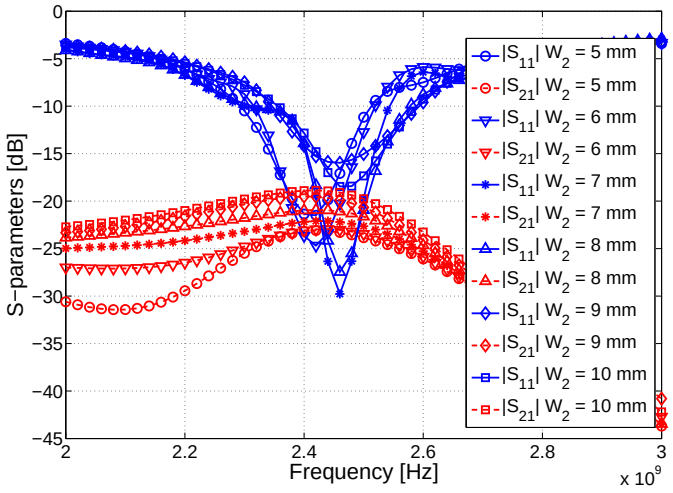

(a) Simulated $|S_{11}|$ and $|S_{21}|$.

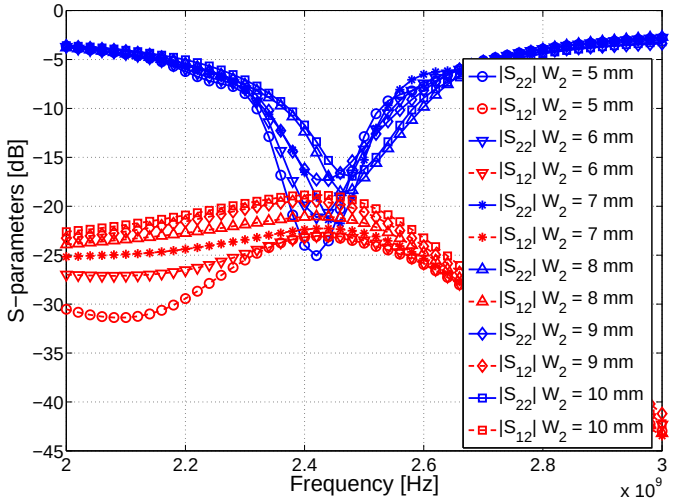

(b) Simulated $|S_{22}|$ and $|S_{12}|$.

Figure 9.4: Simulated S-parameters of HEMA for variable W_2 values. Ground plane length $L_1 = 70$ mm and width $W_1 = 4$ mm.

9.1.2 Substrate Material

The effective wavelength, λ_{eff} of an electromagnetic wave at a given frequency f_c, is inversely proportional to the square root of the product of permittivity and permeability of the medium, i.e., $\lambda_{eff} = \frac{1}{f_c\sqrt{\epsilon\mu}}$, where $\epsilon = \epsilon_r\epsilon_0$, and $\mu = \mu_r\mu_0$. The permittivity and the permeability in a vacuum are denoted by ϵ_0 and μ_0, respectively. The relative permittivity and permeability are denoted by ϵ_r and μ_r, respectively. Use of a ferrite substrate instead of a dielectric substrate for an antenna causes a lower λ_{eff}, thus resulting in a smaller dimension of the antenna structure. The reason for using ferrite material just below each meander structure is the higher loss of the used ferrite material. If ferrite material is used as substrate material instead of the FR4 substrate, then the design would suffer from lower radiation efficiency. In this case, simulations show that the antenna efficiency would be 27%. Therefore, for HEMA, ferrite material is only used beneath each meander structure. The Y-shaped slit on the ground plane is used to reduce the signal coupling between the ports, i.e, to reduce forward and reverse transmission coefficients ($|S_{21}|$, and $|S_{12}|$). Among other parameters, low dielectric losses in substrate material, low reflection coefficients, and low transmission coefficients enhance antenna efficiency.

9.1.3 Fabricated Antenna

According to the simulation results obtained in Section 9.1.1, an antenna was fabricated, as shown in Figure 9.5. The antenna model consists of two spatially separated half-cycle microstrip meander structures: a ferrite substrate below each meander structure and an FR4 substrate covered by the ground. A commercially available FR4 PCB is used as the system board. The dimensions of the meander structure are shown in Figure 9.5a.

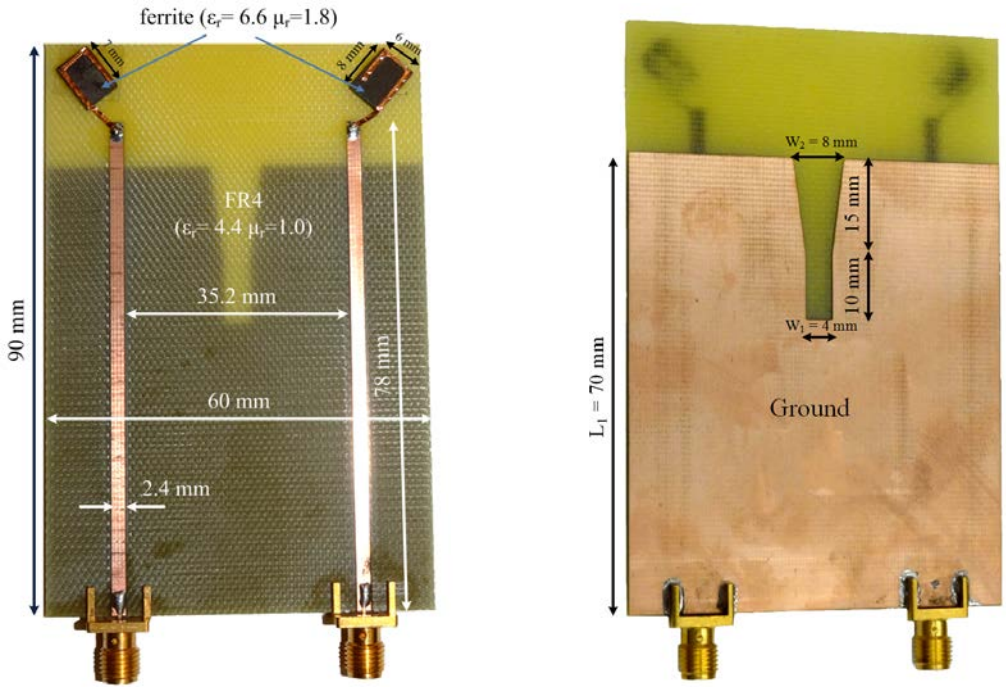

(a) Top view. (b) Bottom view.

Figure 9.5: Top and bottom views of fabricated HEMA.

A ferrite substrate of dimensions 8×6×1.5 mm^3 has a permittivity of 6.6 and a permeability of 1.8, with corresponding loss tangents of 0.014 and 0.112, respectively. Permittivity and loss tangent values of an FR4 substrate (90×60×1 mm^3) are 4.4 and 0.02, respectively. The size of the ground plane is 70×60 mm^2 and has a Y-shaped slit, where $W_1 = 4$ mm, and $W_2 = 8$ mm (see Figure 9.5b).

9.2 Measurement Results of Fabricated HEMA

The fabricated HEMA is shown previously in Figure 9.5. The simulated and measured S-parameters of that HEMA are compared in Figure 9.6. Simulated as well as measured forward- and reverse-voltage gains, S_{21} and S_{12}, are less than -21 dB in the simulated/measured frequency band, 2 GHz to 3 GHz.

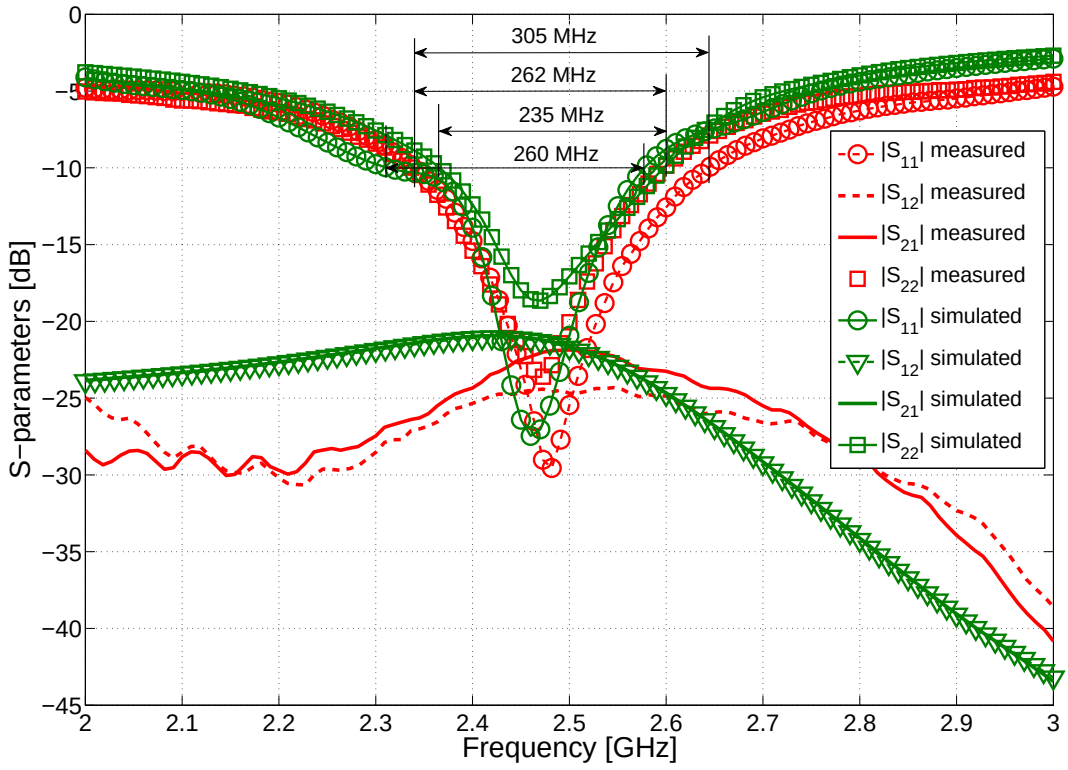

Figure 9.6: Simulated and measured S-parameters of HEMA.

These low values of $|S_{21}|$ and $|S_{12}|$ assure a very low signal coupling between the two antennas (ports), which is required. The impedance bandwidth of each port, which is measured at $|S_{ii}|$ = -10 dB, where $i \in \{1, 2\}$, is as follows: Port 1 has simulated and measured impedance bandwidths of 262 MHz and 305 MHz, respectively, whereas these values for port 2 are 262 MHz and 235 MHz, respectively. When the reflection coefficients of both antennas ($|S_{11}|$ and $|S_{22}|$) are considered together, the fabricated antenna has an impedance bandwidth of 262 MHz. The measured and simulated reflection coefficients of port 2 ($|S_{22}|$) are almost aligned but have a 5 dB difference at the center frequency, whereas this is only 2 dB for port 1 ($|S_{11}|$), but the curves are shifted approximately 20 MHz at their minimum values. In general, the simulated S-parameter values agree with that of the fabricated antenna.

Simulated three-dimensional radiation gain patterns of the HEMA are shown in Figure 9.7.

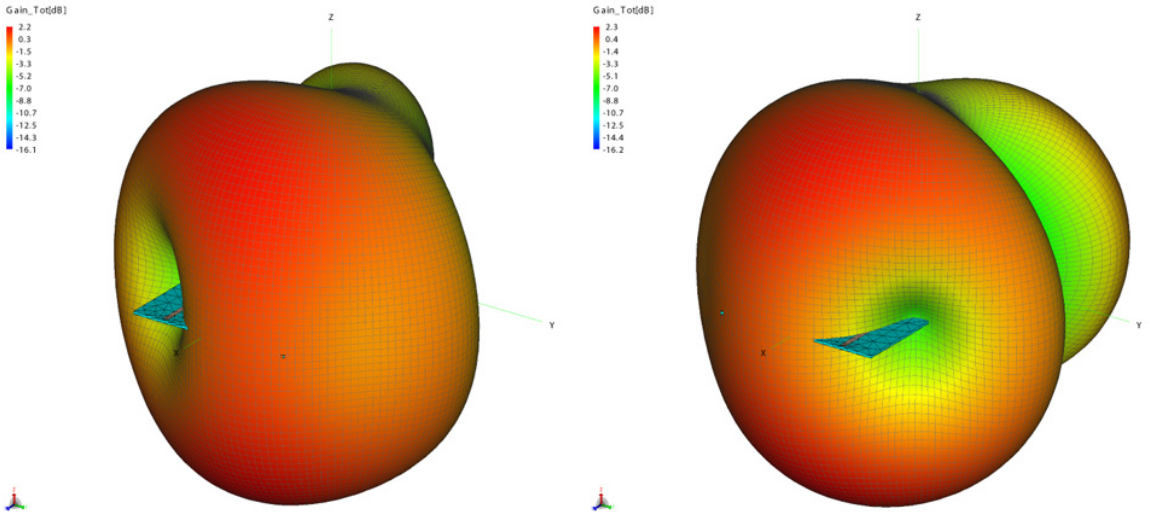

(a) Only Port 1 excited.

(b) Only Port 2 excited.

Figure 9.7: Simulated radiation patterns of HEMA.

Figure 9.7a and 9.7b show the gain patterns when each port was individually excited, i.e, only port 1 was excited for the case shown in Figure 9.7a, and only port 2 was excited for the case shown in Figure 9.7b. The maximum gain of each antenna is 2.2 dB and 2.3 dB, respectively. In the proceeding performance evaluations, the radiation patterns for elevation angle $\theta = 90°$ and azimuth angle $\phi =$ -180° $\cdots$ 180° were used, because a mobile handset is typically held in an upright position, and most of the electromagnetic field reaching a mobile device is assumed to be azimuthal. The 2D radiation patterns were measured in an anechoic chamber by using the HEMA and a horn antenna as the transmitter and the receiver, respectively.

Simulated and measured radiation patterns of the HEMA were normalized and shown in Figure 9.8.

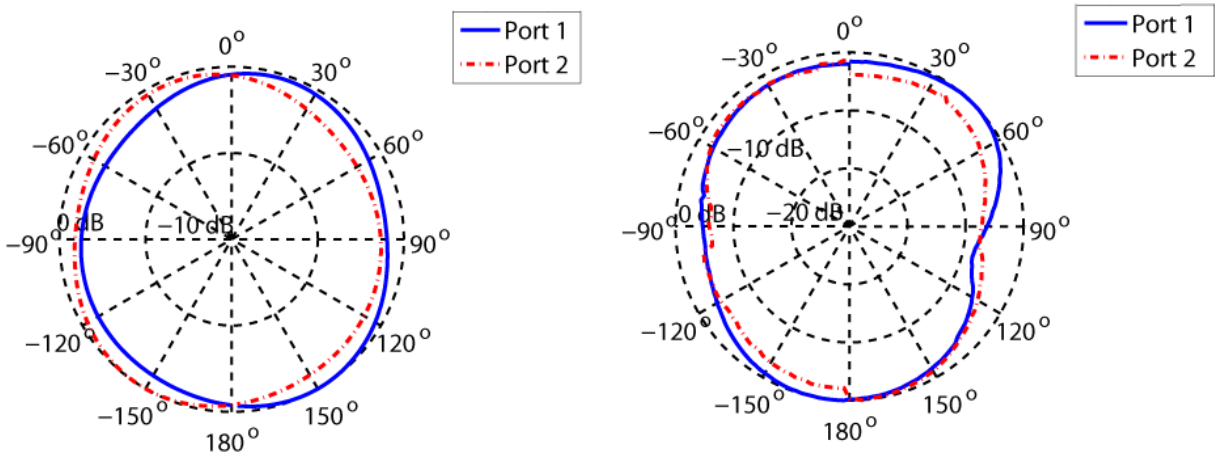

(a) Simulated.

(b) Measured.

Figure 9.8: Simulated and measured radiation patterns of HEMA. Both patterns are shown for $\phi = 90°$ and $\theta = -180° \cdots +180°$ (a) total gain and (b) normalized total measured power.

The 2D patterns were normalized in order to be easily compared. The gain values vary between the maximum and minimum of about 3 dB and 7 dB for simulated and measured patterns, respectively, when the azimuth angle varies from -180° to 180°. The greater variations in measured pattern could be caused by measurement errors and also from the dependency of gain for various ϕ angles, as shown in Figure 9.9. The difference between the highest and lowest gain values for $\phi = 86°$, $\phi = 88°$, $\phi = 90°$, $\phi = 92°$, and $\phi = 94°$ are 5.36 dB, 4.09 dB, 3.06 dB, 2.54 dB, and 3.09 dB, respectively. So slight variations in antenna orientation will affect the variations in gain.

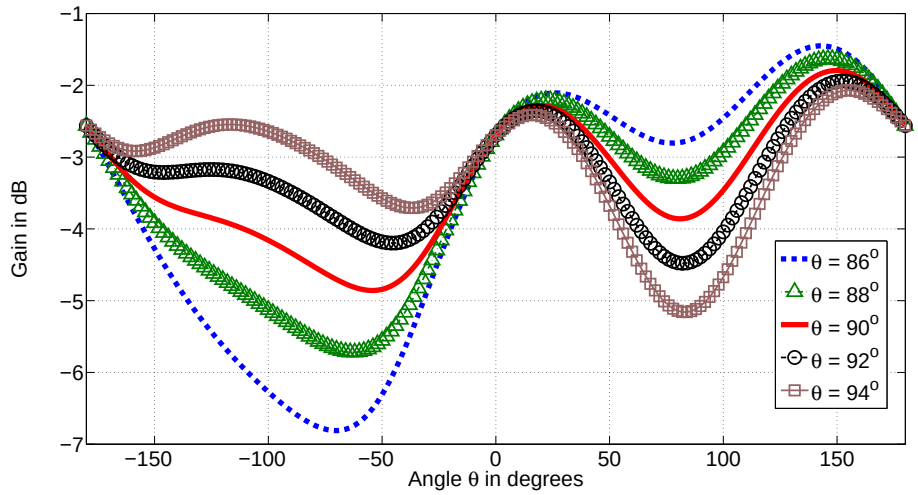

Figure 9.9: Simulated gain of HEMA vs. azimuth angle with elevation angle, θ, as a parameter.

9.3 Performance Analysis

A microwave parametric evaluation of the antennas was done in section 9.2. In this section, the antenna is evaluated by using communication system performance metrics such as BER and channel capacity. In order to evaluate these performance metrics, the channel matrix has to be realized according to (4.4.1), which includes the effects of mutual coupling between antennas, radiation efficiency of the antennas, and correlation between the transmitter-side and receiver-side radiation patterns. Simulated S-parameters at the center frequency, f_c, were used to calculate the mutual impedance matrices M_R and M_T, from equations (4.4.2) to (4.4.4). Since no impedance matching network was used, $\dot{\mathbf{Z}}_M$ was assumed to be the identity matrix. By using the simulated 2D radiation patterns (see Figure 9.8a), correlation coefficients were calculated according to equation (3.2.1) and are shown in Figure 9.10.

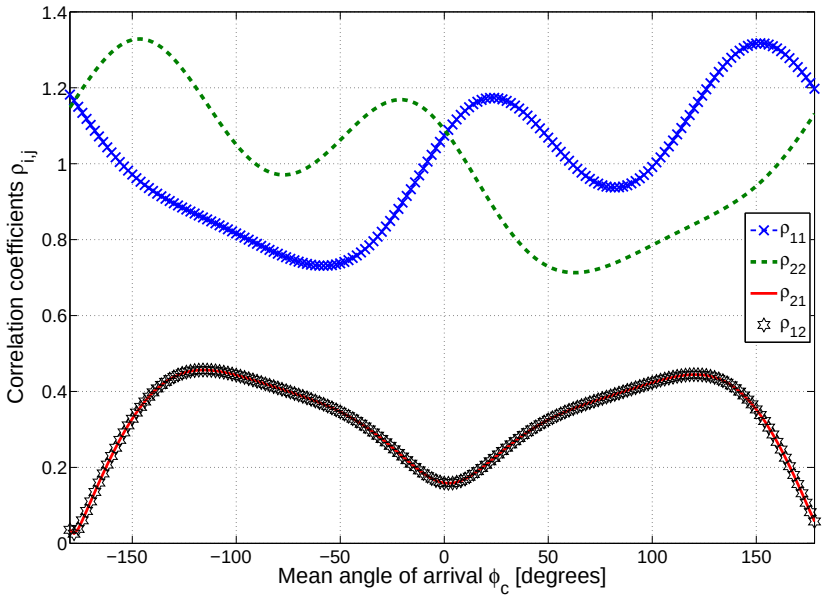

Figure 9.10: Simulated correlation coefficients of HEMA vs. mean angle of arrival ϕ_c.

The reason for using the simulated 2D radiation patterns for calculating correlation coefficients is that the electric field strengths are required according to equation (3.2.1), and those cannot be measured but can be obtained by simulations. These correlation values are used to generate $\mathbf{R}_T$ and $\mathbf{R}_R$ matrices in equation (4.4.1) for each angle. According to the conventional definition of correlation, the envelope is always lower than one. Since equation (3.2.1) is normalized with respect to the antenna gain of ideal isotropic radiation, it can be larger than one, as observed in Figure 9.10 [7].

The 2×2 MIMO transmission scheme introduced in [49] was used for evaluating BER performance. Bit error rate was simulated for each angle and then averaged, as shown in Figure 9.11 (green curve). To see the effect of antenna efficiency and correlation between radiation patterns on system performance, two more curves are presented.

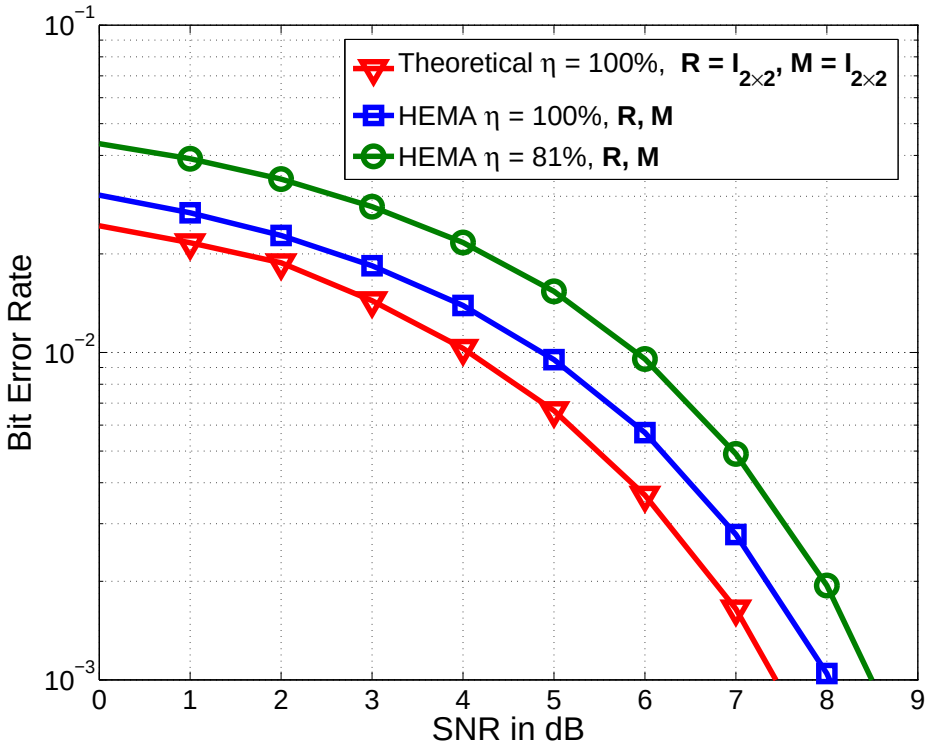

Figure 9.11: Average BER comparison of HEMA, and theoretical 2×2 MIMO vs. SNR using Alamouti scheme under Rayleigh fading channel.

The scheme presented by Alamouti [49] does not take antenna efficiency, mutual coupling, and correlation into account when generating the channel matrix, $\mathbf{H}$, i.e, it is assumed that $\mathbf{M}_T = \mathbf{M}_R = \mathbf{R}_T = \mathbf{R}_R = \mathbf{I}_2$ and $\eta_R = \eta_T = 100\%$ (see red curve) and hence is used as the reference. The radiation efficiency of the HEMA obtained by simulations is 81%. At the BER of 10^{-3}, the HEMA needs a 1.1 dB signal-to-noise ratio increment with respect to the reference curve to achieve the same performance. To see the effect of radiation efficiency on bit error rate, BER is simulated for the ideal antenna efficiency, $\eta = 100\%$ (blue curve). The correlation and mutual impedance matrices used are the same as for the green curve. When radiation efficiency is increased to 100%, a BER of 10^{-3} is achieved for 0.53 dB less SNR, compared to when the efficiency is 81% (compare blue and green curves). When compared

with the ideal curve (red curve), it can be seen that the non-ideal correlation and mutual impedance matrices cause degradation in system performance, even though the antenna has maximum efficiency. The performance degradation in this case is about 0.6 dB (compare blue and red curves).

Simulated ergodic capacity of the system is shown in Figure 9.12.

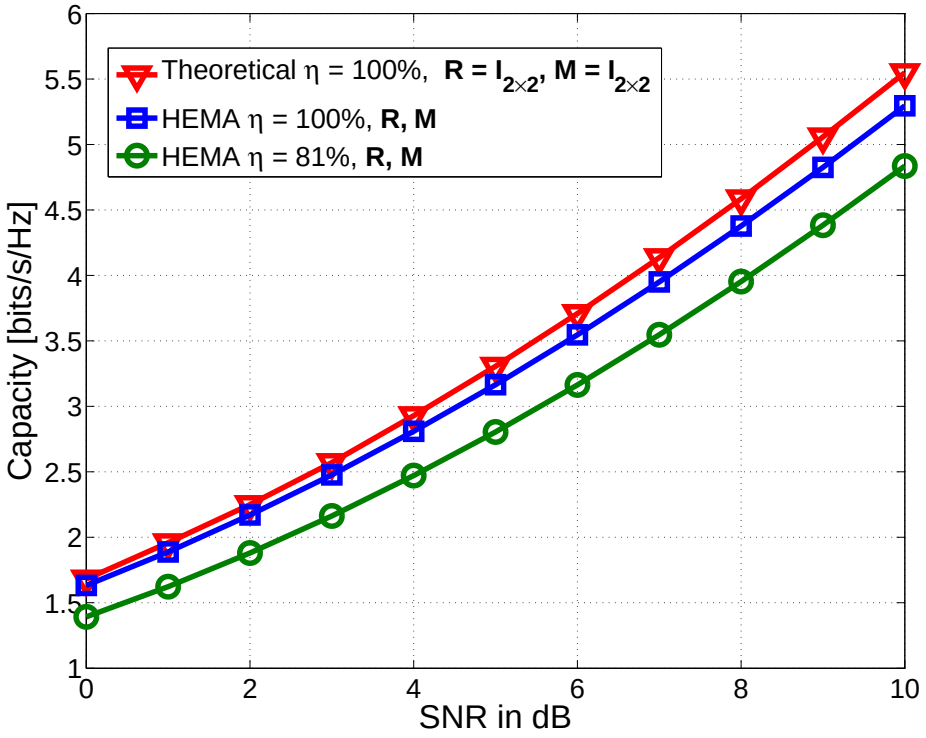

Figure 9.12: Average ergodic capacity comparison of HEMA, and theoretical 2×2 MIMO vs. SNR.

Capacity is calculated according to equation (3.3.3) for three different cases and is color-coded the same as for BER. For example, to achieve a capacity of 3 bits/s/Hz, the HEMA requires 1.4 dB higher SNR than for the ideal case (compare red and green curves). In evaluating ergodic capacity, by keeping the correlation matrix and the mutual impedance matrix of the

HEMA unchanged and only increasing the efficiency to 100%, the blue curve is generated. Now it needs only 0.4 dB higher SNR than for the ideal case to achieve the capacity of 3 bits/s/Hz. As shown, the antenna efficiency has a greater impact on the performance of the system than the correlation matrix and the mutual impedance matrix.

Table 2.1 compares bandwidth, antenna efficiency, PCB size, antenna element size, and envelope correlation coefficient of the proposed antenna with that presented in [34–38]. The envelope correlation coefficient of the proposed antenna calculated according to Eq. 11 in [44] is shown in Figure 9.13.

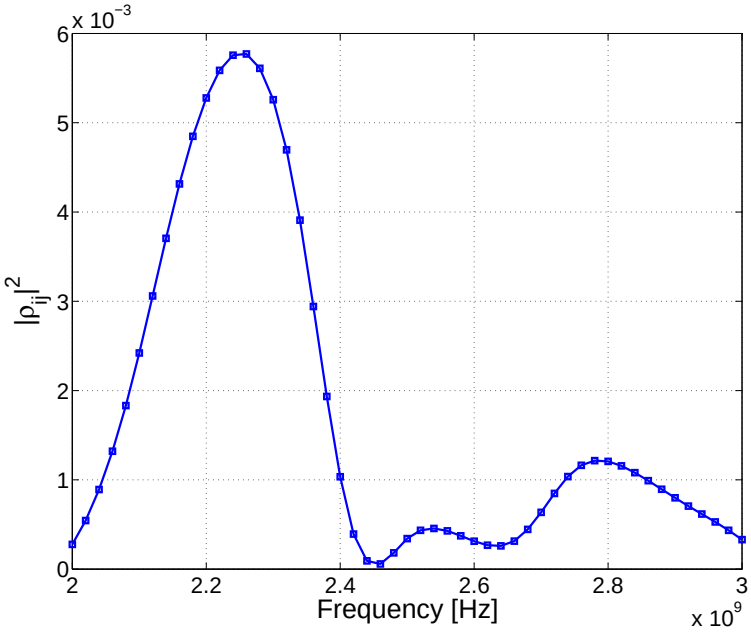

Figure 9.13: Envelope correlation of HEMA calculated according to Eq. 11 in [44].

It is only used for comparison purposes, since all other antennas listed in the table have presented the correlation coefficients calculated using the same formula.

The impedance bandwidth is given for a specific VSWR or reflection coefficient value

$|S_{ii}|$, where i is the port index. A VSWR of 3:1, 2.5:1, and 2:1 corresponds to a reflection coefficient of -6 dB, -7.4 dB, and -9.6 dB, respectively. For each of the preceding cases, the percentage of reflected power is 25.0%, 18.4%, and 11.0%, respectively. The lower the percentage, the more the power is transferred to the device. For the previously discussed VSWRs, the bandwidth of the proposed antenna is 519 MHz, 391 MHz, and 262 MHz, respectively. When compared with the listed antennas in Table 2.1, the proposed antenna has a lower bandwidth than only the one presented in [37]. But it has a lower efficiency and higher correlation coefficient, which are more critical factors when other performance matrices (BER and capacity) are considered. Lower correlation and higher efficiency improve the BER and capacity. Even though the area of PCB of the antenna presented in [37] is 17% smaller, its element size (area) is 3.9 times (296%) greater, and the correlation coefficient is more than eight times greater than that of the proposed antenna. The antenna presented in [36] has the highest efficiency of all listed. But its bandwidth is much less than the proposed antenna (200 MHZ compared to 519 MHz). Its PCB size is 11% larger, and the element size is 11.25 times larger than the proposed antenna. The antenna presented in [35] has the smallest PCB size (10×20 mm^2), which is 27 times smaller than the proposed antenna. But its correlation coefficients are more than 250 times greater, and the bandwidth is 111 MHz (28%) lower than the proposed antenna.

CHAPTER 10

CONCLUSIONS

A single circular patch antenna and a single ring patch antenna were miniaturized, fabricated using the available ferrite substrate materials in the lab, and tested for MIMO communications exploiting pattern diversity. At the initial stage, antenna parameters were determined empirically using the FEKO electromagnetic simulation tool. Using the far-field radiation pattern and S-parameters, the capacity and BER performance of the Fe 1-CPA and the Fe 1-ARA antennas were evaluated.

A volume reduction factor of 25.7 could be achieved, compared to the dielectric 2-CPA. Accordingly, the weight of the Fe 1-CPA could be reduced by a factor of 10.6. The achieved frequency bandwidth was 25 MHz, which is 3.2 times smaller than that of the dielectric 2-CPA. The capacity of the Fe 1-CPA was varied slightly with the azimuth angle, due to the unequal radiated power along the lobes of the far field radiation pattern.

On the other hand, the Fe 1-ARA shows a bandwidth of 70 MHz, which is close to that of the 2-CPA, and smaller variations in both capacity and BER as AoA changes. This is because the radiation far field patterns show more symmetrical shapes than those of Fe 1-CPA. The separation between port 1 and port 2 of the Fe 1-ARA is as small as $S_{12} = -3$ dB at the resonance frequency, and it is smaller than that of the Fe 1-CPA whose $S_{12} = -20$ dB at the resonance frequency. However, the BER of the Fe 1-ARA is slightly smaller than that of the Fe 1-CPA at a fixed SNR. Or, the Fe 1-ARA achieves the same BER (e.g., 10^{-3}) with slightly smaller SNR (e.g., 7.1 dB) than that of the Fe 1-CPA (e.g., 7.3 dB). This is because

the Fe 1-ARA has slightly higher radiation efficiency and higher determinant magnitude in the coupling matrix than the Fe 1-CPA.

The permeability, permittivity, and associated loss tangent values of the fabricated substrate materials are slightly different from those used for the FEKO simulations. Thus, the expected S-parameters and radiation patterns could not have been obtained. But the FEKO simulations using the measured permeability, permittivity, and loss tangent values agree with the measurements well, thus showing that if the substrate parameters were exactly the same as those used for the simulations, then measurement results of the fabricated antennas would agree with the simulation results. Overall, if the ideal mutual coupling matrices ($M_T = M_R = I$) and perfect antenna efficiencies ($\eta_T = \eta_R = 100\%$) are used, then the Fe 1-CPA and the Fe 1-ARA show the capacities and BERs similar to those of the dielectric 2-CPA, even if their volumes are reduced significantly, e.g., 25.7 times and 20 times, respectively. If the practical mutual coupling matrices M and imperfect antenna efficiencies η are used, then the proposed Fe 1-CPA and Fe 1-ARA show worse capacity and worse BER than the dielectic 2-CPA. This is because the antenna efficiency is low, such as 7% to 8% due to the high permeability tangent loss.

A high-efficiency half-cycle microstrip meander antenna with partial ferrite substrate was fabricated and tested. S-parameters and radiation patterns were measured in the lab and compared with those from simulations. An impedance bandwidth of 262 MHz was achieved by the fabricated HEMA. Simulations showed that the HEMA has a high antenna efficiency of 81%. Using the simulated far-field radiation patterns and S-parameters, ergodic capacity and BER performance of HEMA were evaluated. The effect of antenna efficiency, non-ideal correlation, and mutual impedance matrices on BER and ergodic capacity was evident. The

most critical parameter out of these three is antenna efficiency. When compared to the ideal case ($\mathbf{M}_T = \mathbf{M}_R = \mathbf{R}_T = \mathbf{R}_R = \mathbf{I}_2$ and $\eta_R = \eta_T = 100\%$), the HEMA shows only 1.0 dB degradation in SNR for a BER of 10^{-3}, and 1.4 dB degradation in SNR for 3 bits/s/Hz capacity. In other words, to achieve a BER of 10^{-3}, the HEMA requires a 1.0 dB higher SNR than that for the ideal case. And it requires a 1.4 dB higher SNR to achieve the same capacity of 3 bits/s/Hz than that for the ideal case. If the HEMA had an efficiency of 100%, then these values would be 0.6 dB and 0.3 dB, respectively. It is evident that the lower the antenna efficiency, the lower the performance.

PUBLICATIONS

Listed below are consequent publications of this dissertation and other publications of the author.

- C. K. Jayasooriya, H. M. Kwon, R. Syslo, Y.-K. Hong, J.-J. Lee, and G. Abo, "On performance of high-efficiency ferrite meander antenna (hema) for MIMO communications," *Progress In Electromagnetics Research B*, vol. 50, pp. 177-199, 2013.

- Seok Bae, Yang-Ki Hong, Jaejin Lee, Jihoon Park, Jeevan Jalli, Gavin S. Abo, Hyuck M. Kwon, and Chandana K. K. Jayasooriya, "Pulsed ferrite magnetic field generator for through-the-earth communication systems for disaster situation in mines," *Journal of Magnetics*, vol. 18, no. 1, pp. 43-49, 2013.

- Gavin S. Abo, Yang-Ki Hong, Ryan Syslo, Jaejin Lee, Woncheol Lee, Hyuck M. Kwon, and Chandana K.K. Jayasooriya, "Hexaferrite slant and slot MIMO antenna element for mobile devices," *Microwave and Optical Technology Letters*, vol. 55, no. 3, pp. 551 554, January 28, 2013.

- C. K. K. Jayasooriya, H. M. Kwon, R. Syslo, Yang-Ki Hong, Jaejin Lee, G. Abo, "High-efficiency ferrite meander antenna (HEMA) for LTE applications," *IEEE Military Communications Conference*, 2012 - MILCOM 2012, Oct. 29 2012 - Nov. 1 2012, pp.1-6.

- Chandana Jayasooriya, Hyuck M. Kwon, Seok Bae, and Yang-Ki Hong, "Miniaturized

annular ring patch antenna for MIMO communications," *IEEE Military Communications Conference*, San Jose, CA, Oct. 31-Nov. 3, 2010.

- Chandana Jayasooriya, Hyuck M. Kwon, Seok Bae, and Yang-Ki Hong, "Miniaturized single circular and single ring patch antenna for MIMO communications exploiting pattern diversity, *IEEE International Conference on Communications*, Cape Town, South Africa, May 24-28, 2010.

- Chandana Jayasooriya, Hyuck M. Kwon, Seok Bae, and Yang-Ki Hong, "Miniaturized circular patch antennas for MIMO communications - pattern diversity, *International Information Technique Group (ITG) - Workshop on Smart Antennas 2010*, University Bremen, Germany, February 23-24, 2010.

- Chandana Jayasooriya and Hyuck M. Kwon, Seok Bae, and Yang-Ki Hong, "Miniaturized multimode circular patch antennas for MIMO communications, *IEEE Vehicular Technology Conference 2009 Fall*, Anchorage, Alaska, September 20-23, 2009.

- Seok Bae, Yang-Ki Hong, Jae-Jin Lee, J.-H. Park, Jeevan Jalli, Gavin Abo, Hyuck M. Kwon, and Chandana K. K. Jayasooriya, "iniature and higher-order mode ferrite MIMO ring patch antenna for mobile communication system," *Progress In Electromagnetics Research B*, vol. 25, pp. 53-74, August 20, 2010.

- S. Bae, Y. K. Hong, J. J. Lee, J. Jalli, G. S. Abo, C. Jayasooriya, and Hyuck M. Kwon, MIMO 2-ring patch antenna (2-RPA) for W-LAN applications, Paper No. II-5 (Oral), presented at Korean Magnetics Society 2009 Summer Conference, An- myun-Do, South Korea, May 31 June 2, 2009.

Additionally, the following provisional application for a U.S. patent was filed.

- Hyuck M. Kwon, Chandana K. K. Jayasooriya, Yang-Ki Hong, Seok Bae, and Amitav Mukherjee, Miniaturized Circular Antenna, September 22, 2009. Doc number: 76788/v001.0.

REFERENCES

REFERENCES

[1] "1946: First mobile telephone call." [Online]. Available: http://www.corp.att.com/attlabs/reputation/timeline/46mobile.html

[2] D. H. Ring, "Mobile telephony - wide area coverage," 1947. [Online]. Available: http://www.privateline.com/archive/Ringcellreport1947.pdf

[3] M. Shiels, "A chat with the man behind mobiles." [Online]. Available: http://news.bbc.co.uk/2/hi/uk_news/2963619.stm

[4] M. Shi, *Technology Base of Mobile Cellular Operators in Germany and China*. Universitätsbibliothek, 2007. [Online]. Available: http://books.google.com/books?id=8ZRo-lxUDwkC

[5] G. S. Foschini and M. J. Gans, "On limits of wireless communications in a fading environment when using multiple antennas," *Wireless Personal Communications*, vol. 6, pp. 311–335, Mar. 1998.

[6] W. C. Jakes, *Microwave Mobile Communications*. New York: John Wiley & Sons., 1974.

[7] A. Forenza and R. W. Heath, Jr., "Optimization methodology for designing 2-CPAs exploiting pattern diversity in clustered MIMO channels," *IEEE Transactions on Communications*, vol. 56, pp. 1748–1759, Oct. 2008.

[8] C. Jayasooriya, H. Kwon, S. Bae, and Y.-K. Hong, "Miniaturized multimode circular patch antennas for MIMO communications," in *IEEE 70th Vehicular Technology Conference Fall (VTC 2009-Fall)*, Sept. 20-23, 2009, pp. 1–5.

[9] ——, "Miniaturized circular antennas for MIMO communication systems – pattern diversity," in *2010 International ITG Workshop on Smart Antennas (WSA)*, Feb. 23-24 2010, pp. 331–334.

[10] C. K. K. Jayasooriya, H. M. Kwon, S. Bae, and Y.-K. Hong, "Miniaturized single circular and single ring patch antenna for MIMO communications exploiting pattern diversity," in *IEEE International Conference on Communications (ICC)*, May 2010, pp. 1–5.

[11] C. Jayasooriya, H. Kwon, S. Bae, and Y.-K. Hong, "Miniaturized annular ring patch antenna for mimo communications," in *Military Communications Conference, 2010 - MILCOM 2010*, 2010, pp. 838–841.

[12] C. Jayasooriya, H. Kwon, R. Syslo, Y.-K. Hong, J. Lee, and G. Abo, "High-efficiency ferrite meander antenna (HEMA) for LTE applications," in *Military Communications Conference, 2012 - MILCOM 2012*, 2012, pp. 1–6.

[13] ——, "High-efficiency ferrite meander antenna (HEMA) for lte applications," in *Progress in Electromagnetics Research B*, vol. 50, 2013, pp. 177–199.

[14] C. A. Balanis, *Antenna Theory Analysis and Design*, 3rd ed. New Jersey: John Wiley & Sons, Inc., 2005.

[15] A. Forenza and R. W. Heath, Jr., "Benefit of pattern diversity via two-element array of circular patch antennas in indoor clustered MIMO channels," *IEEE Transactions on Communications*, vol. 54, pp. 943–954, May 2006.

[16] R. M. Manning, "An overview of antenna rd efforts in support of nasa's space exploration vision," in *Proceedings of IDGA's Military Antenna Systems Conference*, 2007, pp. 26–28. [Online]. Available: http://ntrs.nasa.gov/archive/nasa/casi.ntrs.nasa.gov/20070032056_2007033090.pdf

[17] J. A. Nessel, A. J. Zaman, and F. A. Miranda, "A miniaturized antenna for surface-to surface and surface-to-orbiter applications," *Microwave and Optical Technology Letters*, vol. 48, pp. 859–862, May 2006.

[18] P. Barr, A. Zaman, and F. Miranda, "A compact, broadband antenna for planetary surface-to-surface wireless communications," *Microwave and Optical Technology Letters*, vol. 48, pp. 521–524, Mar. 2006.

[19] G. Huff and J. Bernhard, "Integration of packaged rf mems switches with radiation pattern reconfigurable square spiral microstrip antennas," *Transactions on Antennas and Propagation, IEEE*, vol. 54, no. 2, pp. 464–469, 2006.

[20] N. Soldner, C. Lam, A. Singer, and J. Bernhard, "Beamforming in intelligent randomly distributed sensor networks using electrically-small dual-sector antennas for planetary exploration," in *Space Mission Challenges for Information Technology, 2006. SMC-IT 2006. Second IEEE International Conference on*, 2006, pp. 7 pp.–366.

[21] D. Werner and S. Ganguly, "An overview of fractal antenna engineering research," *Antennas and Propagation Magazine, IEEE*, vol. 45, no. 1, pp. 38–57, 2003.

[22] J. Zhu, A. Hoorfar, and N. Engheta, "Bandwidth, cross-polarization, and feed-point characteristics of matched hilbert antennas," *Antennas and Wireless Propagation Letters, IEEE*, vol. 2, no. 1, pp. 2–5, 2003.

[23] E. Telatar, "Capacity of multiantenna Gaussian channels," *European Transactions on Telecommunications*, vol. 10, pp. 585–596, Nov.-Dec. 1999.

[24] M. R. Andrews, P. P. Mitra, and R. deCarvalho, "Trippling the capacity of wireless communications using electromagnetic polarization," *Nature*, vol. 409, pp. 316–318, Jan. 2001.

[25] R. G. Vaughan and J. B. Anderson, "A multiport patch antenna for mobile communications," in *Proceedings of 14th European Microwave Conference*, Oct. 1984, pp. 607–612.

[26] R. G. Vaughan, "Two-port higher mode circular microstrip antennas," *IEEE Transactions on Antennas and Propagation*, vol. 36, pp. 309–321, Mar. 1988.

[27] R. Vaughan and J. B. Andersen, *Channels, Propagation and Antennas for Mobile Communications*. London: Institution of Electrical Engineers, 2003.

[28] F. Dammerle and W. Wiesbeck, "A biconical multibeam antenna for space-division multiple access," *IEEE Transactions on Antennas and Propagation*, vol. 46, pp. 782–787, June 1998.

[29] L. Dong, H. Ling, and R. W. Heath, Jr., "Multiple-input-multiple-output wireless communication systems using antenna patttern diversity," in *IEEE Global Telecommunications Conference GlobeComm 2002*, Nov. 2002, pp. 997–1001.

[30] D. Piazza, P. Mookiah, M. DAmico, and K. R. Dandekar, "Pattern reconfigurable circular patch antenna for MIMO communications," in *Proceedings of RiNEm Conference*, 2008.

[31] D. Piazza, M. D'Amico, and K. R. Dandekar, "MIMO communication system with reconfigurable circular patch antennas," in *Proceedings of IEEE Antennas and Propagation Society International Symposium*, Jul. 2008, pp. 1–4.

[32] E. Rajo-Iglesias, O. Quevedo-Teruel, M. L. Pablo-Gonzalez, and M. Sanchez-Fernandez, "A compact dual mode microstrip patch antenna for MIMO applications," in *Proceedings of IEEE Antennas and Propagation Society International Symposium*, Jul. 2006, pp. 3651–3654.

[33] M. Sanchez-Fernandez, E. Rajo-Iglesias, O. Quevedo-Teruel, and M. Pablo-Gonzalez, "Spectral efficiency in mimo systems using space and pattern diversities under compactness constraints," *IEEE Transactions on Vehicular Technology*, vol. 57, no. 3, pp. 1637–1645, 2008.

[34] C. Yang, Y. Yao, J. Yu, and X. Chen, "Novel compact multiband MIMO antenna for mobile terminal," *International Journal of Antennas and Propagation*, vol. 2012, p. 9, 2012.

[35] V. Ssorin, A. Artemenko, A. Sevastyanov, and R. Maslennikov, "Compact bandwidth-optimized two element MIMO antenna system for 2.5 - 2.7 GHz band," in *Proceedings of the 5th European Conference on Antennas and Propagation (EUCAP)*, April 2011, pp. 319–323.

[36] I. Dioum, A. Diallo, C. Luxey, and S. Farsi, "Dual-band monopole MIMO antennas for LTE mobile phones," in *ICECom, 2010 Conference Proceedings*, Sept. 2010, pp. 1–4.

[37] W.-Y. Li and W.-J. Chen, "Concurrent 2-port/3-port MIMO antenna system for UMTS/LTE2500 operation in the mobile phone," in *2011 IEEE International Symposium on Antennas and Propagation (APSURSI)*, July 2011, pp. 1918–1921.

[38] R. Kuonanoja, "Low correlation handset antenna configuration for LTE MIMO applications," in *IEEE Antennas and Propagation Society International Symposium (APSURSI)*, July 2010, pp. 1–4.

[39] J. Lee, Y.-K. Hong, S. Bae, G. Abo, W.-M. Seong, and G.-H. Kim, "Miniature long-term evolution (LTE) MIMO ferrite antenna," *IEEE Antennas and Wireless Propagation Letters*, vol. 10, pp. 603–606, 2011.

[40] R. Bhatti, S. Yi, and S.-O. Park, "Compact antenna array with port decoupling for lte-standardized mobile phones," *IEEE Antennas and Wireless Propagation Letters*, vol. 8, pp. 1430–1433, 2009.

[41] H. Sato, T. Hayashi, Y. Koyanagi, and H. Morishita, "Small array antenna for 2x2 MIMO terminal using folded loop antenna," in *First European Conference on Antennas and Propagation (EuCAP 2006)*, Nov. 2006, pp. 1–5.

[42] M. Sharawi, Y. Faouri, and S. Iqbal, "Design and fabrication of a dual electrically small MIMO antenna system for 4G terminals," in *2011 German Microwave Conference (GeMIC)*, March 2011, pp. 1–4.

[43] Q. Rao and D. Wang, "A compact dual-port diversity antenna for long-term evolution handheld devices," *IEEE Transactions on Vehicular Technology*, vol. 59, no. 3, pp. 1319–1329, 2010.

[44] S. Blanch, J. Romeu, and I. Corbella, "Exact representation of antenna system diversity performance from input parameter description," *Electronics Letters*, vol. 39, no. 9, pp. 705–707, May 2003.

[45] K. I. Pedersen, P. E. Mogensen, and B. H. Fleury, "Spatial channel characteristics in outdoor environments and their impact on bs antenna system performance," in *Proceedings of 48th IEEE VTC*, 1998, pp. 719–723.

[46] P. Soma, D. Baum, V. Erceg, R. Krishnamoorthy, and A. Paulraj, "Analysis and modeling of multiple-input multiple-output (MIMO) radio channel based on outdoor measurements conducted at 2.5 GHz for fixed BWA applications," in *IEEE International Conference on Communications (ICC 2002)*, vol. 1, 2002, pp. 272–276.

[47] J.-H. Lee and C.-C. Cheng, "Spatial correlation of multiple antenna arrays in wireless communication systems," *Progress In Electromagnetics Research*, vol. 132, pp. 347–368, 2012.

[48] L. M. Correira, *Wireless Flexible Personalized Communications*. New York: John Wiley & Sons, Inc., 2001.

[49] S. M. Alamouti, "A simple transmit diversity technique for wireless communications," *IEEE Journal on Selected Areas in Communications*, vol. 16, no. 8, Oct. 1998.

[50] T. M. Cover and J. A. Thomas, *Elements of Information Theory*, 2nd ed. Wiley-Interscience, 1991.

[51] D. M. Pozar, *Microwave Engineering*, 3rd ed. New Jersey: John Wiley & Sons, Inc., 2005.

[52] D. Frickey, "Conversions between s, z, y, h, abcd, and t parameters which are valid for complex source and load impedances," *IEEE Transactions on Microwave Theory and Techniques*, vol. 42, no. 2, pp. 205–211, 1994.

[53] R. Marks, D. Williams, and D. Frickey, "Comments on "conversions between s, z, y, h, abcd, and t parameters which are valid for complex source and load impedances" [with reply]," *IEEE Transactions on Microwave Theory and Techniques*, vol. 43, no. 4, pp. 914–915, 1995.

[54] O. N. Alrabadi, C. B. Papadias, A. Kalis, N. Marchetti, and R. Prasad, "Spatial multiplexing via antenna switching," *IEEE Communication Letters*, vol. 13, pp. 594–596, 2009.

[55] M. J. Alexander, "Capacitive matching of microstrip patch antennas," *IEE Proceedings Microwaves, Antennas and Propagation*, vol. 136, pp. 172–174, Apr. 1989.

[56] P. S. Hall, "Probe compensation in thick microstrip patched," *IEE Electronic Letters*, vol. 23, pp. 606–607, May 1987.

[57] R. W. Heath, Jr., private communication, 2009.

[58] C. A. Balanis, *Advanced Engineering Electromagnetics*. New York: John Wiley & Sons, Inc., 1989.

[59] M. A. Sultan, "Extended analysis of closed-ring microstrip antenna," *IEE Proceedings H, Microwaves, Antennas and Propagation,*, vol. 136, no. 1, pp. 67–69, Feb. 1989.

[60] J. Kennedy and R. Eberhart, "Particle swarm optimization," in *Proceedings of IEEE International Conference on Neural Networks, 1995*, vol. 4, 1995, pp. 1942–1948.